LBL-14585
c.2

Lawrence Berkeley Laboratory
UNIVERSITY OF CALIFORNIA

Physics, Computer Science & Mathematics Division

RECEIVED
LAWRENCE
BERKELEY LABORATORY

JAN 31 1983

LIBRARY AND
DOCUMENTS SECTION

TOTAL AND INCLUSIVE HADRON PRODUCTION BY e^+e^- ANNIHILATION AT $\sqrt{S}$ = 5.2, 6.5 AND 29.0 GeV

James Fraser Patrick
(Ph.D. Thesis)

July 1982

LBL-14585
c.2

Prepared for the U.S. Department of Energy under Contract DE-AC03-76SF00098

DISCLAIMER

This document was prepared as an account of work sponsored by the United States Government. While this document is believed to contain correct information, neither the United States Government nor any agency thereof, nor the Regents of the University of California, nor any of their employees, makes any warranty, express or implied, or assumes any legal responsibility for the accuracy, completeness, or usefulness of any information, apparatus, product, or process disclosed, or represents that its use would not infringe privately owned rights. Reference herein to any specific commercial product, process, or service by its trade name, trademark, manufacturer, or otherwise, does not necessarily constitute or imply its endorsement, recommendation, or favoring by the United States Government or any agency thereof, or the Regents of the University of California. The views and opinions of authors expressed herein do not necessarily state or reflect those of the United States Government or any agency thereof or the Regents of the University of California.

LBL-14585

TOTAL AND INCLUSIVE HADRON PRODUCTION BY e^+e^- ANNIHILATION AT $\sqrt{S}$ = 5.2, 6.5 and 29.0 GeV

By

James Fraser Patrick

(Ph.D. Thesis)

Lawrence Berkeley Laboratory
University of California
Berkeley, California 94720

July 1982

This work was supported by the Director, Office of Energy Research, Office of High Energy and Nuclear Physics Division of High Energy Physics of the U. S. Department of Energy under Contract No. DE-AC03-76SF00098.

ABSTRACT

Measurements are presented of R, the ratio of the total hadronic cross section to the cross section for mu pair production, and of the inclusive charged particle momentum distribution $s d\sigma/dx$ for e^+e^- annihilation at center of mass energies of 5.2, 6.5, and 29.0 GeV. The ratio R is found to be approximately 3.9, consistent with quark-parton model expectations, at each of the three energies with an estimated systematic uncertainty of 6%. The inclusive cross sections show significant deviation from the scaling behavior predicted by the quark-parton model.

ACKNOWLEDGMENTS

Of course any result from the Mark II experiment is due to the efforts of a large number of people. It has indeed been a privilege to work with so many talented physicists, engineers, and technicians. I am especially indebted to Jim Siegrist, on whose earlier work much of this analysis is based, for considerable encouragement and advice over the course of my graduate career. I am also extremely grateful to Martin Breidenbach for providing me with a superb education in the hardware aspects of modern experimental physics. Thanks also go to William Chinowsky for serving as my advisor for this work. And finally, I thank all the various people I have worked with over these years for making my graduate experience a pleasant one.

Contents

	Page
Acknowledgments	i
List of Figures and Tables	iii
Chapter 1 Introduction	1
Chapter 2 Apparatus	18
2.1 SPEAR	18
2.2 PEP	19
2.3 Mark II Detector	19
2.4 Data Reduction	29
Chapter 3 Event Selection	31
3.1 SPEAR Analysis	31
3.2 PEP Analysis	39
Chapter 4 Detection Efficiency	44
4.1 Production Models	44
4.2 Detector Model	53
4.3 The Unfold Method	53
4.4 Results of the Models	54
Chapter 5 Radiative Corrections	64
Chapter 6 Normalization	73
Chapter 7 Results and Conclusions	83
7.1 Total Cross Section Results	83
7.2 Results for $s\frac{d\sigma}{dx}$	89
References	102

Figures and Tables

		Page
Figure 1	One photon annihilation	2
Figure 2	Experimental results for R	3
Figure 3	$s\frac{d\sigma}{dx}$ as measured by the Mark I.	6
Figure 4	Higher order contributions to hadron production	9
Figure 5	R versus $\sin^2\theta_w$	12
Figure 6	QCD and weak contributions to R versus s	13
Figure 7	$s\frac{d\sigma}{dx}$ as measured by DASP, PLUTO, and the Mark I	15
Figure 8	Early $s\frac{d\sigma}{dx}$ measurements from TASSO compared to low energy measurements	16
Figure 9	The Mark II detector (transverse view).	21
Figure 10	The Mark II detector (isometric view).	22
Figure 11	The Mark II vacuum and shielding system	23
Figure 12	The small angle tagger (SAT)	26
Table 1	Composition of detector triggers.	28
Figure 13	Radial distribution of vertices at 5.2 and 6.5 GeV	33
Figure 14	Z distribution of vertices at 5.2 and 6.5 GeV	34
Table 2	Tau branching ratio estimates	36
Figure 15	Observed charged multiplicity at 5.2 and 6.5 GeV	38
Figure 16	Observed x distribution at 5.2 and 6.5 GeV	39
Figure 17	Total charged momentum at 29 GeV	40
Figure 18	Radial vertex distribution at 29. GeV	41
Figure 19	Z vertex distribution at 29. GeV	42
Figure 20	Observed charged multiplicity at 5.2 and 6.5 GeV	46
Figure 21	Observed x distribution at 5.2 and 6.5 GeV	47
Figure 22	Observed charged energy at 5.2 and 6.5 GeV.	48
Figure 23	Observed charged multiplicity at 29. GeV	51
Figure 24	Observed x distribution at 29. GeV.	52
Figure 25	Observed charged energy at 29. GeV	53
Table 3	Total detection efficiencies	55
Figure 26	Detection efficiency versus x at 5.2 and 6.5 GeV	57
Figure 27	Detection efficiency versus x at 29. GeV	58
Figure 28	Produced multiplicity for $x > 0.5$ events	59
Figure 29	Detected multiplicity at 5.2 GeV for $x > 0.5$ and 0.4 events	60
Figure 30	Detected multiplicity at 6.5 GeV for $x > 0.5$ and 0.4 events	61
Figure 31	Contribution to hadron production of order α^3	65
Figure 32	Angular distribution of radiated photons	68
Figure 33	Energy distribution of radiated photons	69

Figure 34 Detection efficiency versus radiated photon energy 70
Figure 35 $\sum$ ELA/$\sum$ P for QED events 75
Figure 36 Observed $\cos\theta$ distribution for Bhabhas 77
Figure 37 Observed momentum distribution for Bhabhas 78
Figure 38 Observed acollinearity distribution for Bhabhas 79
Table 4 Comparison of luminosity determinations 81
Table 5 Results for R 84
Table 6 Summary of systematic errors in the R measurement 85
Table 7 R values measured by other experiments 87
Figure 39 $s\frac{d\sigma}{dx}$ versus x as measured by this experiment 90
Table 8 $s\frac{d\sigma}{dx}$ as measured by this experiment 91
Table 9 Integrated x distributions compared to the mean multiplicity 93
Figure 40 $s\frac{d\sigma}{dx}$ versus s as measured by this experiment 94
Figure 41 $\frac{1}{\sigma}\frac{d\sigma}{dx}$ as measured by the Mark II and TASSO experiments 95
Figure 42 $\frac{1}{N}\frac{dN}{dx}$ versus x including and excluding gluon production 96
Figure 43 $\frac{1}{N}\frac{dN}{dx}$ versus x for events with a primary charm quark 97
Figure 44 $\frac{1}{N}\frac{dN}{dx}$ versus x including and excluding b quark production 98
Figure 45 $\frac{1}{N}\frac{dN}{dx}$ versus x for the Feynman Field model 100

Chapter 1

Introduction

Since the early observations of hadron production by e^+e^- annihilation, a clear picture of the mechanism has emerged. The study of this reaction has provided dramatic evidence for a quark–parton structure of matter. The process is believed to proceed via production of a pair of pointlike, spin $\frac{1}{2}$ quarks from the intermediate virtual photon (Figure 1), followed by their transformation ("fragmentation") into the observed hadrons, shown in Figure 1. Whereas the lifetime of the virtual photon is short ($\sim 1/Q$) compared to the time scale of the final state hadronization, in this picture the total cross section for hadron production, σ_{HAD}, should be that for production of pointlike fermion pairs, $e_q^2\sigma_{\mu\mu}$, summed over quark types, i.e.

$$R = \frac{\sigma_{HAD}}{\sigma_{\mu\mu}} = \sum_q e_q^2 \tag{1.1}$$

where

$$\sigma_{\mu\mu} = \frac{4\pi\alpha^2}{3s}\beta\left(\frac{3-\beta^2}{2}\right)$$

β = fermion velocity/speed of light

e_q = quark charge

s = square of center of mass energy.

The data [1], shown in Figure 2, in fact show that the ratio R is approximately constant for $\sqrt{s} \leq 3.6$ GeV with a value of about 2.5. This is interpreted as production of the up (u), down

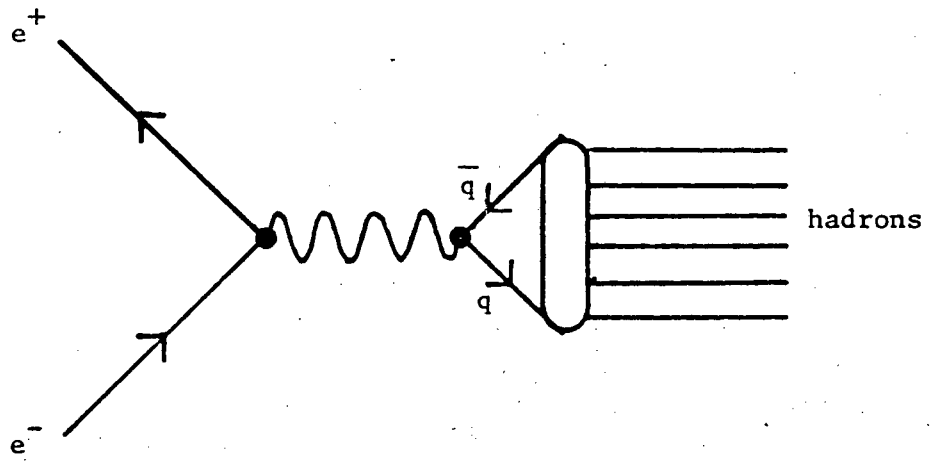

Fig. 1 Hadron production via one-photon annihilation

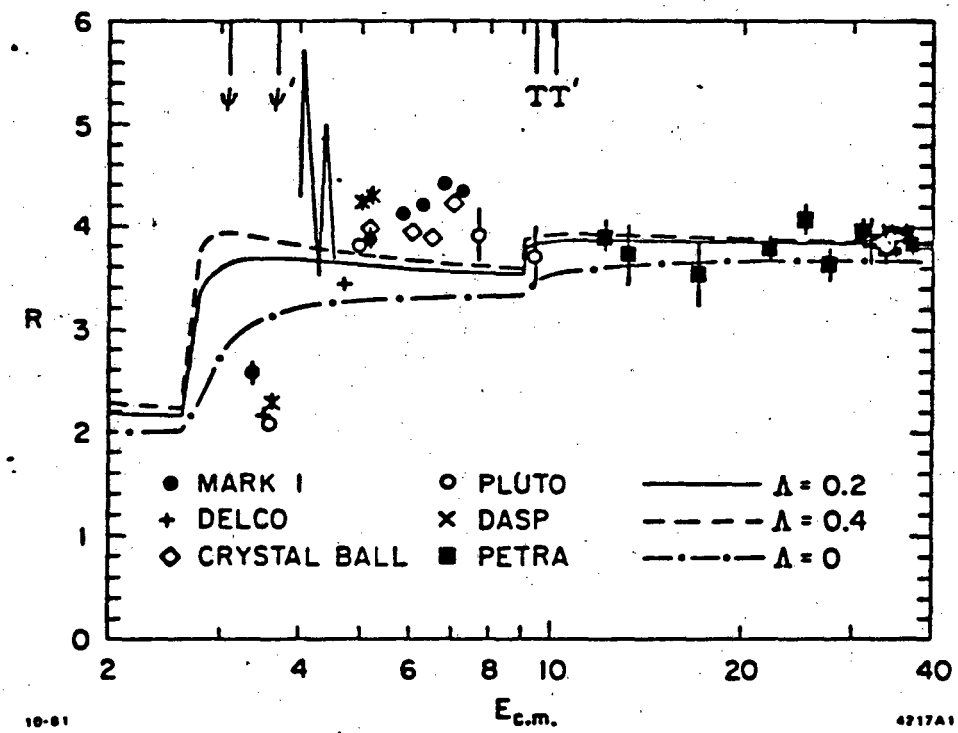

Fig. 2 Summary of R measurements in the range $\sqrt{s}$ = 3-36 GeV, together with QCD predictions.

(d), and strange (s) quarks with charges $\frac{2}{3}, -\frac{1}{3}$, and $-\frac{1}{3}$ respectively first proposed in 1964 to explain the basis for the hadron spectrum [2]. Following a region of complicated structure, R is again essentially constant with a value of about 4 from $\sqrt{s} = 4.5$ GeV all the way to 36 GeV, the highest energy at which measurements have been made. This step is interpreted as production of a charge $\frac{2}{3}$ charm (c) quark, originally proposed in 1971 to explain the absence of strangeness changing neutral currents [3]. To give agreement with the data, it is necessary to assume that the quarks each come in three types, or colors; this will be discussed further below. There are also prominent narrow resonances at 3.095, 3.69 (the ψ and ψ')[4], and 9.4, 10.0, and 10.3 GeV (the Υ's [5]). These families are interpreted as particle-anti-particle bound states of the c and $\bar{c}$ quarks, and of a charge $-\frac{1}{3}$ "bottom" (b) quark of mass $\approx$ 5.5 GeV and its antiquark respectively. The b quark only contributes $\frac{1}{3}$ unit to R in this model, of comparable magnitude to the systematic error in the experiments. Hence no clear cut step in R near 10 GeV can be attributed to the b.

Also in this model, it is natural to expect the final state hadrons to be clustered about the initial quark direction, giving the events a two "jet" topology. Experiments have shown that the observed hadrons have limited transverse momentum ($\approx$ 300 MeV/c) about some axis (the "jet" axis), and furthermore the angular distribution of this axis is consistent with that expected for pointlike fermions [6].

From general considerations, the single particle inclusive cross section can be written [7].

$$E\frac{d^3\sigma}{dp^3} = \frac{\alpha^2}{2s^2}[(w_1 + w_0) + (w_1 - w_0)\cos^2\theta] \tag{1.2}$$

where the functions w_1 and w_0 are a *priori* unknown functions of s and the particle energy E. It has been argued that at high energies, where mass effects are unimportant, these functions should depend only on the dimensionless parameter $x = 2\ \mathrm{E}/\sqrt{s}$ [8], where E is the particle

energy. In this case, the above expression becomes

$$\frac{\alpha^2}{8s}\beta x[(w_1(x)+w_0(x))+(w_1(x)-w_0(x))\cos^2\theta]. \tag{1.3}$$

Integrated over angle, this may be expressed in terms of so called quark fragmentation functions as

$$\frac{d\sigma}{dx}=\frac{4\pi\alpha^2}{s}\sum_q e_q^2\, 2\, D_q^h(x) \tag{1.4}$$

where $D_q^h(x)$ is a distribution function for producing a hadron h with energy fraction x from the quark q. Measurements made over the range 3 GeV $< \sqrt{s} <$ 8 GeV showed that scaling was approximately valid in that energy region (Figure 3) [9].

So the naive parton model has been very successful in explaining the qualitative features of e^+e^- annihilation, within the errors of the experiments. Next are considered possible extensions of this basic model, as well as a more formal theoretical structure, and how these would affect the measurements discussed above. This is in hopes that better experiments over a wider energy range may be sensitive to new phenomena.

Changes in R may be indications of new particle production as above. It is expected that a charge $\frac{2}{3}$ quark, known as the top (t), should exist to restore lepton-hadron symmetry and cancel the so called triangle anomalies [10]. This quark would contribute $1\frac{1}{3}$ unit to R. There should also exist a series of narrow resonances analogous to the ψ and Υ families below the threshold for unbound $t\bar{t}$ production. Extensions of the standard SU(2) $\times$ U(1) theory of weak and electromagnetic interactions predict the existence of charged scalar bosons from which are derived masses of the fermions and gauge bosons, the so called "Higgs" particles [11]. These particles would be produced by e^+e^- annihilation. Provided there is sufficient center of mass energy available, their contribution to R would be

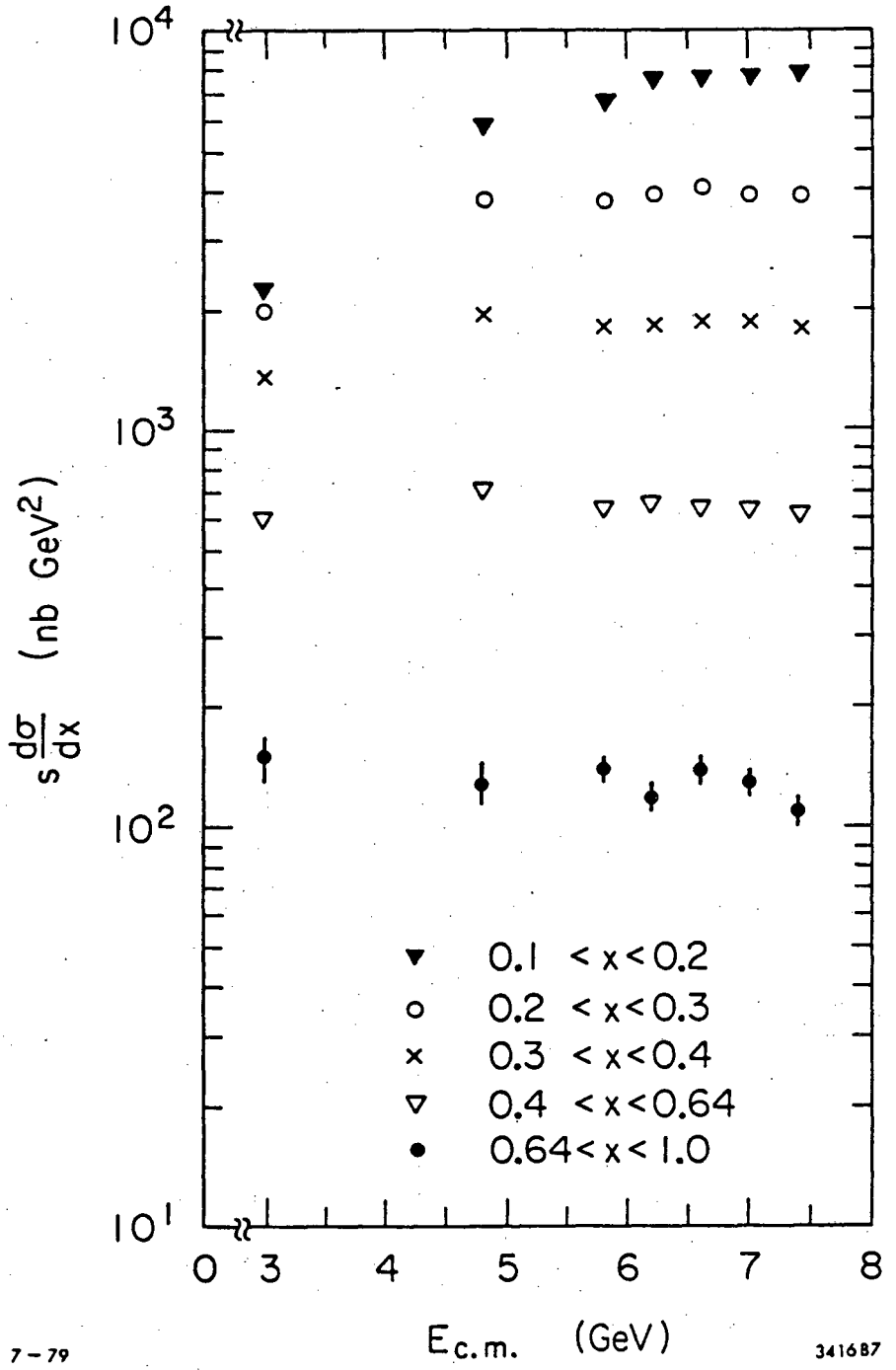

Fig. 3 $s\,d\sigma/dx$ as measured by the Mark I experiment.

$$R_H = \frac{1}{4}\beta^3. \tag{1.5}$$

The change in R from production of these particles would be more difficult to observe due to its small size (Δ R $\leq \frac{1}{4}$) and the gradual β^3 threshold behavior. It should be noted that observation of new particle production by changes in R depends to some extent on the decay modes of the particles. If the decay modes cause the events to have significantly different properties than the usual hadronic events, they may not be readily observed in this measurement. For example, with the selection criteria used for hadronic events in this experiment, the detection efficiency for $\tau^+\tau^-$ events is only 10% at $\sqrt{s} = 29$ GeV. This is due to the low multiplicity of τ decay products and the fact that all decays contain at least two undetected neutrinos.

We have already seen that is necessary to assume that quarks come in three types, or "colors" to obtain approximate agreement of the parton model with the data. It is also necessary to make this assumption in the calculation of the π^0 decay rate [12]. Furthermore, if baryons are composed of three quarks, Fermi statistics requires that they not be completely identical, or the Δ^{++} could not exist. Quantum Chromodynamics (QCD) is a theory of strong interactions which describes interactions between colored quarks through exchange of massless vector gluons. This is a "non-abelian" theory, the gluons also carry color and thus can interact with other gluons. The coupling constant of the theory depends on the momentum transfer squared of the process Q^2 as

$$\alpha_s(Q^2) = \frac{12\pi}{(33 - 2n_f)\ln\frac{Q^2}{\Lambda^2}} \tag{1.6}$$

n_f is the number of fermions in the theory, and Λ is a scale parameter to be determined from experiment, of comparable fundamental significance to the electric charge. It is noted that if n_f is not too large, α_s decreases toward zero with increasing Q^2, the theory is thus said to be asymtotically free [13]. So for large enough energy scales, the strong coupling constant is small enough so that perturbative calculations may be reliable. In particular, for $Q^2 = 5^2$ GeV^2, $\Lambda =$

0.3 GeV, and $n_f = 4$, α_s is approximately 0.2. Although not negligible, next order corrections should be only of order a few percent, and at higher Q^2 α_s is smaller still.

Whereas the primary quarks produced in e^+e^- annihilation may radiate gluons, the theory makes several important predictions for this process. Most dramatically, events where an energetic gluon is emitted at large angles to a quark should have a distinctive 3–jet topology. Such events were first observed by experiments at the PETRA storage ring [14]. Diagrams containing gluon emission should also affect the total cross section. And gluon emission by the primary quarks should lead to a depletion in particle production at large x, and thus a violation of scaling since the coupling constant depends on Q^2.

In QCD, the total hadronic cross section is modified by the diagrams shown in Figure 4. First order contributions include diagrams with single gluon emission (a) as well as inteference between second order virtual corrections (b) and the lowest order process. Second order contributions include diagrams with two gluons (c) in the final state as well as interference between third order virtual corrections (d) and the single gluon diagrams. The total cross section through order α_s^2 is

$$R = 3\sum_q e_q^2\Big(1 + C_1(\frac{\alpha_s}{\pi}) + C_2(\frac{\alpha_s}{\pi})^2\Big) \tag{1.7}$$

A straightforward computation of the third order contribution gives $C_1 = 1$ [15]. The coefficient C_2 depends on how the coupling constant is renormalized. This calculation has been done using several schemes, giving the following results [16]:

$$\begin{aligned} C_2 &= 7.36 - 0.44n_f && \text{minimal subtraction (MS) scheme} \\ C_2 &= 1.99 - 0.12n_f && \text{modified minimal subtraction } (\overline{\text{MS}}) \text{ scheme} \\ C_2 &= -2.19 + 0.16n_f && \text{momentum space subtraction (mom) scheme.} \end{aligned} \tag{1.8}$$

This does not mean that the physical value of R is dependent on the renormalization scheme.

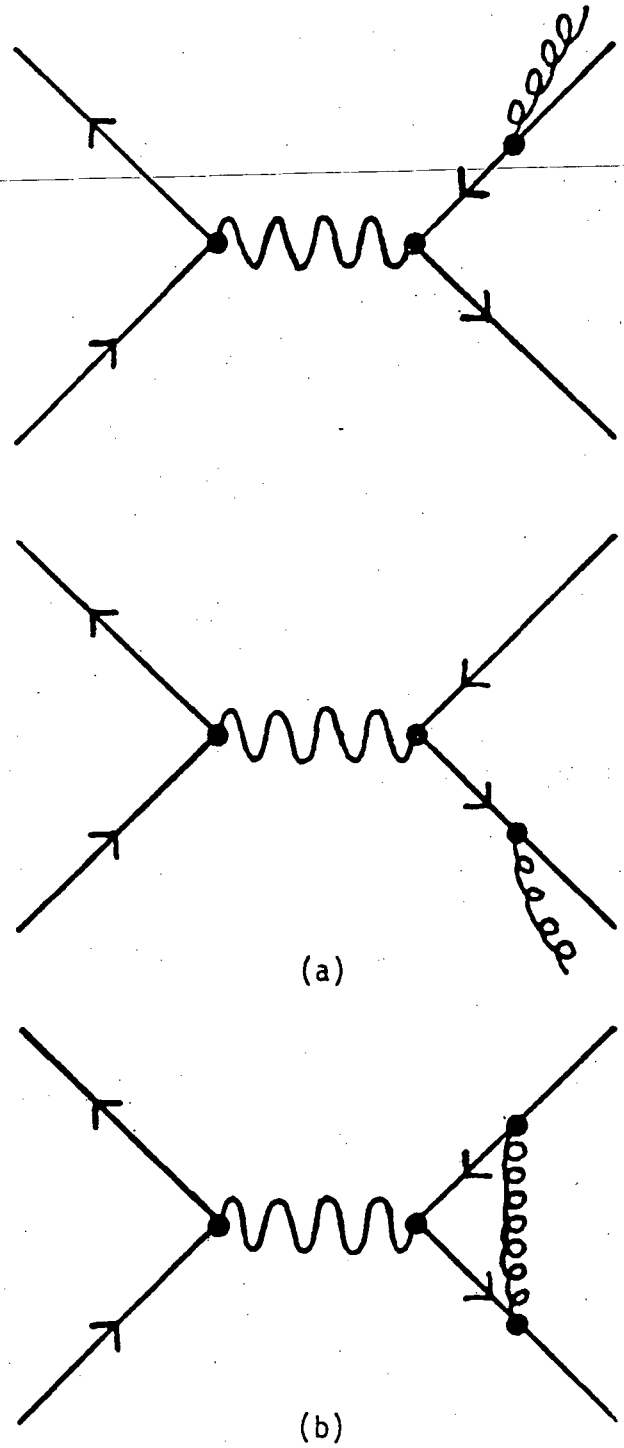

Fig. 4 Diagrams contributing to hadron production of order α_s.

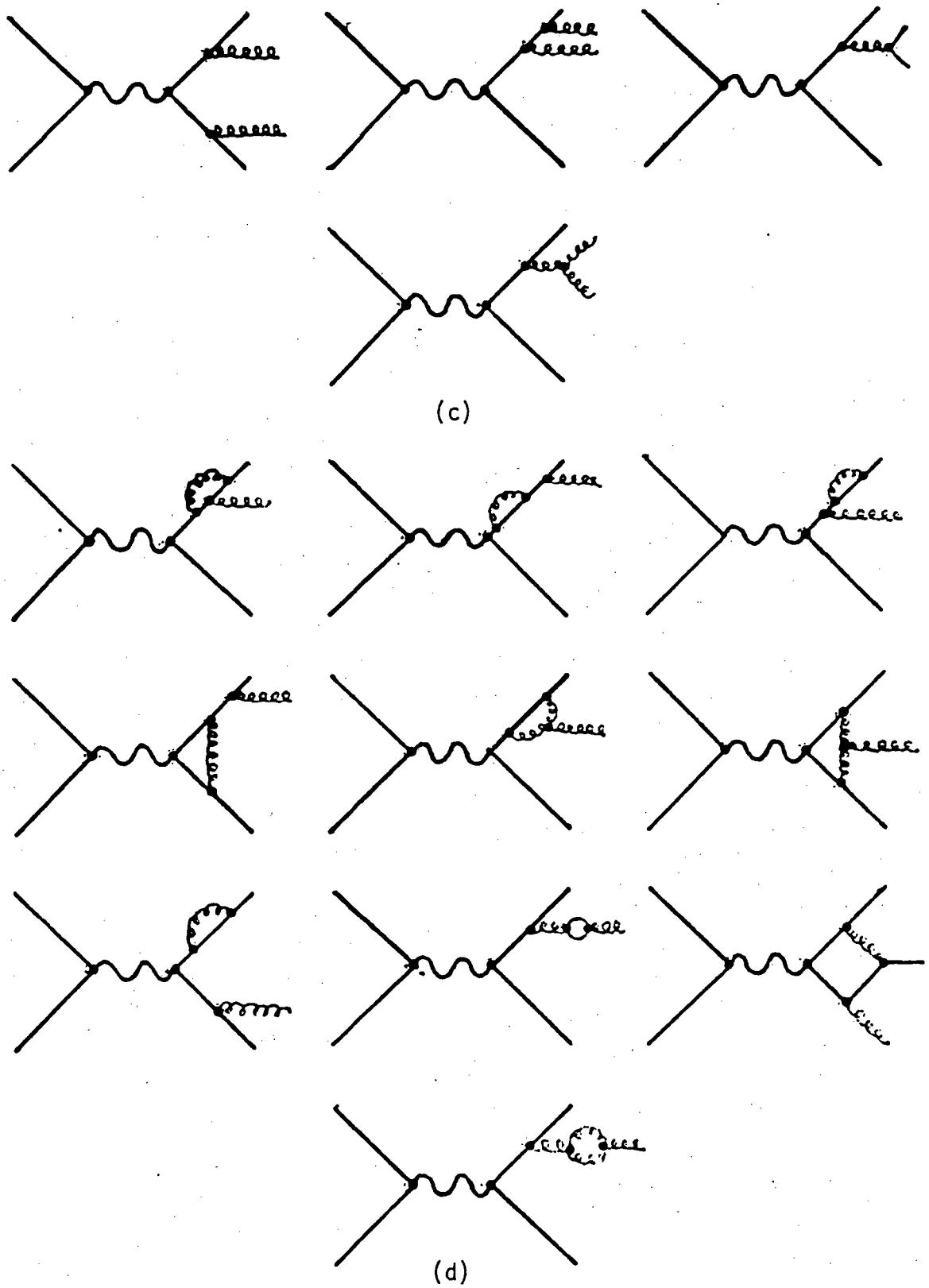

Fig. 4 Diagrams contributing to hadron production of order α_s^2.

Rather it is a consequence of the finite number of terms of the perturbation expansion considered, and the freedom of choice of the expansion parameter. What the different methods do is absorb different diagrams into the definition of the coupling constant, actually making it somewhat larger in the case of the $\overline{\mathrm{MS}}$ and mom schemes. However, they at the same time make the coefficient C_2 smaller, and are believed to make higher order coefficients smaller as well, so that the second order calculation should be a better estimate of the true result [17]. This is important since computation of the next order QCD corrections is extremely difficult. At $\sqrt{s} = 6.5$ GeV, the first order QCD corrections increase the expected value of R by 7%, and the second order corrections by an additional 2% (for $\Lambda = 0.3$ GeV). These corrections are 5% and 0.7% at $\sqrt{s}$ $= 30$ GeV.

The value of R is considered to be the most reliable quantitative prediction of QCD, as it does not require detailed understanding of the quark fragmentation process. Furthermore, α_s^2 corrections have been computed and are small. Also, an absolute prediction is made for any given energy. In contrast, predictions about jet structure depend sensitively on details of quark fragmentation, especially complicating computation of α_s^2 corrections [18]. For deep inelastic scattering, QCD only predicts the evolution of the structure functions with Q^2, not the structure functions themselves. Also, there are complications from charm production and non-perturbative effects which must be considered. Unfortunately, the deviation from the simple quark-parton prediction for R is only about 5–7%, meaning that a good understanding of systematic errors is required for a meaningful test of QCD. Also, the variation of R with energy due to the running coupling constant, a critical aspect of the theory, is even smaller and thus even more difficult to test by this method.

The annihilation process may proceed through an intermediate Z° as well as through a virtual photon. Thus the total cross section will be altered by diagrams containing Z° exchange,

and by interference between Z° and photon exchange diagrams, so the total cross section should reflect the the Z°–quark couplings. This process supplements neutrino scattering measurements, since s, c, and b quark production is substantial, and since the initial particles are electrons, which have different couplings to the Z° than neutrinos. The full expression for R in the standard SU(2) × U(1) theory is given by [19]

$$R = \frac{1}{\sigma_{\mu\mu}} \sum_q \left(\left(1 + C_1^V \frac{\alpha_s}{\pi} + C_2^V \left(\frac{\alpha_s}{\pi}\right)^2\right) \sigma_{VV} + \left(1 + C_1^A \frac{\alpha_s}{\pi} + C_2^A \left(\frac{\alpha_s}{\pi}\right)^2\right) \sigma_{AA} \right) \tag{1.9}$$

where

$$C_1^V = \frac{4\pi}{3}\left(\frac{\pi}{2\beta} - \frac{3+\beta}{4}\left(\frac{\pi}{2} - \frac{3}{4\pi}\right)\right)$$

$$\sigma_{VV} = e_q^2 \sigma_{\mu\mu} - \frac{G_F \alpha e_q}{\sqrt{2}} g_V^e g_V^q \left(\frac{M_Z^2 (M_Z^2 - s)}{(M_Z^2 - s)^2 + \Gamma_Z^2 M_Z^2} \right)$$

$$+ \left(\frac{G_F^2}{32\pi} \right) g_V^{q^2} (g_V^{e^2} + g_A^{e^2}) \frac{s M_Z^4}{(M_Z^2 - s)^2 + \Gamma_Z^2 M_Z^2}$$

$$\sigma_{AA} = \left(\frac{G_F^2}{32\pi} \right) g_A^{q^2} (g_V^{e^2} + g_A^{e^2}) \frac{s M_Z^4}{(M_Z^2 - s)^2 + \Gamma_Z^2 M_Z^2}$$

$$M_Z = 37.3 / \sin\theta_W \cos\theta_W$$

$$g_V^i = 2I_3^i - 4e_i \sin^2\theta_W$$

$$g_A^i = 2I_3^i$$

and Γ_Z is the width of the Z°, I_3^i is the weak isospin of the particle ($+\frac{1}{2}$ for u and c quarks, $-\frac{1}{2}$ for d, s and b quarks and electrons), and θ_W is the Weinberg angle. The effect of the weak corrections on R is shown in Figures 5 and 6. For $\sin^2\theta_W = 0.22$, approximately the value measured in deep inelastic lepton–hadron scattering [20], the contribution from Z° exchange is less than 1% at 30 GeV but rises rapidly above that point, eventually far exceeding the magnitude of the QCD corrections. Thus for center of mass energies above 40 GeV, tests of QCD using R

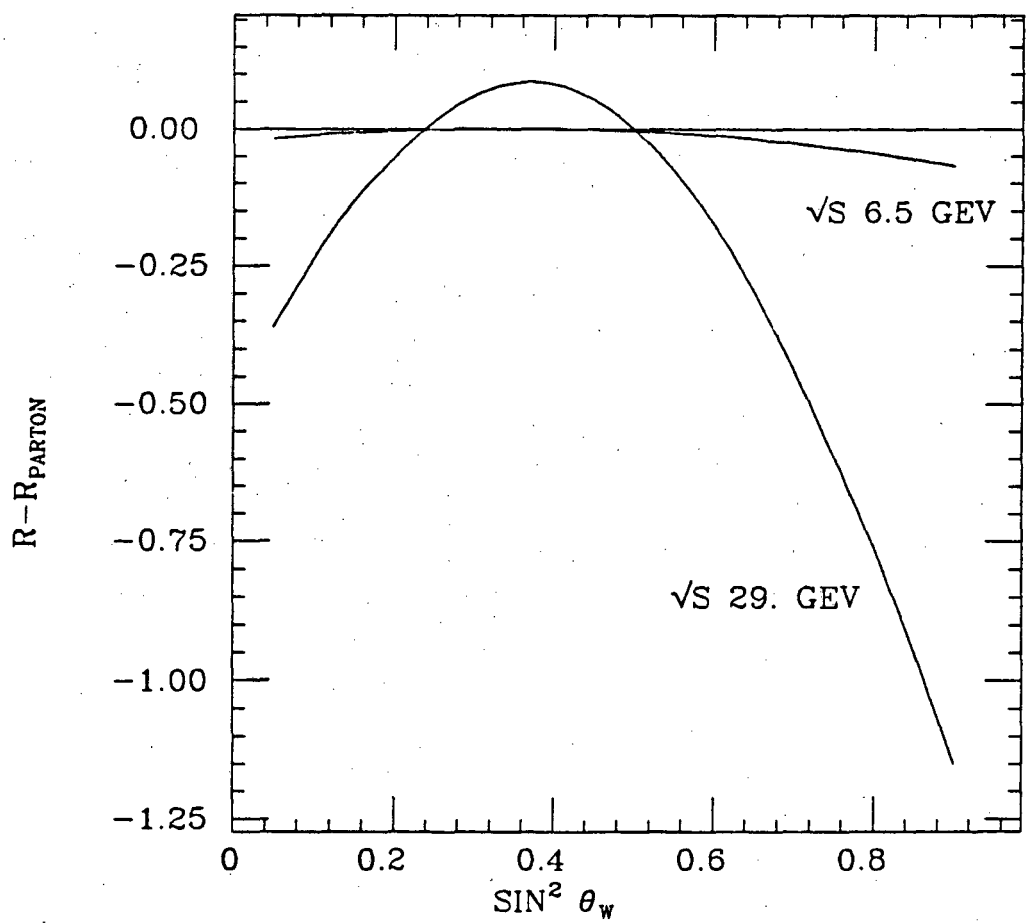

Fig. 5 The difference between R as computed including weak effects and the naive parton model estimate as a function of $\sin^2\theta_W$.

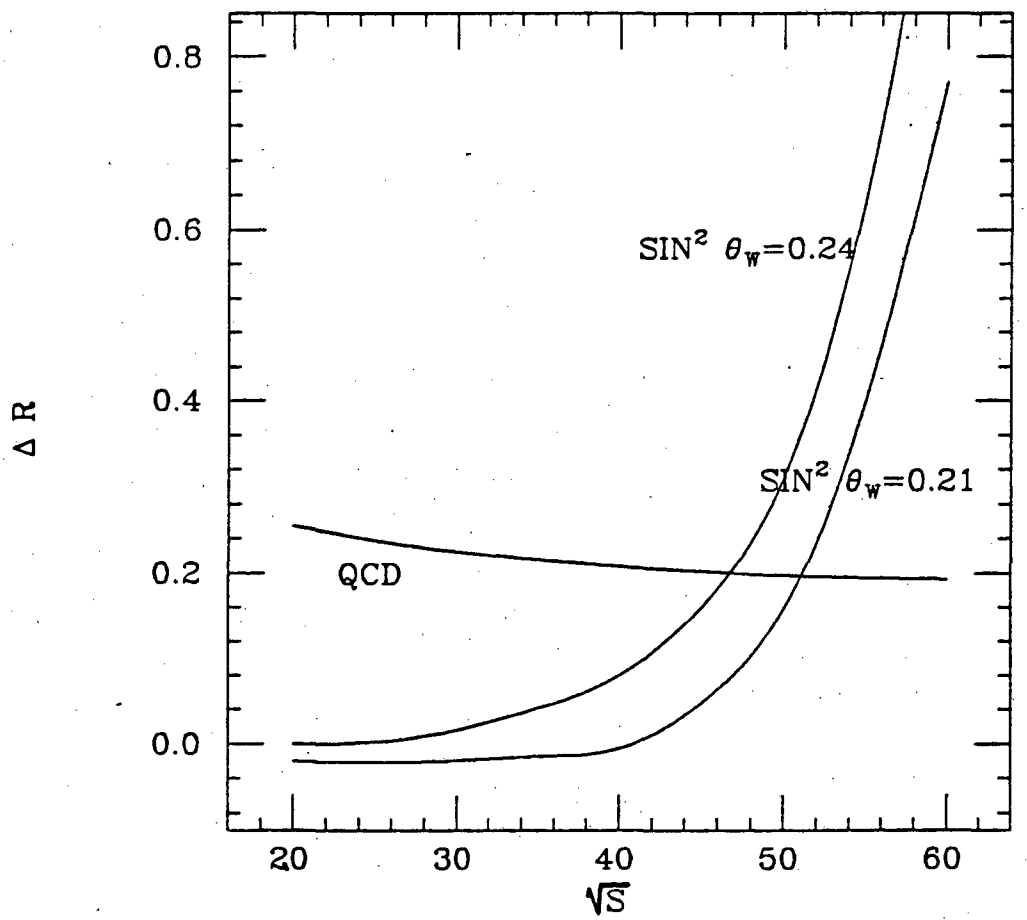

Fig. 6 Contributions to R from QCD effects, and from weak effects with $\sin^2\theta_W$=.21 and .24.

become difficult due to uncertainties in the weak coupling parameters. Precise determination of the weak coupling parameters below 30 GeV would require exceptional precision over a wide energy range, measurements of R are only sensitive to large deviations from the standard model with the accepted value of $\sin^2\theta_W$.

The effect of gluon emission on the x distributions is most conveniently computed in the Altarelli–Parisi formulation [21]. Here the probability of gluon emission is convoluted with the pure quark fragmentation function to obtain an integro–differential equation for the fragmentation function. Since hadrons may come from gluons as well as from quarks, a gluon fragmentation $D_g^h(x)$ function must also be included, giving a pair of coupled equations:

$$Q^2\frac{dD_q^h(x,Q^2)}{dQ^2} = \frac{\alpha_s(Q^2)}{2\pi}\int_0^1 dy\int_0^1 dz\delta(x-yz)(P_{q\to q}(y)D_q^h(z,Q^2)+P_{g\to q}(y)D_g^h(z,Q^2))$$

$$Q^2\frac{dD_g^h(x,Q^2)}{dQ^2} = \frac{\alpha_s(Q^2)}{2\pi}\int_0^1 dy\int_0^1 dz\delta(x-yz)(P_{g\to q}(y)\sum_q D_q^h(z,Q^2)+P_{g\to g}(y)D_g^h(z,Q^2)). \tag{1.10}$$

These equations state that the probability for obtaining a hadron with energy fraction x is equal to the probability for obtaining a parton with energy fraction z times the probability of obtaining a hadron from this parton with energy fraction y such that $x = yz$, summed over y and z, and summed over partons. The solution of these equations is qualitatively that the fragmentation functions should decrease logarithmically with increasing s. This calculation is very similar to the calculation of the evolution of structure functions in deep inelastic lepton–hadron scattering. Since there is no prediction made for the fragmentation functions at a particular s, to test the theory it is necessary to take measurements at some s and evolve them to a different s using the above equations. The result of doing this is that the functions should be lower by 20% at $x = 0.7$ at $\sqrt{s}$ of 29 GeV than at 5 GeV [22]. This prediction is complicated by the fact that only final decay products of resonances and heavy quarks are observed in experiments. There is thus dependence on resonance production and decays of c and b quarks, which are not completely

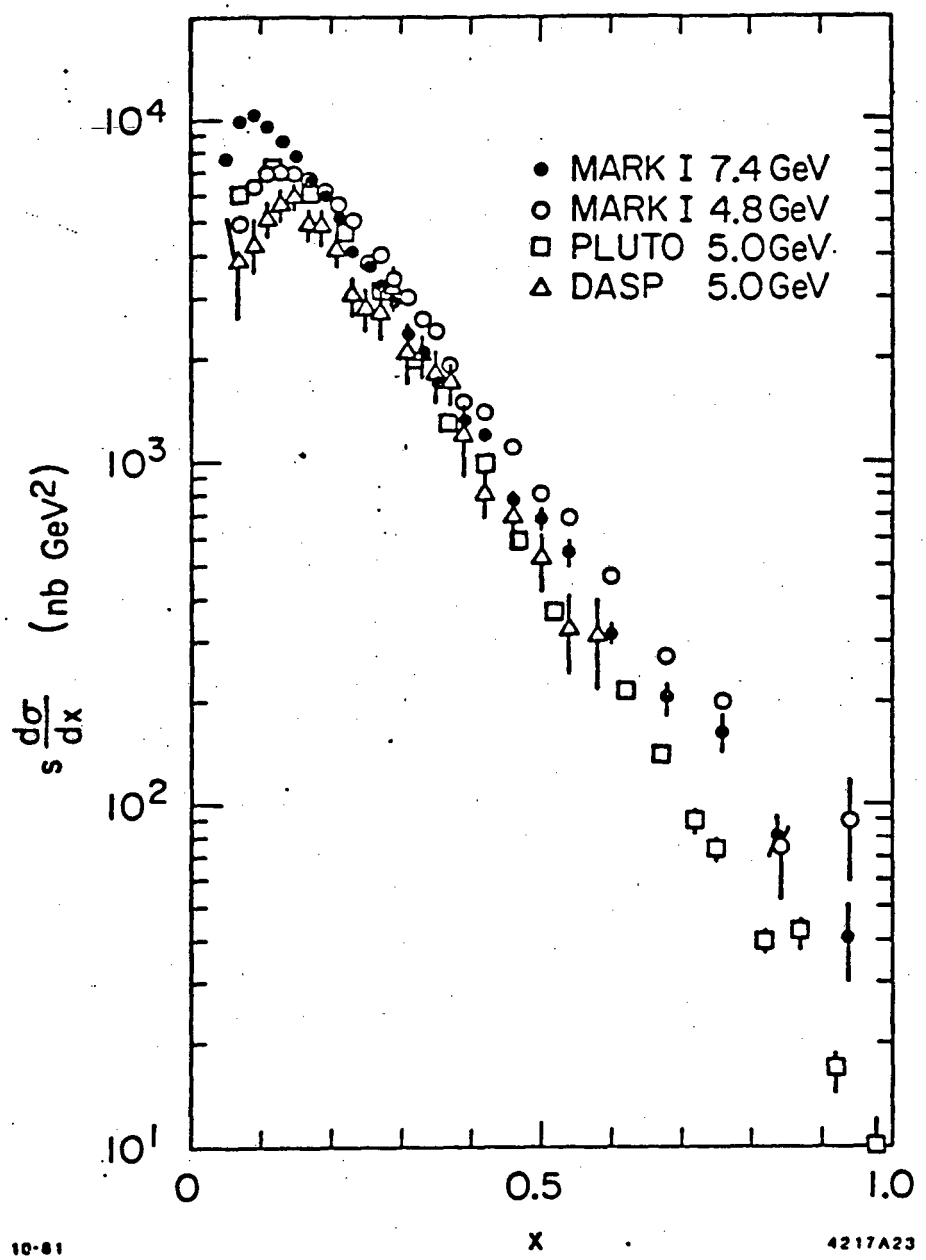

Fig. 7 $sd\sigma/dx$ as measured by the Mark I, PLUTO, and DASP detectors.

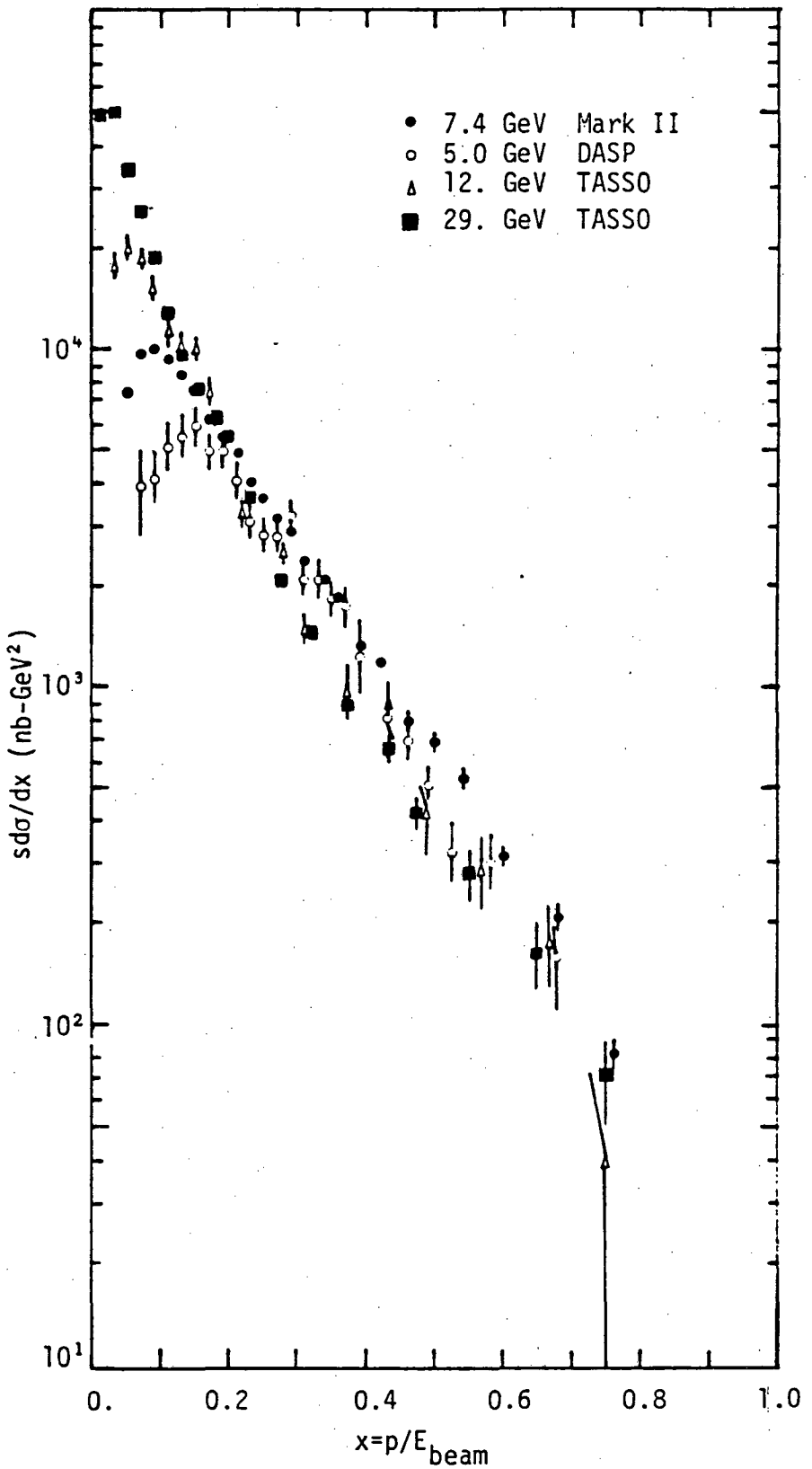

Fig. 8 Early measurements of sdσ/dx from the TASSO experiment compared with measurements at lower energies.

understood. Another difficulty in observing scaling violation is the disagreement among different experiments at low energies (Figure 7) [23]. Early experments at higer energies [24], due to large systematic errors as well as uncertainties in the low energy data, were not sensitive to deviations from scaling behavior (Figure 8). Thus use of the same detector over a wide range of energy should help lessen systematic errors increasing the sensitivity to scaling violation.

The goal of this thesis is to measure the total and inclusive cross sections for hadron production by e^+e^- annihilation with as high a precision as possible over a wide energy range, specifically at $\sqrt{s} = 5.2$, 6.5, and 29.0 GeV. A search is made for deviations of R from the naive parton model, and for violations of scaling behavior in the inclusive distributions.

Chapter 2

Apparatus

The data for these measurements were acquired with the SLAC-LBL Mark II detector at the SPEAR (5.2 and 6.5 GeV) and PEP (29.0 GeV) storage rings located at the Stanford Linear Accelerator Center.

§2.1 SPEAR

In the SPEAR storage ring, beams consisting of a single bunch of electrons or positrons which counter-rotate in the same vacuum pipe and magnet lattice, colliding every 780 ns at two points. The peak luminosity of the machine depends on the beam energy as

$$\mathcal{L} \approx 10^{31}(\frac{E_b}{3.25})^4 \mathrm{cm}^{-2}\mathrm{sec}^{-1} \tag{2.1}$$

for center of mass energies up to 6.5 GeV. The machine is operated in "top up" mode at center of mass energies up to 5.2 GeV. In this mode, beams are injected from the SLAC linear accelerator directly into the configuration used for colliding beams. Thus it is not necessary to discard the beams prior to injection, and no "ramping" of the machine configuration is necessary, reducing the filling time. With this luminosity, and taking into account machine and detector reliablility

and the several hour beam lifetime, typically 1500-3000 hadronic events per day were recorded at these energies. Thus the simplicity of the e^+e^- process is gained at the expense of event rate due to the colliding beam method and the small electromagnetic cross sections.

§2.2 PEP

The PEP storage ring was proposed in 1974 to extend the study of e^+e^- annihilation to center of mass energies up to 30 GeV. Construction began in the spring of 1977 and was completed 2 years later. Beams were first stored and collided in May, 1979, and following machine and experimental checkout serious data taking began in December, 1979. The beams consist of three bunches each counter-rotating in the same magnet lattice in the 2200 meter circumference ring. Collisions occur every 2.4 μs in each of six interaction areas. The maximum energy per beam is 18 GeV with the 5.5 MW of installed rf power. To date, all experimental running has been at $\sqrt{s} = 29$ GeV, the maximum energy at which the machine can run in "top up" mode. The maximum initial luminosity obtained during data taking on which this analysis is based was $7.0 \cdot 10^{30}$ cm^{-2} sec^{-1}, with typical operating currents of 20 ma per beam. Integrated luminosities of typically 200-300 nb^{-1}, corresponding to 80-120 hadronic events, were accumulated per day during this time.

§2.3 Mark II Detector

The SLAC-LBL Mark II detector was assembled on the beam line at SPEAR in the fall of 1977, where data taking began in April 1978. This detector had significant improvements in solid angle coverage, momentum resolution, and in the trigger compared to the previous SLAC-LBL Mark I detector which helped reduce systematic errors in measurements of the total and

inclusive cross sections. The data discussed here were acquired in the spring of 1979, during the last seven weeks of running at SPEAR, corresponding to integrated luminosities of 4.16 events/pb at 5.2 GeV and 1.63 events/pb at 6.5 GeV. In the summer of 1979, the detector was moved to PEP interaction area 12, where some modifications were made to better cope with the PEP environment. Since the detector had been operated for some time in the high event rate environment at SPEAR, it was well understood by the time it was moved, allowing a rapid analysis of the data at PEP. The data for these measurements were acquired during the spring running cycle in 1981, corresponding to an integrated luminosity of 13.6 events/pb.

The detector as configured at SPEAR has been described in considerable detail elsewhere [25]. Hence the following discussion will be limited to the aspects most important for the present analysis, and the modifications made for PEP.

The PEP configuration of the Mark II detector is shown in Figures 9 and 10. It basically consists of a series of concentric cylindrical detectors designed to determine the momenta and identities of the produced particles with good efficiency over as large a solid angle as practical. Tracks leaving the interaction point encounter in succession the following elements:

Vacuum pipe. (Figure 11). The 0.15 mm thick corrugated stainless steel pipe used at SPEAR was replaced by a 2 mm thick aluminum pipe. Also, masks composed of tantalum, tungsten, and lead were installed at 3 and 9 meters from the interaction point. The goal of these modifications was to reduce backgrounds from synchrotron radiation and from electrons which had radiated or had been scattered in the residual gas, causing them to be misfocussed by the quadropoles into the detector. The pipe was flared at each end to minimize the amount of material encountered by tracks from Bhabha events heading toward the luminosity monitor. Further details regarding the vacuum and shielding system may be found in reference [26].

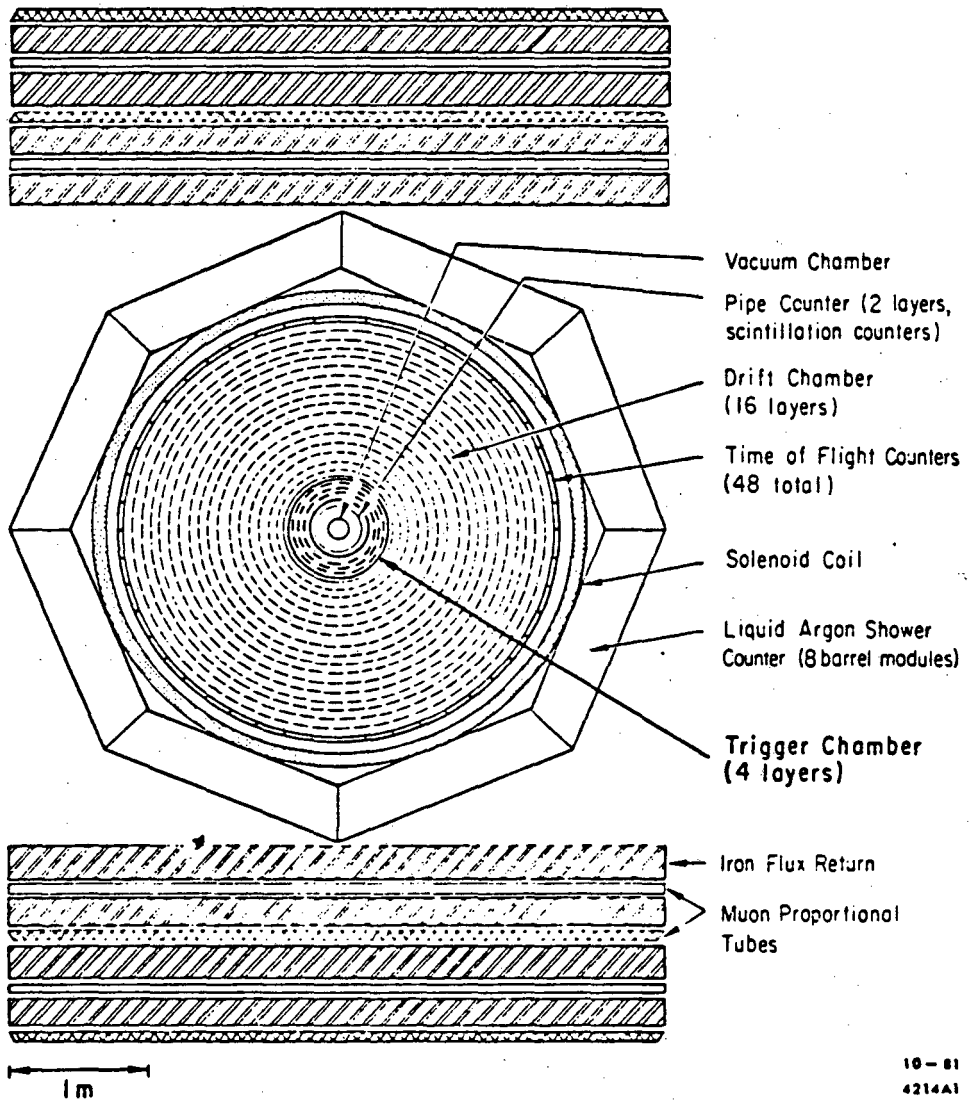

Fig. 9 The Mark II detector (transverse view).

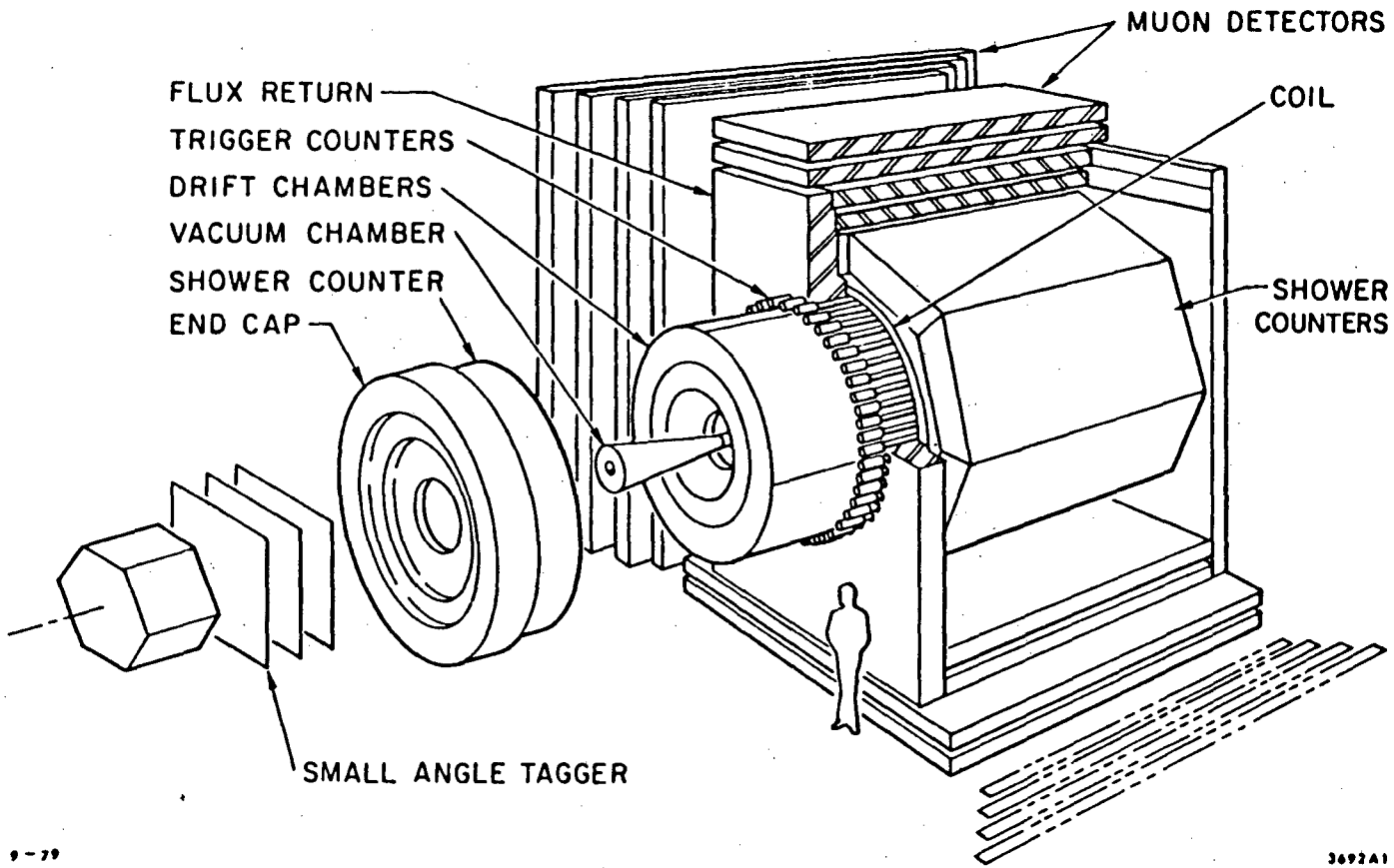

Fig. 10 The Mark II detector (isometric view).

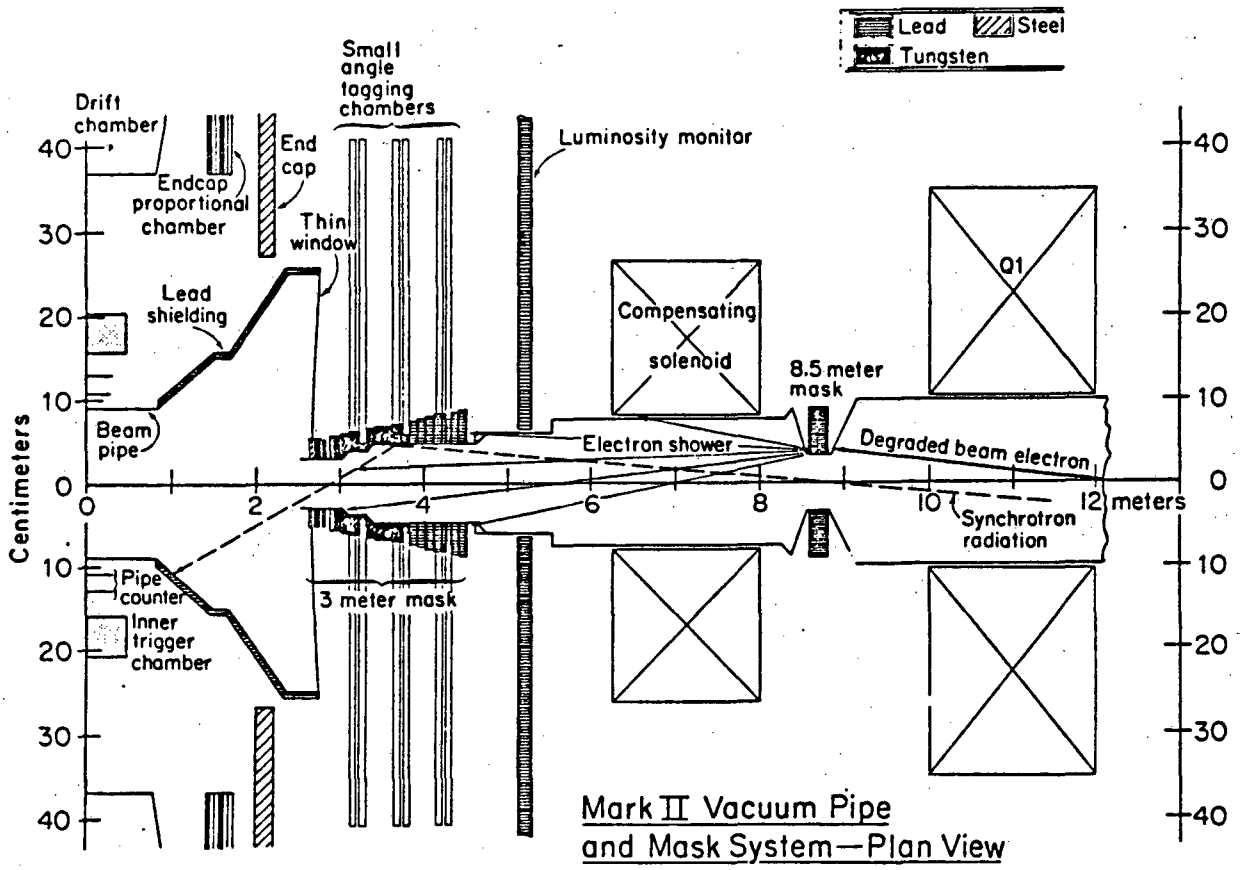

Fig. 11

XBL799-4215

Cylindrical scintilation detector ("Pipe Counter"). Signals from this device were required in the detector trigger to reduce the area sensitive to cosmic rays.

Cylindrical drift chamber ("Trigger Chamber"). This was a chamber added to the detector in the space between the pipe counter and the main drift chamber after it was moved to PEP. It consisted of four layers each containing 64 sense wires parallel to the beam direction. Incorporating signals from this chamber in the charged particle trigger helped reject background events originating at large r and z. This reduced the trigger rate by a factor of 2, hence the name trigger chamber.

Main drift chamber. Charged particle tracking was provided by this 3 m diameter chamber, which consisted of 16 layers of drift cells in a common gas volume. Six of the layers had wires parallel to the beam direction, the other 10 had wires skewed by $\pm 3°$ to provide track z information. The resolution in the distance of closest approach of tracks to the wires was about 200 μm. Taking into account the magnetic field and multiple scattering in the 0.065 radiation lengths of material (0.9 at PEP) preceeding the chambers, the transverse momentum resolution of the system was $(0.015^2 + 0.01^2 p^2)^{1/2}$. Further details may be found in reference [27].

Time of Flight (TOF) System. Flight times of charged particles were measured by a ring of 48 scintillation counters. This time, combined with the flight path and momentum determined from the drift chambers, measured the particle mass. The time resolution of the system was about 300 ps at SPEAR, giving a 1 standard deviation separation of pions from kaons up to 1.35 GeV/c, and of pions from protons up to 2 GeV/c. For PEP running, high resolution time to amplitude converters were installed in an attempt to improve this resolution [28]. However radiation damage significantly reduced the attenuation length of the scintillator, thus the resolution was degraded to about 360 ps by the end of the running discussed here.

Magnet coil. This was constructed of water cooled aluminum conductor 1.4 radiation lengths

thick, providing a nominal axial field of 4.06 kG uniform to 1.5% in the tracking volume of the drift chamber. The coil was powered in series with compensating soleniods on either side of the detector so that the integral of the field along the beam direction was zero through the interaction region. At PEP, the compensating soleniods were moved back from the detector giving a field uniform to 0.5%, and a larger power supply allowed a nominal field of 4.65 kG.

Liquid Argon System. Electromagnetic showers from electrons and photons were detected in 8 lead-liquid argon modules arranged in an octagon outside the coil. This system covered the central 65% of the detector solid angle. This system gives full azimuthal coverage except for cracks between modules, which accounted for about 10% of the 2π azimuth. The energy resolution of the system was about $12\%/\sqrt{E}$ (E in GeV). Reference [29] contains more information about this system.

Muon system. Highly penetrating particles were detected by a system of tubular proportional counters interleaved with steel absorber. At SPEAR, this system consisted of 2 layers of steel and tubes surrounding the detector, covering about 50% of the solid angle. At PEP, to compensate for the decreasing interaction probability of hadrons with increasing momentum in this energy range, 2 additional layers were installed on all four sides of the detector.

The ends of the detector were instrumented with proportional chambers (at SPEAR, one end had a liquid argon shower detector). However, these were not used in the analysis presented here and will not be discussed further.

To measure the luminosity of the machine, a system of shower detectors was used at small angles to the beam direction to detect elastic scatters. At SPEAR, this consisted of 2 tungsten-scintillator counters on each side of the detector, covering a solid angle of $1.6 \cdot 10^{-4}$ of 4π. At PEP, to compensate for the lower count rate imposed by the larger center of mass energy and the larger angles required to avoid beam associated backgrounds, a more sophisticated system,

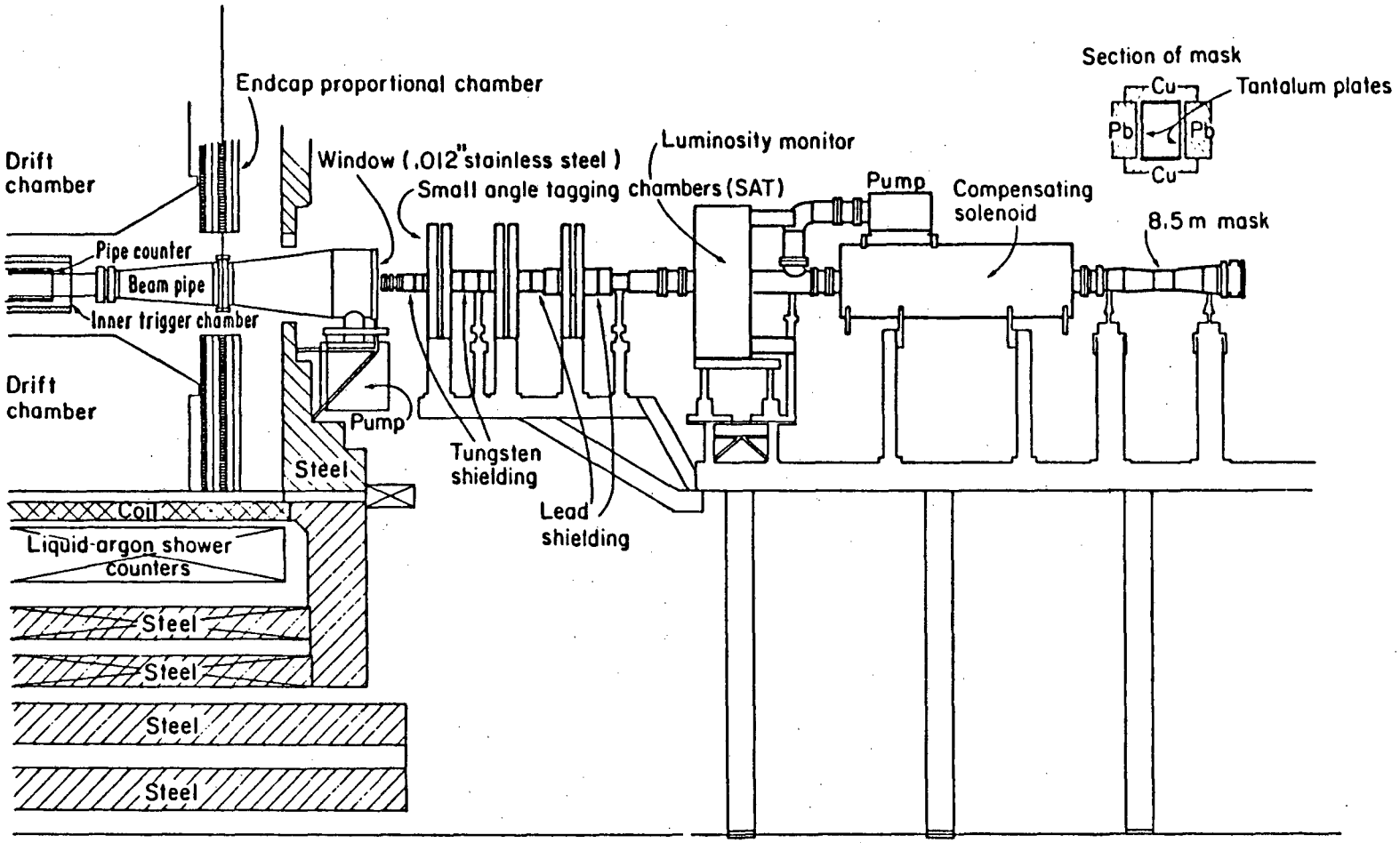

Fig. 12 The Small Angle Tagger (SAT) system. XBL 799-4216

known as the Small Angle Tagger (SAT) and shown in Figure 12, was built. On each side of the detector was an octagonal shower detector subtending the region 22 mr $\leq \theta \leq$ 80 mr consisting of eighteen layers of $\frac{1}{4}$" lead and $\frac{1}{2}$" NE114 plastic scintillator. BBQ waveshifting bars were used to transfer light to 2" phototubes. The front 5 layers were viewed separately from the back 13 to reject electrons entering from the rear and to assist in pion–electron separation if necessary. The energy resolution of these detectors was measured in a test beam to be $15.5\%/\sqrt{E}$. A series of scintillation detectors of various sizes defined the actual acceptance for luminosity monitoring. This system also contained sets of drift chambers at three positions in z on each side of the detector to track charged particles. These provided more detailed information about the events allowing a better estimate of the luminosity to be made off line (a subset of the Bhabha events were logged on tape). Besides providing a good measurement of the luminosity, this system also served to "tag" events produced via the two photon process, about which little was known and which was considered a potentially serious background to the usual one photon annihilation process.

The detector trigger was similar at both machines, employing a two-level scheme. The first level required signals from the pipe counter and a beam pickup electrode located inside the vacuum pipe to be coincident within 6 ns, and at least one hit in 4 of a subset of 9 of the drift chamber layers. This decision was made within 500 ns (which was before the next beam crossing), so there was no associated dead time. Rates varied between 10 Hz and 1 kHz, depending on beam conditions. If these primary level requirements were satisfied, a hardware processor [30] searched the drift chamber hits for patterns resembling tracks coming from the beam axis. The secondary level charged trigger required at least two tracks to be found. For the 5.2 GeV running, at least one was required to be within the central 67% of the detector solid angle and have an associated TOF hit, the other was only required to be only within the central 85% of the solid angle. For the 6.5 GeV and 29.0 GeV running, both tracks were required to be within the the central 67% of the

Process	Fraction of Triggers at 5.2 GeV	Fraction of Triggers at 29. GeV
Cosmic Rays	0.10	0.10
No Vertex	0.10	0.25
No Tracks	0.04	0.10
$Z_V > 30$ cm	0.25	0.10
1 prong	0.15	0.07
hadrons + τ	0.05	0.0015
Bhabhas	0.15	0.005
Two photon	0.01	0.02
Beam wall	0.15	0.20
SAT Bhabhas	–	0.05
TED	–	0.10

Table 1. Composition of detector triggers

detector solid angle and have associated TOF hits. In addition, in the PEP configuration there was an independent trigger based on energy deposited in the liquid argon system. This trigger was satisfied if at least 1 GeV was detected in the front half of at least 2 of the eight modules. This allowed triggering on events of the type $e^+e^- \rightarrow \gamma\gamma$ as well as providing some redundancy to the charged trigger lacking at SPEAR. Finally, the detector was triggered on some fraction, typically $\frac{1}{16}$, of the Bhabhas observed in the SAT system to obtain a precise off-line measurement of the luminosity. If any of these trigger requirements were satisfied, the detector information was read into a VAX 11/780 computer and written to tape. Typical secondary rates were 1-4 Hz, with the composition give in Table 1. A subset (20-80%) of these events were analyzed on line to monitor the performance of the detector.

§2.4 Data Reduction

Event reconstruction was done off-line on an IBM 370/168 (3081 for PEP data). First, drift chamber tracks were reconstructed. The initial level of pattern recognition started with tracks found by the hardware processor, using circle fits and a constant field approximation to resolve the left-right ambiguities. This program worked best in events with well separated tracks, due to the limited azimuthal resolution of the hardware processor. Tracks found by this program were then fit to a helix using the correct magnetic field. A more sophisiticated algorithm then searched the remaining drift chamber hits for tracks by searching for patterns of axial hits at a constant curvature. Further details regarding the track finding and fitting procedure may be found in reference [31]. For the PEP data, due to the much higher probability of two tracks passing through the same drift cell, it was necessary to use the stereo as well as the axial layers in this search. This required the assumption that the tracks came from the beam interaction point, thus biasing the pattern recognition in this data. The track finding efficiency for the SPEAR

data was greater that 99% for tracks which traversed all 16 layers, based on Monte Carlo studies and a visual scan of a computer generated pictures of events. This efficiency dropped to 80% at $|\cos\theta| = 0.8$, and was zero for $|\cos\theta| > 0.85$ since seven drift chamber hits were required to construct a track. For the PEP data, due to the much higher track density, this efficiency was reduced by about 5%. Because of the high track density at small radii and its relatively large cell size, information from the trigger chamber was not used in the pattern recognition for this analysis.

The drift chamber tracks were projected to the TOF, LA, and muon systems and associated with hits there. Photons were then searched for in the liquid argon system; details may be found in reference [32].

The event vertex was found by taking all tracks within 15 cm in radius of the beam and finding the point which minimized the summed distance of closest approach. Tracks were weighted by their measurement errors including multiple scattering. Any track which contributed more than 100 to the χ^2 of the fit was discarded, and the fit repeated. This was done to minimize displacements of the vertex by tracks from K_s or Λ decay, or which were multiple scattered or otherwise poorly measured. Finally, tracks passing within 1.5 cm in R and 15 cm in Z of the beam interaction point (determined from Bhabha events) were refit including this point. Whereas this increased the track length by about 40%, the momentum resolution was improved to $(0.015^2 + 0.006^2 p^2)$. For the PEP data, because of the bias toward the origin in the pattern recognition algorithm, only tracks with R $<$ 4 cm and Z $<$ 15 cm were included in the vertex fit. Events where no tracks were found, or where the vertex fit failed, or which had vertices with large z displacement, and cosmic rays were discarded. The remaining events were written on summary tapes.

Chapter 3

Event Selection

§3.1 SPEAR Analysis

Following the above described data reduction, remaining were Bhabha, mu pair, tau pair, and two photon events, and events from interactions of the beam with the vacuum chamber walls and the residual gas as well as hadronic events. Hadronic events were selected using cuts as loose as possible to minimize bias due to the finite acceptance of the detector, while also minimizing uncertainties in subtraction of the remaining background. To be considered as hadron candidates, events were required to contain at least two tracks satisfying the following:

1) Momentum transverse to the beam direction > 100 MeV/c. This required the track to have sufficient transverse momentum to reach the outside of the detector, thus rejecting looping tracks.

2) $|\cos\theta| \leq 0.794$. This required the track to at least reach the tenth drift chamber layer, so that the tracking efficiency was still reasonably high.

3) Radial distance of closest approach to the beam direction ≤ 6 cm.

4) Distance of closest approach along the beam direction varying from $\leq$ 30 cm for low momentum tracks to $\leq$ 5 cm for tracks with $x > 0.5$. These last two cuts reject poorly measured tracks, but were kept loose since a multiplicity cut was made.

Events resulting from interactions of the beam with the walls of the vacuum chamber were rejected by requiring the event vertex to lie within 4 cm in radius of the beam axis. This distribution is shown in Figure 13. Despite the attempts in the vertex fitting procedure to minimize distortions induced by scattered tracks or tracks from decays, an estimated $3 \pm 1\%$ of the events were lost by this cut. This loss was determined by a visual scan and study of the z vertex distribution of events with $R_V > 4$ cm. A check was provided by passing Monte Carlo generated data through the same reconstruction programs as used for the real data; this gave a loss of 2%. Whereas the Monte Carlo generally provides an optimistic simulation of the detector, this was considered a lower limit. Another estimate was obtained from events at the $\psi(3095)$. Because of the large hadronic cross section (R $\approx$ 1000) and low beam currents (making beam associated backgrounds small), the fraction of wall interactions was negligible at this energy. The fraction of events lost in this data was 4.5%. However this is probably an overestimate since the mean observed track momentum was only about 400 MeV, as opposed to 550-600 MeV at 5.2 and 6.5 GeV. Hence the tracks are more subject to multiple scattering, which combined with the lower multiplicity (4 versus 5-5.5) increases the liklihood of improperly reconstructing the vertex.

To suppress background from interactions of the beam with the residual gas, the z position of the vertex was required to be within 10 cm of the beam interaction point (Figure 14). Based on a study of Monte Carlo events and of events at the $\psi(3095)$, the loss of hadronic events due to this cut was negligible. The remaining background was estimated from events whose z vertex was in the region 10 cm $\leq |z_V| \leq$ 15 cm, assuming the z vertex distribution for such events was uniform. This contamination amounted to 8.9% at 5.2 GeV and 19% at 6.5 GeV. The

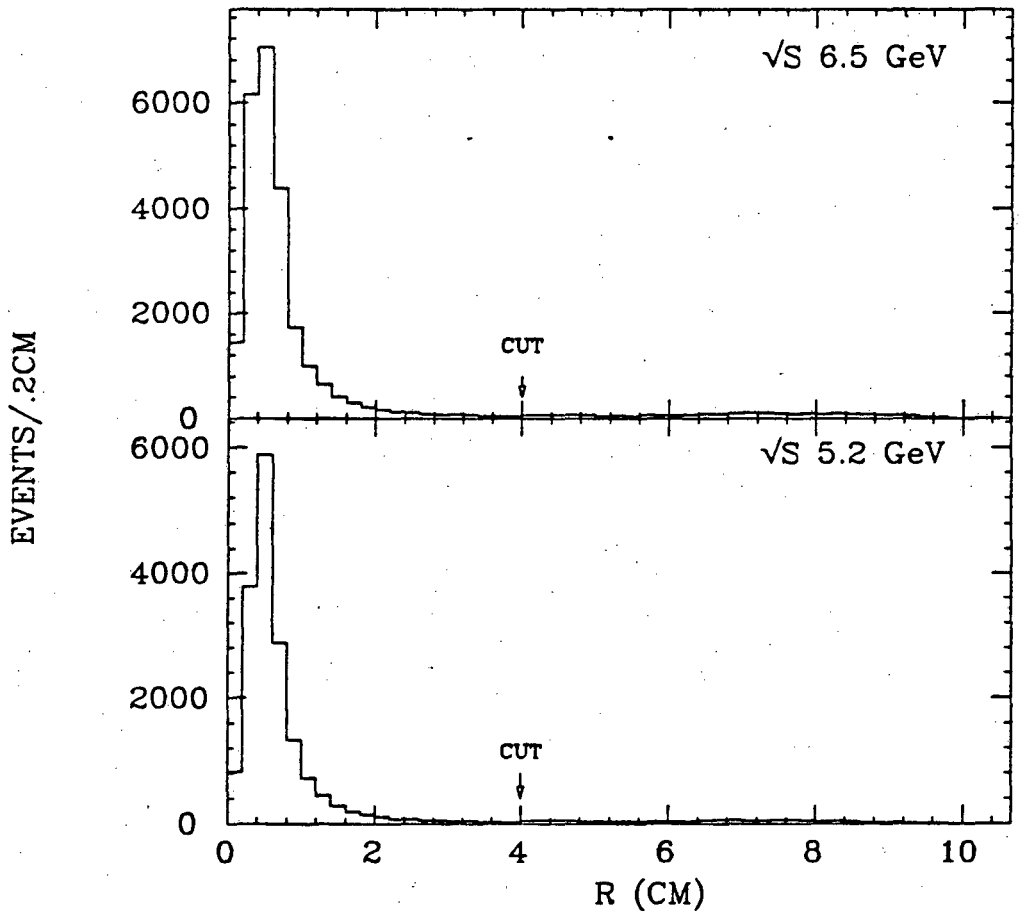

Fig. 13 Radial distribution of event vertices at 5.2 and 6.5 GeV for events meeting the hadronic selection criteria.

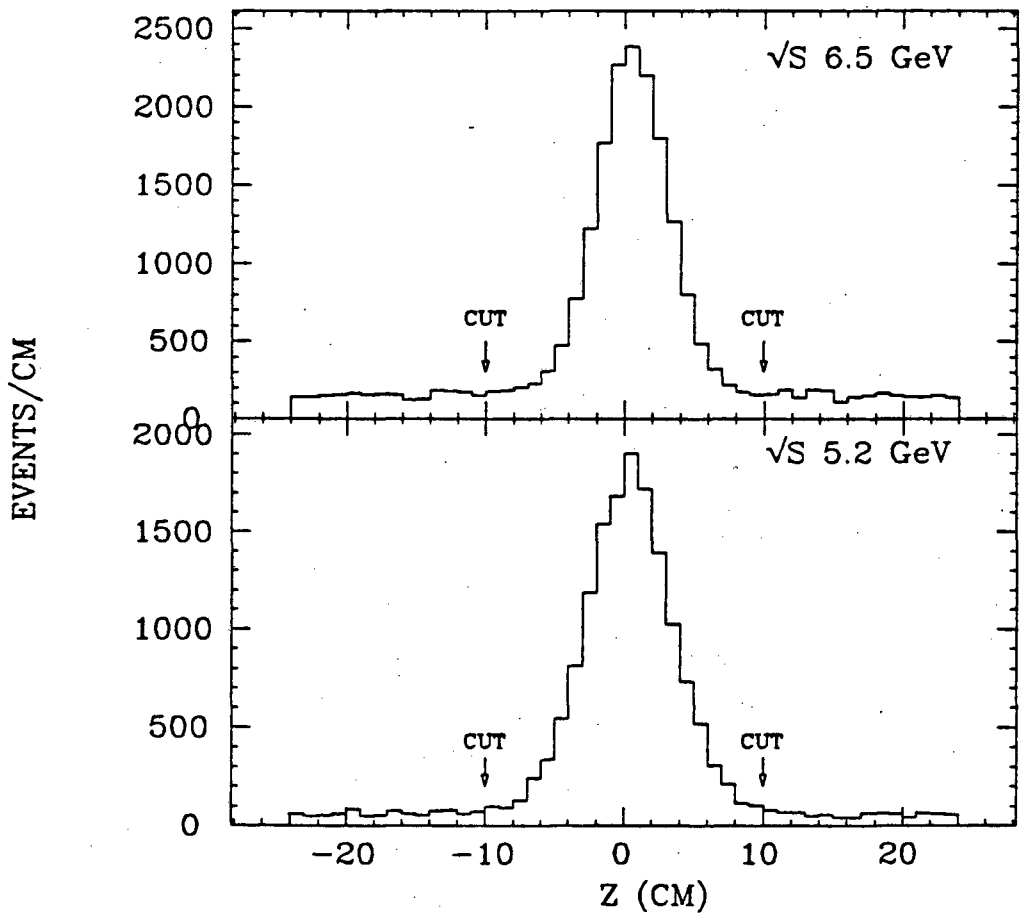

Fig. 14 Z distribution of event vertices at 5.2 and 6.5 GeV for events meeting the hadronic selection criteria.

observed z vertex distribution was in fact not perfectly uniform, as the detector acceptance was not exactly constant in z. Unfortunately, no separated beam running, which would have allowed a determination of the distribution of this background in the signal region, was done. Based on a study of this distribution for 10 cm $\leq |z_V| \leq$ 30 cm, a 10% systematic error was assigned to this subtraction.

To suppress backgrounds from QED processes, in two prong events the tracks were required to be acoplanar [33] by at least 10° and have a total transverse momentum > 300 MeV/c. To further suppress background from radiative Bhabha scattering, particularly events containing a converted photon, two and three prong events were rejected if they included a track with momentum > 900 MeV/c whose energy deposition in the liquid argon system was consistent with that of an electron [34]. Four prong events with two such tracks were also rejected. Following these cuts, background from radiative Bhabha scattering was negligible, based on a visual scan of a subset of the accepted events. Also, the distribution of $\cos\theta$ times particle charge (strongly asymmetric for Bhabha events), showed no significant asymmetry, even for tracks with $x > 0.8$. A Monte Carlo calculation was used to compute the remaining background from lepton production via the two photon process. This amounted to $3.7 \pm 0.8\%$ at each of the two energies, the uncertainty due to uncertainties in the detector simulation at low momenta and small angles, the kinematic region occupied by most of these events.

Background from $\tau^+\tau^-$ production and decay was subtracted based on a Monte Carlo generated data set using measured branching ratios. This contamination amounted to $12.2 \pm 1.8\%$ at 5.2 GeV and $9.0 \pm 1.5\%$ at 6.5 GeV. The branching ratios used are given in Table 2, they sum to a one charged prong inclusive branching ratio of 78%. Very recent measurements, without making any assumptions about particular branching ratios, have determined this number to be $85 \pm 2\%$ [35], which would reduce this subtraction somewhat. Whereas the $\pi\nu_\tau$, $\rho\nu_\tau$, $e\nu_e\nu_\tau$,

Mode	Branching ratio
$e\nu_e\nu_\tau$	0.164
$\mu\nu_\mu\nu_\tau$	0.160
$\pi\nu_\tau$	0.104
$\rho\nu_\tau$	0.230
$K\nu_\tau$	0.008
$K^*\nu_\tau$	0.015
$A_1\nu_\tau$	0.093
$4\pi\nu_\tau$	0.226

Table 2. Tau branching fractions used for background computation

and $\mu\nu_\mu\nu_\tau$ decay modes are well understood theoretically and experimentally, any discrepancy most likely is in the fraction of multi-pion decay modes which contain only one charged track. However, there still is little known about the total multiplicity, or the final state dynamics of these modes. These factors are potentially important, because of the collinearity and p_t cuts for two prong events. So from these considerations, the original branching ratio estimates were used, and a 15% uncertainty was assigned to this subtraction based on the variation in the computed background with the assumed branching ratios.

The observed charged multiplicity distribution is displayed in Figure 15, together with the estimated backgrounds. Following the background subtractions, there were 44,000 events remaining at 5.2 GeV and 11,900 at 6.5 GeV.

Because of the large background component in the two prongs, these events were were not used in the inclusive distributions. The remaining background from beam gas interactions was $5.5 \pm 0.5\%$ at 5.2 GeV and $15 \pm 1.5\%$ at 6.5 GeV; and in the inclusive distributions was confined to the region $x < 0.4$. Background from tau production was $8.6 \pm 1.3\%$ at 5.2 GeV and $6.8 \pm 1.2\%$ at 6.5 GeV. In the inclusive distributions, this varies from 4% at low x to 13% in the region $0.6 < x < 0.8$. Figure 16 displays the observed x distributions together with the estimated backgrounds.

§3.2 PEP Analysis

For the data at $\sqrt{s} = 29.$ GeV, events were required to have at least 5 tracks as defined above. Also, the sum of the particle momenta was required to exceed 7.25 GeV, or 3.75 GeV if there was also at least 4 GeV of energy in photons deposited in the liquid argon system. Relatively more stringent cuts were necessary to suppress background from hadron production via the two photon process, about which there is insufficient experimental or theoretical information

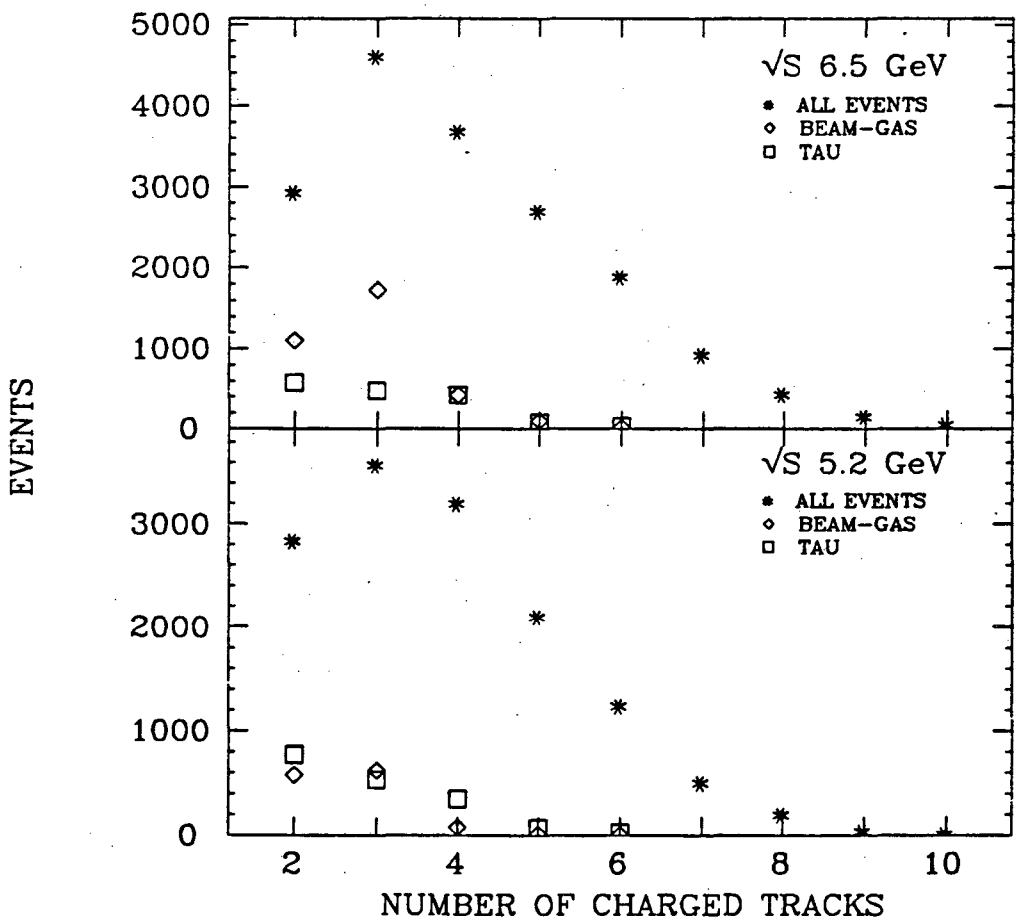

Fig. 15 Observed charged multiplicity at 5.2 and 6.5 GeV together with the estimated background contributions.

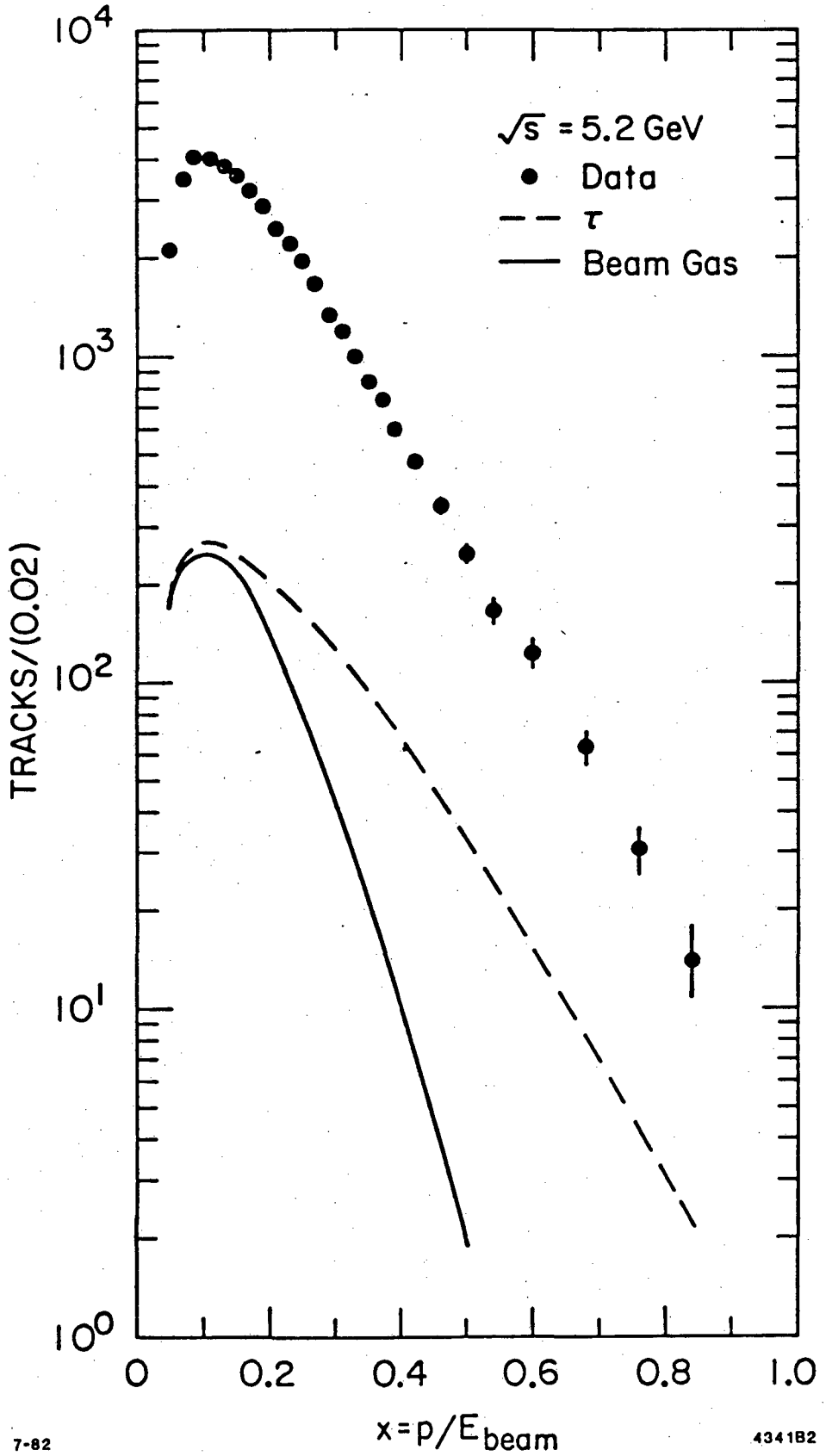

Fig. 16a Observed x distribution at 5.2 GeV together with the estimated bacgrounds.

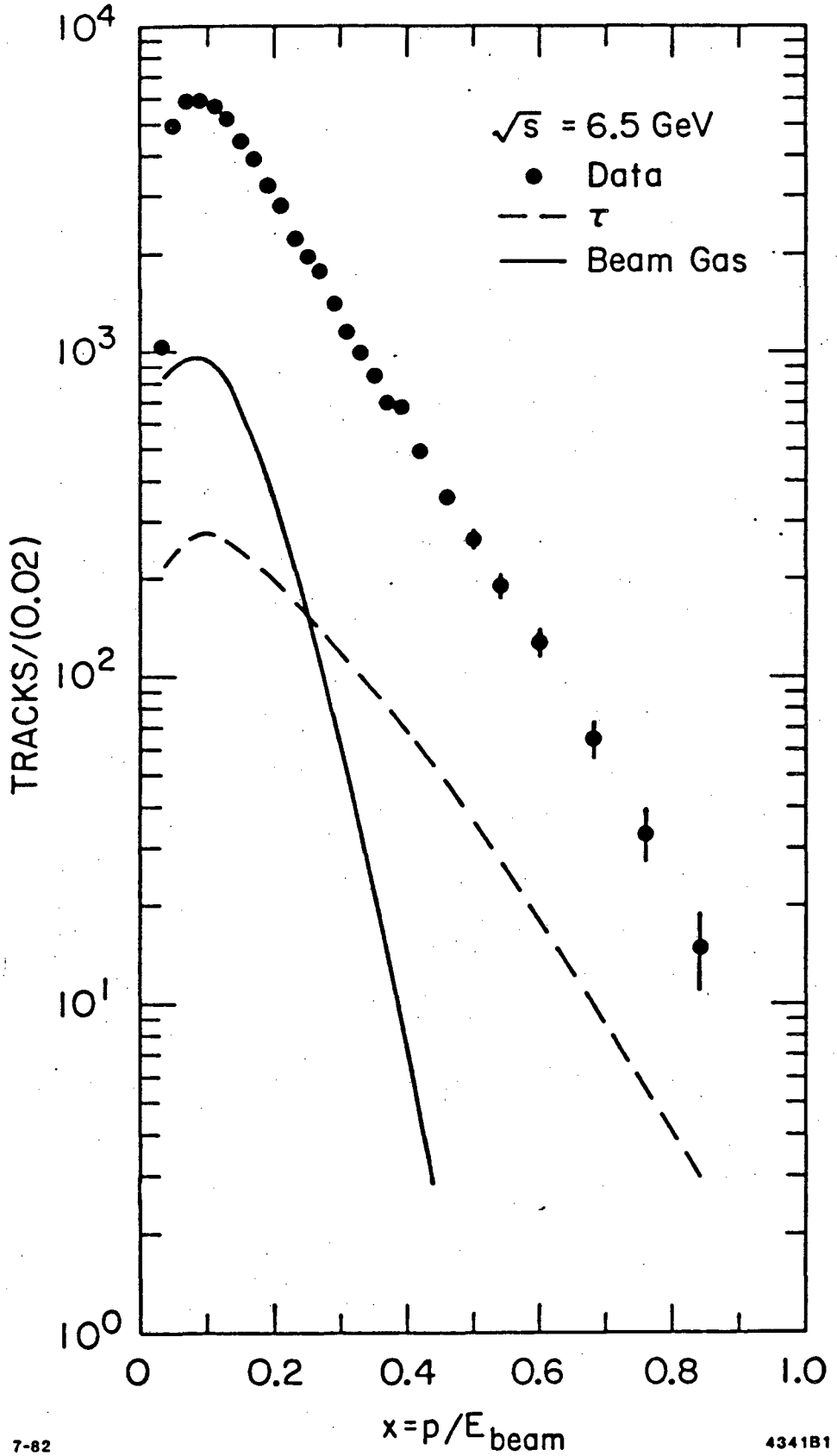

Fig. 16b Observed x distribution at 6.5 GeV together with the estimated backgrounds.

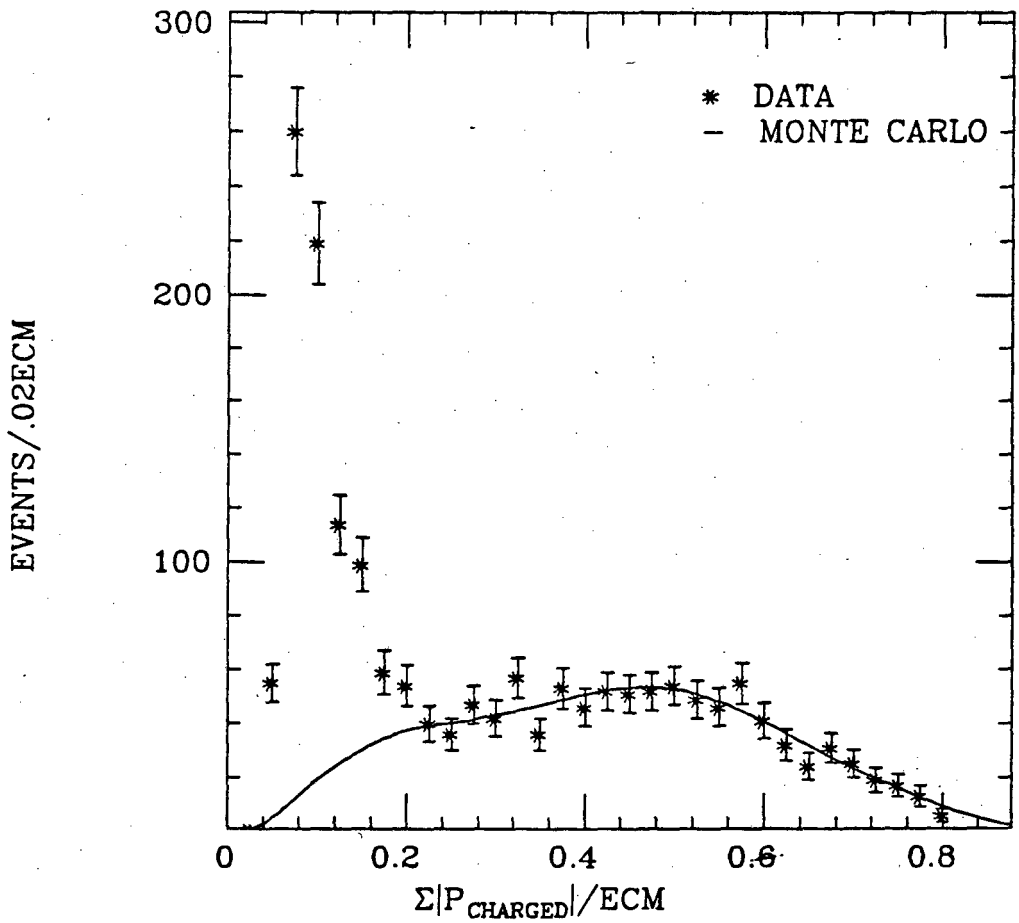

Fig. 17 Total charged momentum distribution at 29 GeV for events with at least 5 detected tracks. The curve is the prediction of the Monte Carlo discussed in Chapter 4 normalized to the number of events with $\Sigma|P| > 0.35$.

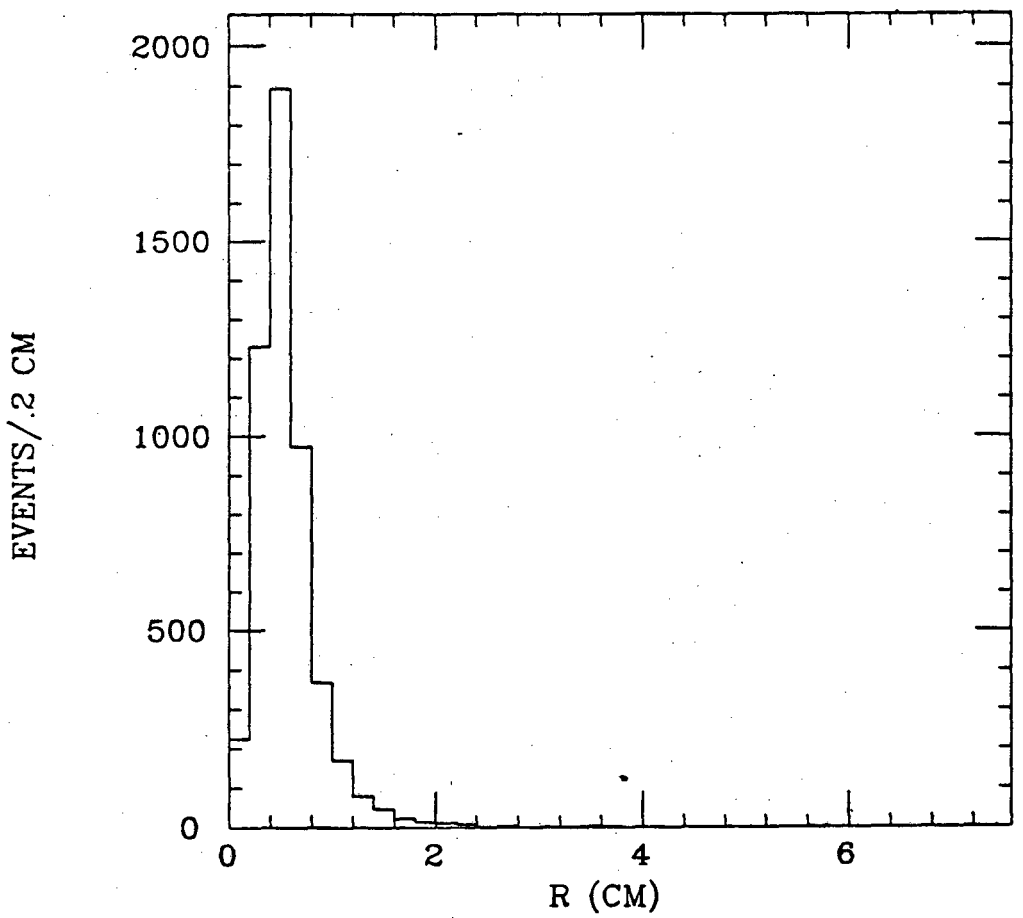

Fig. 18 Radial distribution of event vertices at 29 GeV for events meeting the hadronic selection criteria.

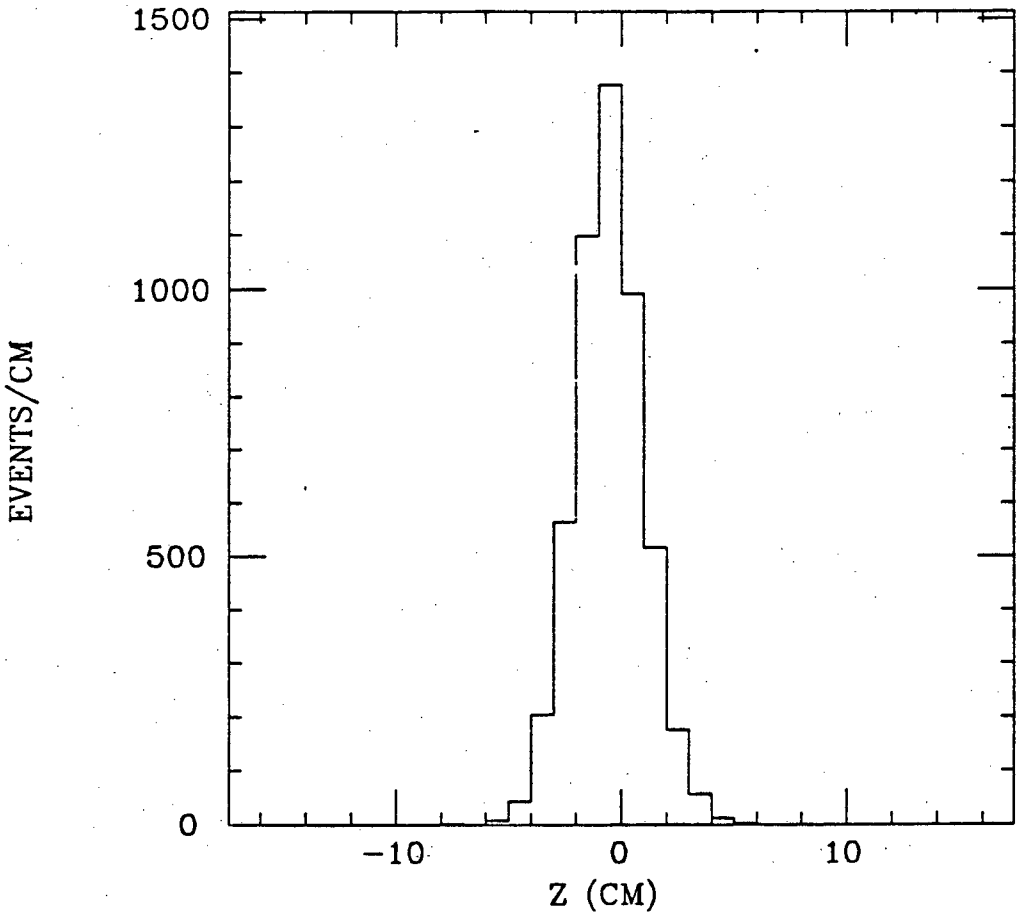

Fig. 19 Z distribution of event vertices at 29 GeV for events meeting the hadronic selection criteria.

to allow a precise subtraction to be made. This process has a much larger cross section than the standard one photon annihilation channel, although the total energy and multiplicity of the hadronic state produced is much smaller. Figure 17 shows that the background level is substantial for $\sum|P|/ECM < 0.2$, so there would be little advantage in reducing this cut. The remaining background was estimated by Monte Carlo, and from the number of events meeting these cuts where an electron was detected in the SAT system. This amounted to $1.5 \pm 0.8\%$ of the remaining events. These cuts also eliminated background from beam gas interactions, as seen in Figures 18 and 19, this would have been more difficult to estimate due to the bias toward the interaction point in the tracking algorithm used for this data. Background from tau production was computed by Monte Carlo to comprise $2.5 \pm 0.5\%$ of the remaining events. Also, using the redundancy provided by the total energy trigger, the charged trigger efficiency was found to be $> 99\%$ for these events. There were 4750 events remaining after the background subtractions.

Chapter 4

Detection Efficiency

The observed data must then be corrected for the finite acceptance and resolution of the detector. This was done using a Monte Carlo simulation, which consists of generation of particles according to some production model and projection of the particles into the detector to determine its reponse to them.

§4.1 Production Models

There is no real detailed theory of how the quarks become hadrons. So the production models can only use general expectations, namely limited transverse momentum about the initial quark direction, to generate the observed hadrons. The important thing for these measurements is that the predicted observed distributions agree with the data, giving confidence in the extrapolation to regions not covered by the detector.

The first model considered is the so called "jet" model used to first demonstrate the presence of jet structure in e^+e^- annihilation [36]. This model is known to give a good qualitative description of the data, while being fairly simple with few free parameters. In this model [37], a jet axis is generated according to a $1+\cos^2\theta$ distribution, appropriate for pointlike fermions. The

total event multiplicity is then selected according to a Poisson distribution. Finally, the particle momenta are generated according to longitudinal phase space with momentum transverse to the jet axis limited by a matrix element squared

$$|M|^2 = e^{-\sum p_i^2/2\sigma^2}. \tag{4.1}$$

Only pions and kaons are created. The fraction of kaons was chosen to agree with measurements in this energy range [38]. Thus the model does not produce vector mesons or charm particles. Free parameters in this model are the mean total multiplicity, the fraction of particles which were charged, and σ in the matrix element. To give agreement with the observed multiplicity, charged energy, and charged particle momentum distributions, the total multiplicity used was 8.8 at 5.2 GeV and 9.9 at 6.5 GeV; and 60% of the particles were taken to be charged at both energies. To give agreement with the observed sphericity distribution and distribution of p_t with respect to the jet axis, σ was taken to be 0.275. As seen in Figures 20, 21, and 22 this model gave a good description of the observed data.

The second model considered was the quark fragmentation model of Feynman and Field [39]. In this model, primary quarks are generated with a $1 + \cos^2\theta$ distribution in the ratio of the squares of their charges. Quark-antiquark pairs are then pulled from the "sea" creating mesons with fractional value of the quantity $E+P_z$ of the parent quark, Z, distributed according to the splitting function

$$1 - A + 3A(1 - Z)^2. \tag{4.2}$$

The transverse momentum of these mesons relative to the parent quarks is genererated according to a Gaussian distribution. This process continues until the initial quark energy is exhausted, the remaining quarks from each jet are combined, and the energy of the particles adjusted to give energy conservation. Free parameters in this model are A in the splitting function, the mean

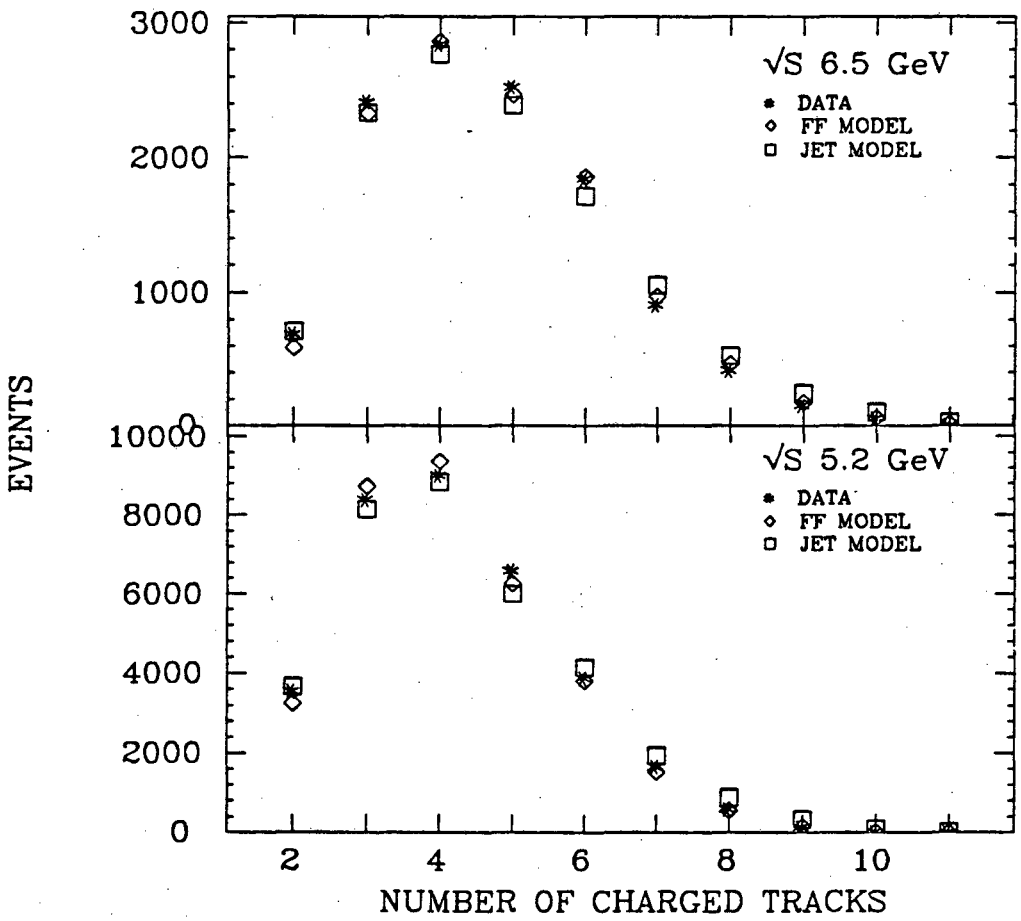

Fig. 20 Observed charged multiplicity at 5.2 and 6.5 GeV, with backgrounds removed, compared to Monte Carlo predictions normalized to the same number of events.

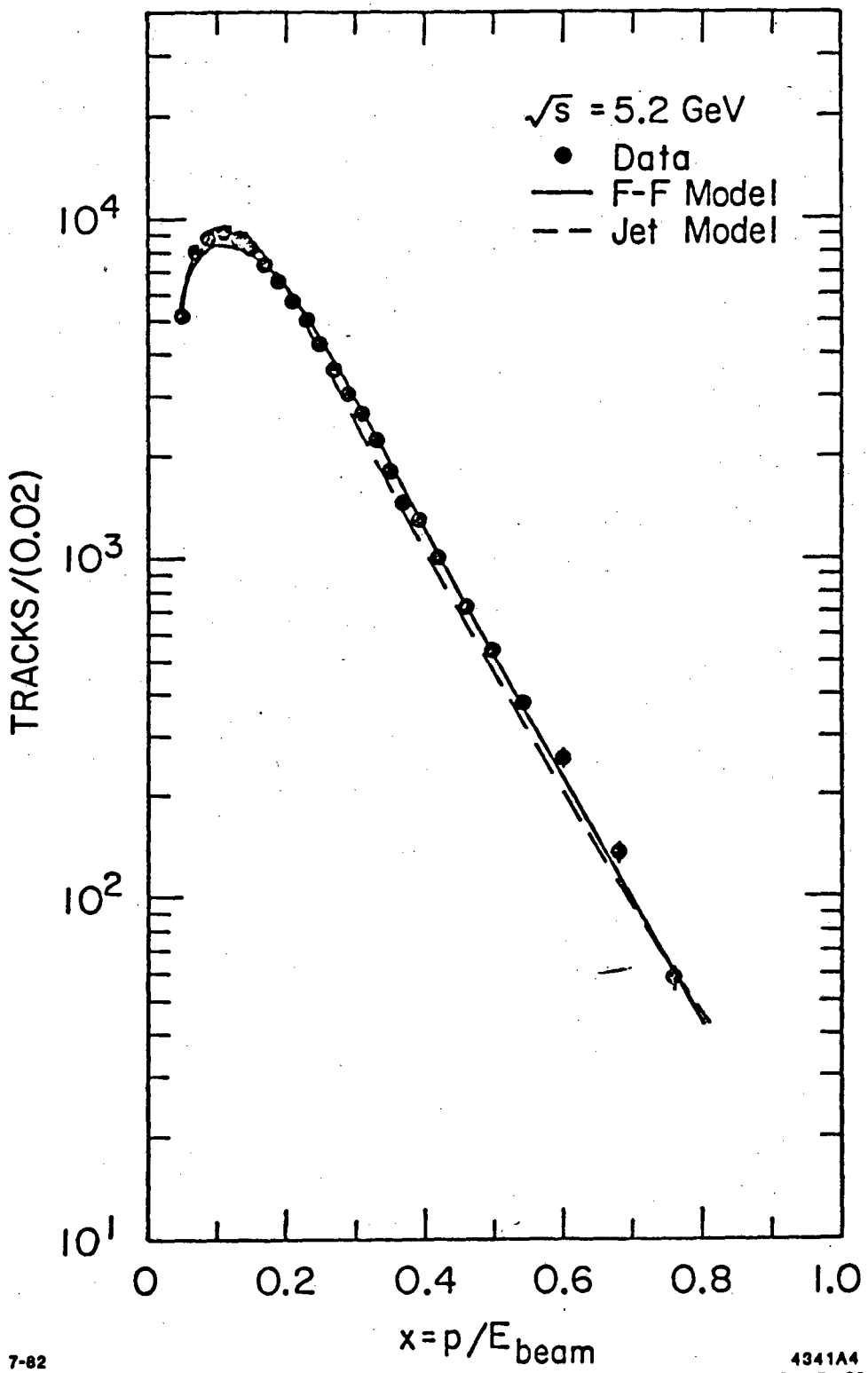

Fig. 21a Observed x distribution at 5.2 GeV, with backgrounds removed, compared with Monte Carlo predictions normalized to the same number of detected tracks.

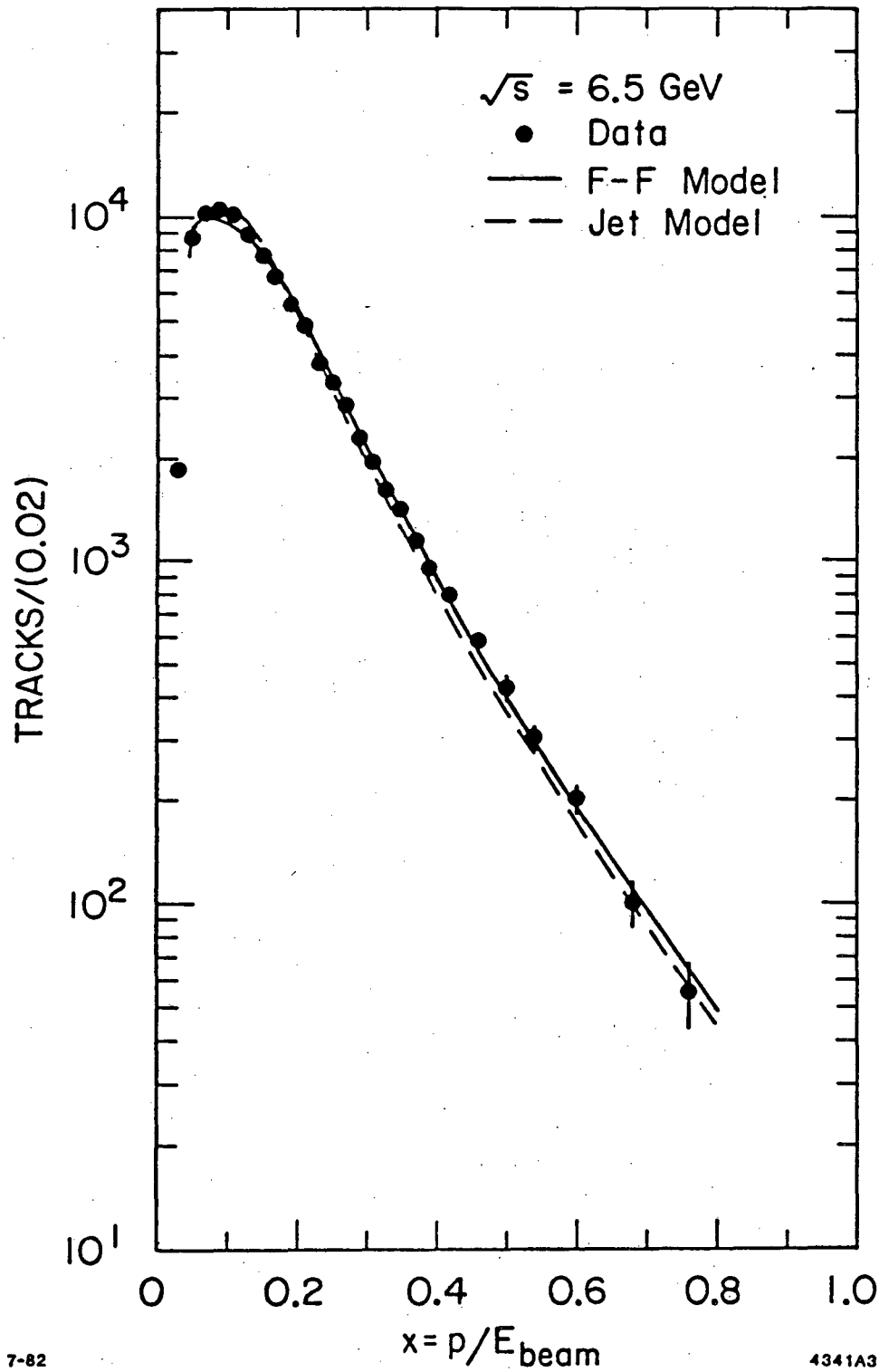

Fig. 21b Observed x distribution at 6.5 GeV, with backgrounds removed, compared with Monte Carlo predictions normalized to the same number of detected tracks.

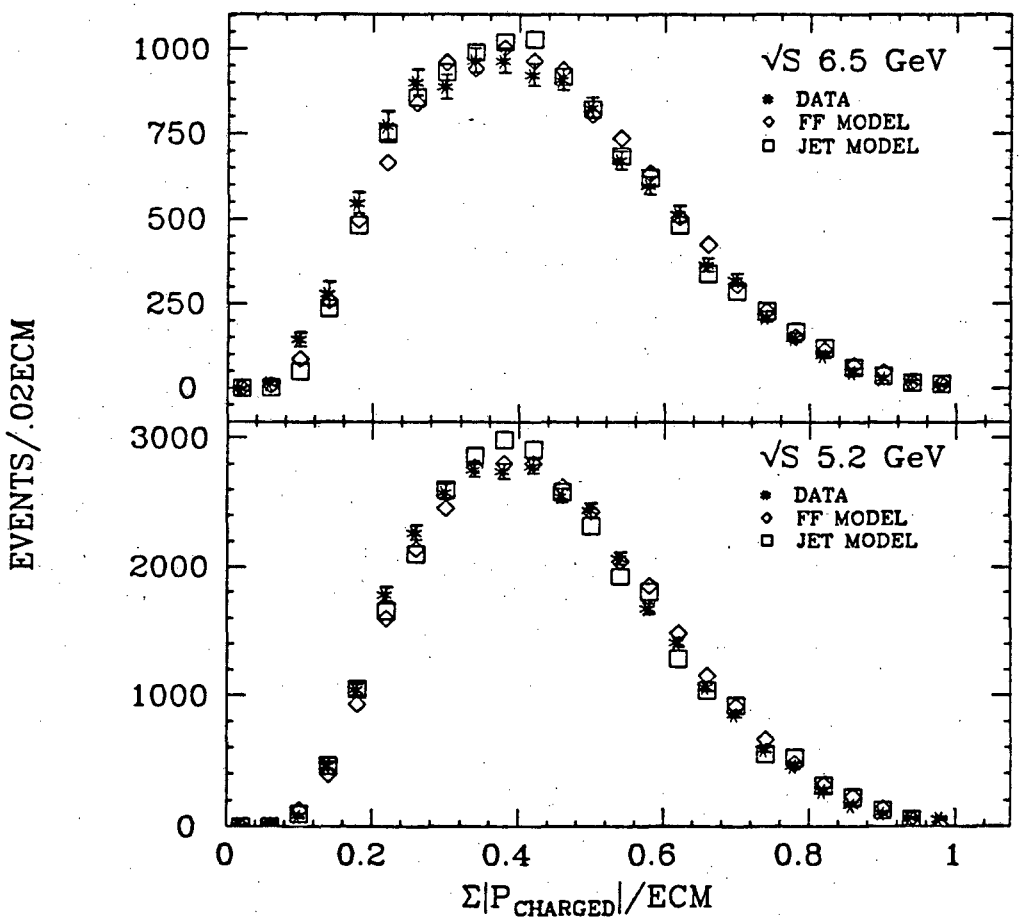

Fig. 22 Observed total charged momentum distribution at 5.2 and 6.5 GeV, with backgrounds removed, compared to Monte Carlo predictions normalized to the same number of detected events.

transverse momentum of mesons from quarks, the fraction of vector particles produced, and the probability of taking a strange quark from the sea. Parameters used to reproduce the data were A = 0.77, vector fraction = 0.1 (these primarily determine the multiplicity and momentum distributions), strange sea fraction = 0. (to give agreement with the measured K° production rate) and mean $p_t = 0.3$ (fixed by the p_t and sphericity distributions). The charm quark, due to its large mass, is expected to have a splitting function peaked at larger values of Z [40]. There is even recent experimental evidence at high energies that this is the case [41]. Whereas the exact form is unknown, a constant splitting function was used for convenience. The computed efficiencies should not be affected by moderate variations from this form. As shown in in the previous Figures, this model also gives a good overall description of the data.

At high energies, it is known that the events are more spherical than expected from extrapolation of the above two-jet models. This deviation is consistent with emission of gluons by the primary quarks. Gluon emission has been incorporated into the Feynman-Field scheme by Ali *et al.* [42]. The cross section for three jet production is given in the context of QCD by

$$\frac{d\sigma}{dx_1 dx_2} = \sigma_0 \frac{\alpha_s}{\pi} \frac{2}{3} \frac{x_1^2 + x_2^2}{(1 - x_1)(1 - x_2)} \tag{4.3}$$

where σ_0 is the lowest order cross section and x_1 and x_2 are the ratios of the quark energies to the beam energy. This cross section diverges in the limit of zero gluon energy or collinearity of the gluon with a quark. This divergence is however canceled by interference of the lowest order diagram with the fourth order vertex correction diagram, so the total cross section is well defined. To deal with this in the Monte Carlo, it is noted that following hadronization, events where the gluon is soft or collinear with a quark or equivalently the thrust [43] is large are indistinguishable from 2-jet events. So an upper limit is imposed on the thrust integration near this point of distinguishability (generally 0.95) to render the 3 jet cross section finite. The generated events should be approximately independent of this cutoff, since three jet events with larger thrust

are similar to 2 jet events [44]. Although perhaps not rigorous theoretically, what is important for this analysis is that the model reproduce the data. This program also incorporates events containing 2 gluons. A similar divergence occurs which is handled by imposing a cut on the event planarity. So 2, 3 and 4 jet events are generated with the appropriate probability. The resulting primary quark–antiquark system is fragmented as above. To generate hadrons from gluons, the gluon is first split into a quark-antiquark pair according to the function

$$f(z) = z^2 + (1 - z)^2 \tag{4.4}$$

where

$$z = \frac{\text{quark energy}}{\text{gluon energy}}$$

motivated by the Altarelli-Parisi splitting function [45]. This pair is then fragmented as above. Parameters used to reproduce the data were A = 1.0, vector fraction = 0.3, mean p_t = 0.3, Λ_{QCD} = 0.20 [46], flat splitting functions for c and b quarks, and strange sea fraction = 0.1. This model gave a good description of the observed data (Figures 23, 24, and 25)

§4.2 Detector Model

Following generation of the initial state, particles were projected into the detector generating hits in the appropriate elements, smeared by known resolutions. Particles were decayed according to known branching ratios. Branching ratios used for D mesons were based on measurements at the $\psi(3770)$ [47]. B quarks were assumed to decay predominantly to charmed quarks. Account was taken of Coulomb and nuclear interactions in the material preceeding the drift chambers. The generated raw data was then passed through the same reconstruction programs as used for real data.

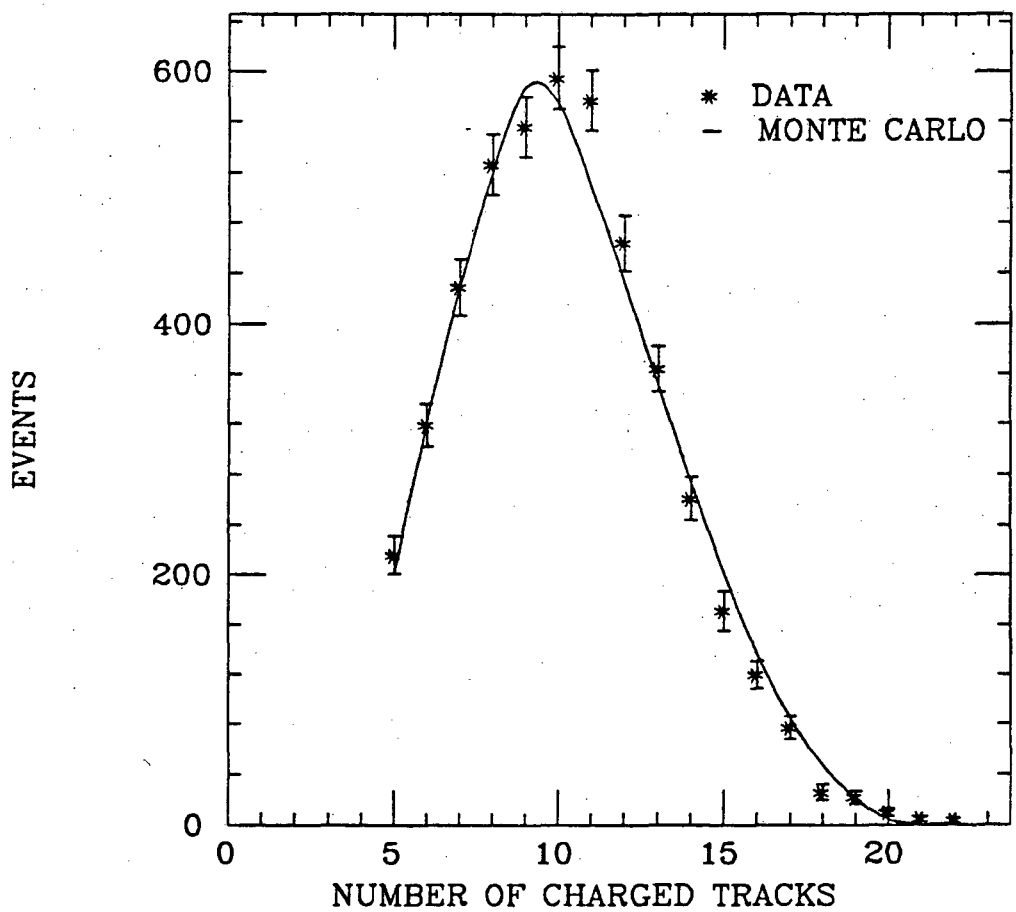

Fig. 23 Observed charged multiplicity at 29 GeV together with the Monte Carlo prediction, normalized to the same number of detected events.

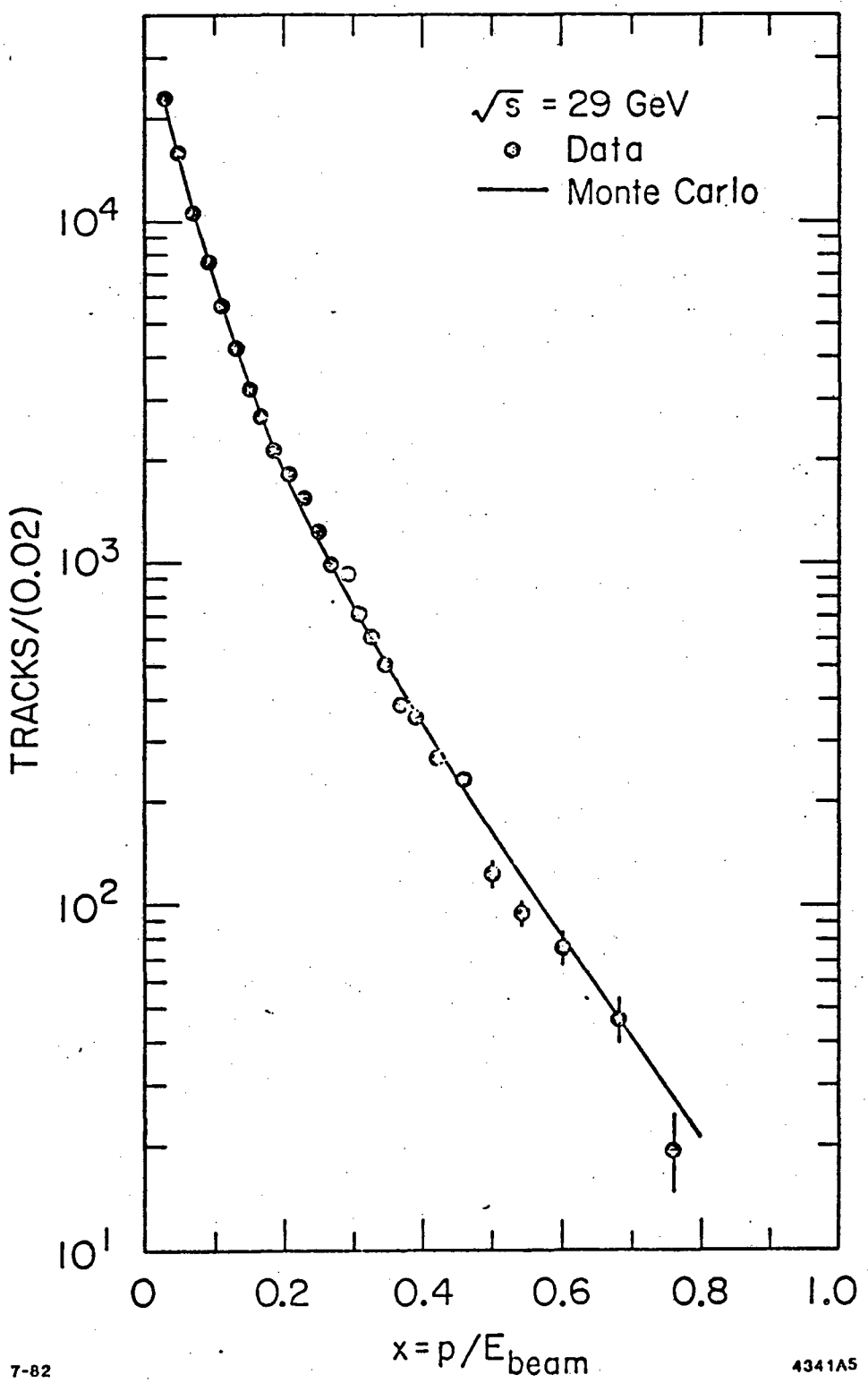

Fig. 24 Observed x distribution at 29. GeV compared to the Monte Carlo prediction normalized to the same number of detected tracks.

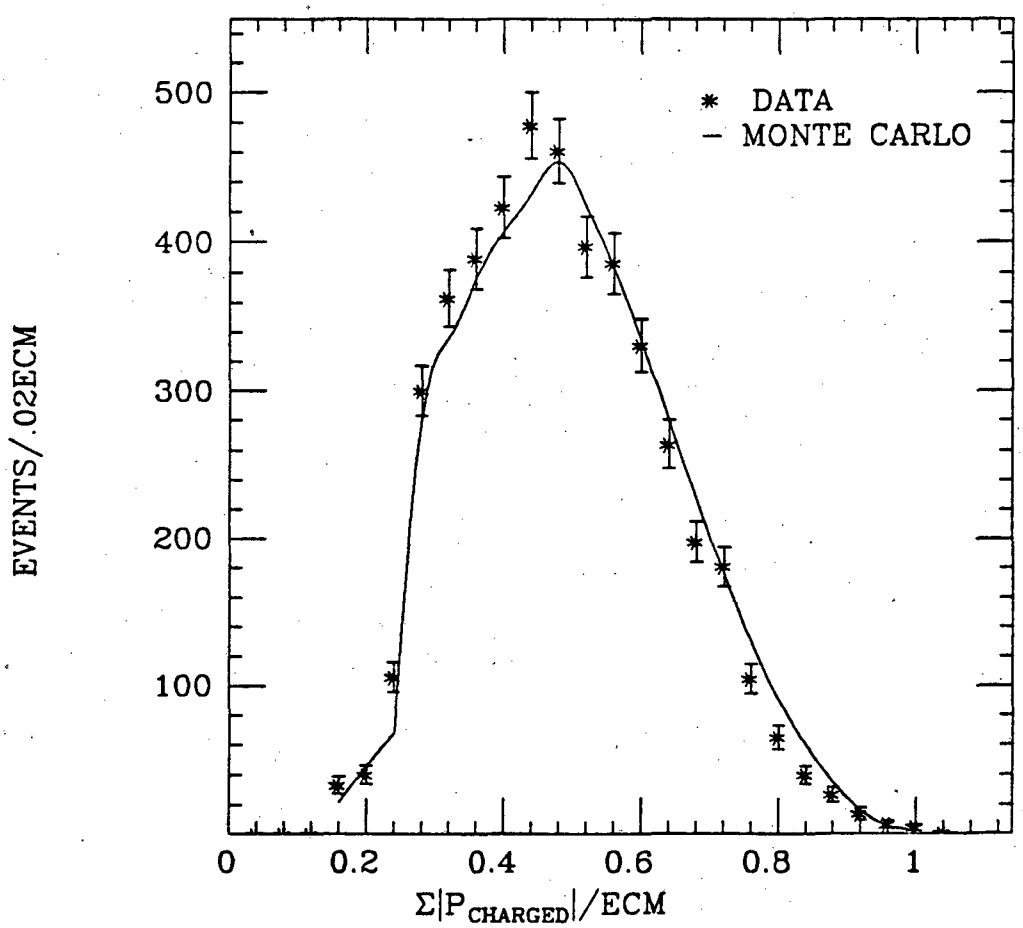

Fig. 25 Observed total charged momentum distribution at 29 GeV for events meeting the selection criteria, compared to Monte Carlo predictions normalized to the same number of detected events.

§4.3 The Unfold Method

At the low energies, since the mean produced charged multiplicity is only around 5, and two tracks must be observed for the event to be detected, the efficiency is potentially very sensitive to the production model. In an attempt to reduce this sensitivity, the detected multiplicity distribution is used as input together with the Monte Carlo to deduce the efficiency. To do this, the matrix ϵ_{qp} is defined as

$$\epsilon_{qp} = \frac{\text{Number of events detected with q prongs from events produced with p prongs}}{\text{Number of events produced with p prongs.}} \tag{4.5}$$

The total number of events detected with q prongs is then given by

$$N_q = NB_q + \sum_p \epsilon_{qp} N_p \tag{4.6}$$

where NB_q is the number of background events with detected multiplicity q. This matrix is computed using the Monte Carlo, then in principle these equations can be solved for the N_p given the observed N_q. The total efficiency is then given by

$$\epsilon = \frac{\sum_q N_q - NB_q}{\sum_p N_p}. \tag{4.7}$$

In practice these equations are over constrained since charge conservation forces N_p to be zero for odd p. So instead, the set of N_p is found which maximizes the liklihood

$$\mathcal{L} = \prod_q \frac{\mu_q^{N_q}}{N_q!} e^{-\mu_q}. \tag{4.8}$$

This function assumes a Poisson distribution for the individual N_p while making no assumptions about the shape of the produced distribution. This method reduces the model dependence of the

$\sqrt{s}$ (GeV)	Efficiency
5.2	0.77
6.5	0.81
29.0	0.74

Table 9. Total Detection Efficiencies

efficiency calculation by about a factor of two. However since the Monte Carlo agrees well with the observed multiplicity distribution, this is not a large effect.

§4.4 Results of the Models

The total detection efficiencies are shown in Table 3. The efficiency is slightly higher at 6.5 GeV than at 5.2 GeV due to the slightly higher produced charged multiplicity. The reduced efficiency at 29. GeV results from the observed energy requirement. Approximately 93% of the produced events satisfy the multiplicity requirement at this energy, but only about 80% of these events also satisfy the energy requirement.

The detection efficiency as a function of x is shown in Figures 26 and 27. At the SPEAR energies, this efficiency sharply decreases with increasing x. This is because events containing high x tracks will tend to be lower than average in multiplicity, from energy conservation considerations. So since at least three tracks must be observed, the event detection efficiency is lower for these events. The change in slope near $x = 0.7$ is due to cuts which reject radiative Bhabha events. It is noted that there is a significant difference in the overall slope of the efficiency between the jet and Feynman-Field models. This is a result of differences in the event generation procedure. In the Feynman-Field model, the two quarks fragment independently, so a high x particle in one jet may be accompanied by a a high multiplicity jet from the other quark. Thus the probability of detecting events containing high x tracks is enhanced. However in the jet model, the event multiplicity is selected first, and most high x tracks come from low multiplicity events, which are less likely to be detected. Figure 28 shows the produced charged multiplicity for events which contain a track with $x > 0.5$. This is, as expected, much lower for the jet model. Unfortunately, the difference is more difficult to observe in the corresponding detected distribution, since it is smeared from the finite detector acceptance, and because of the three track

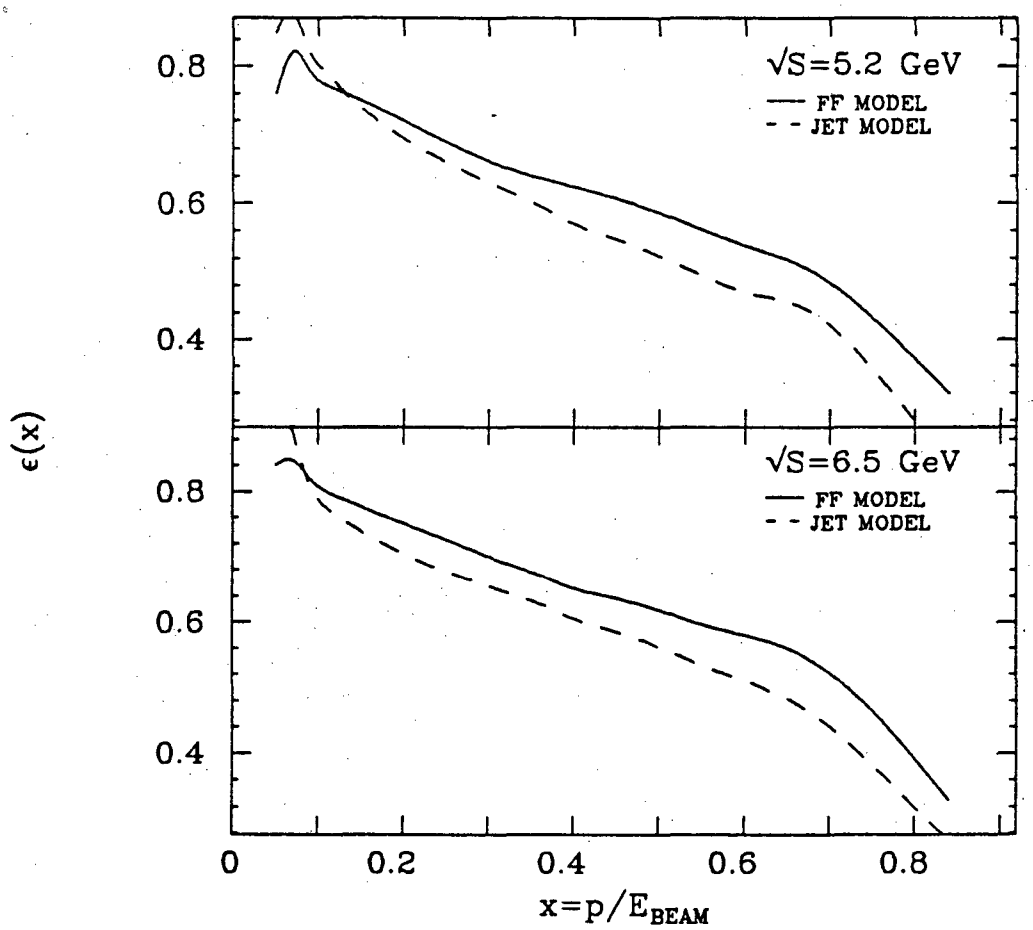

Fig. 26 Charged particle detection efficiency as a function of x at 5.2 and 6.5 GeV. Effects due to initial state radiation are included.

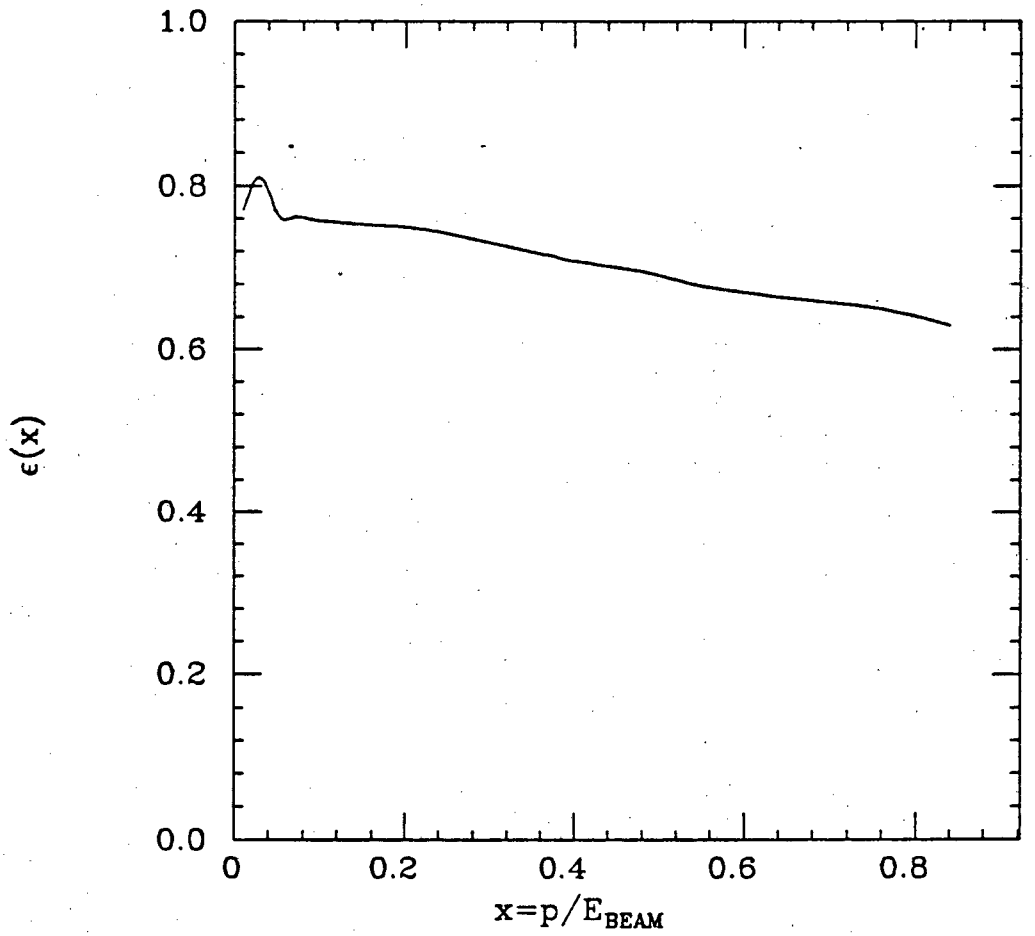

Fig. 27 Charged particle detection efficiency as a function of x at 29 GeV. Effects due to initial state radiation are included.

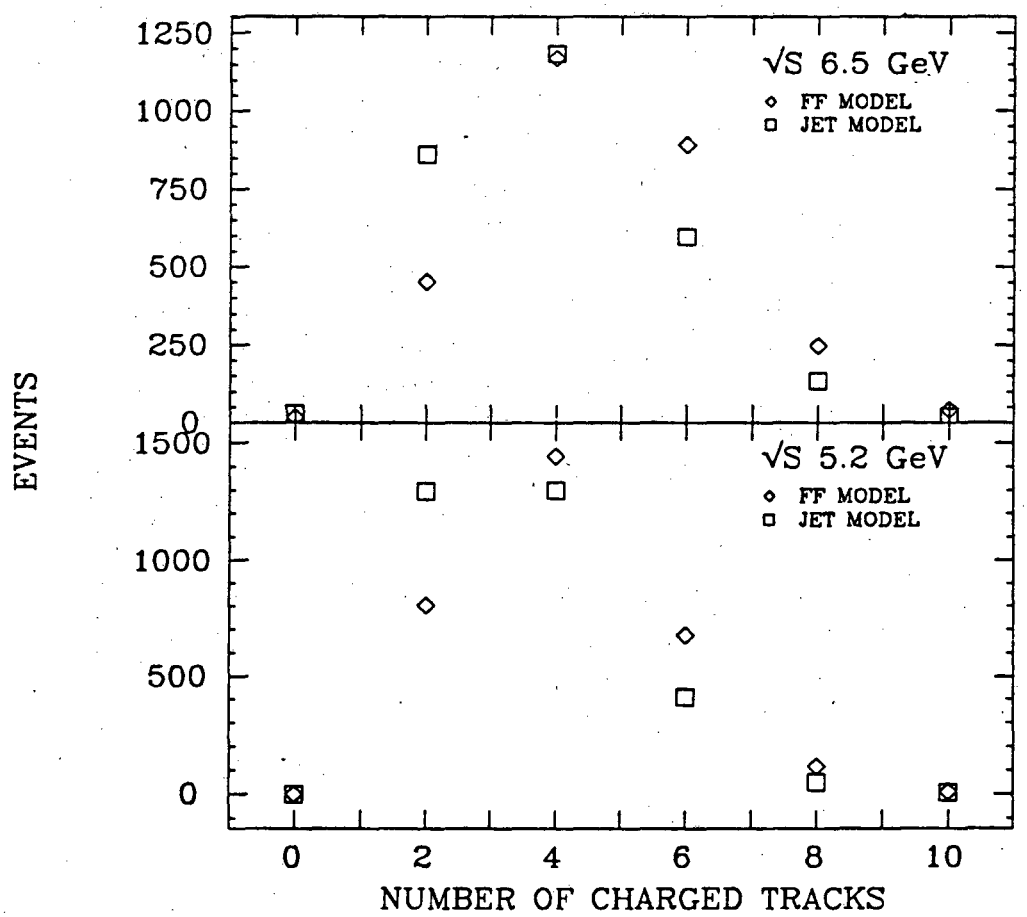

Fig. 28 Produced charged multiplicity distribution at 5.2 and 6.5 GeV for events containing a track with x>0.5.

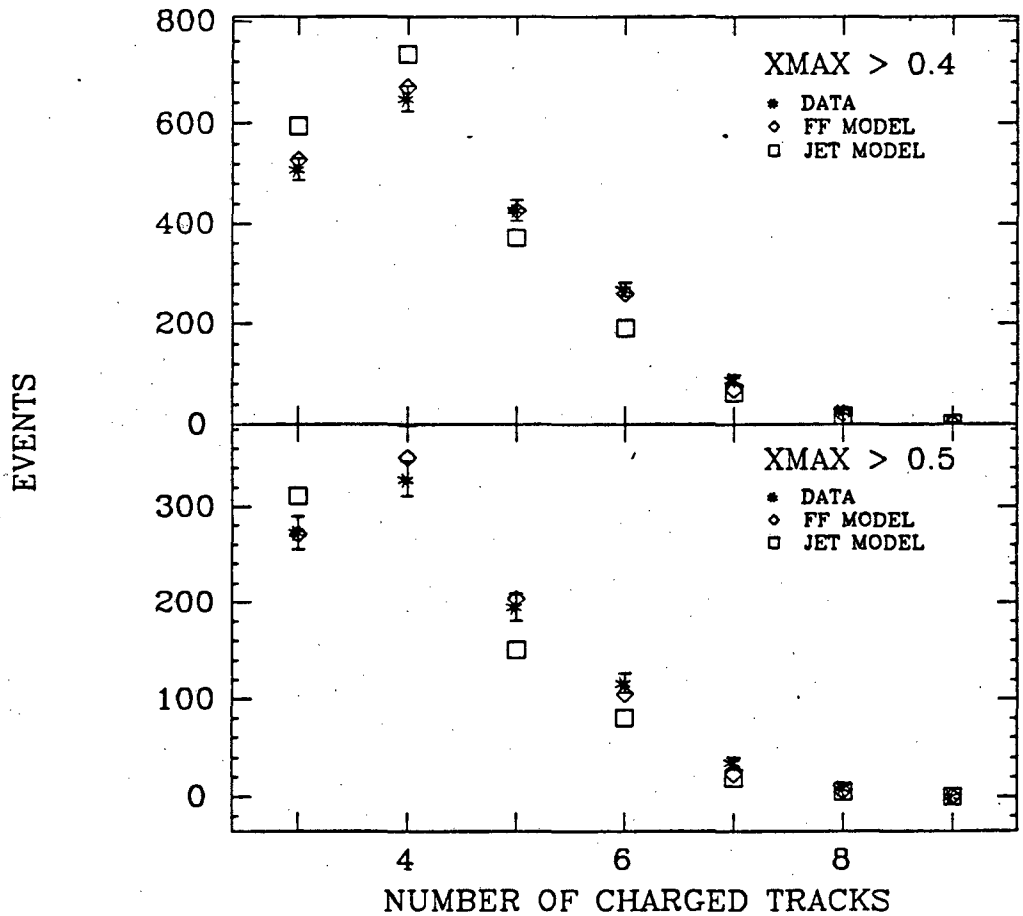

Fig. 29 Observed charged multiplicity at 5.2 GeV for events with a detected track with x>0.4 or 0.5.

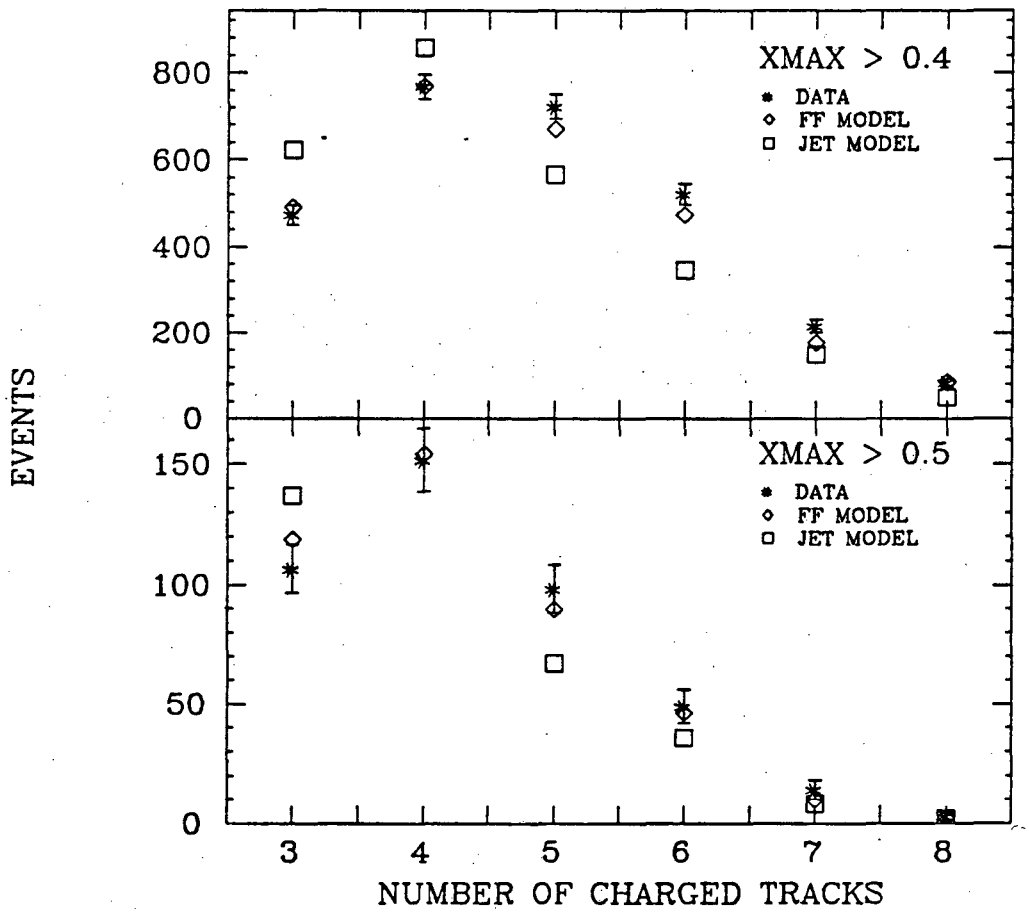

Fig. 30 Observed charged multiplicity at 6.5 GeV for events with a detected track with x>0.4 or 0.5.

detection requirement. However, the very large number of events available do allow a distinction to be made. Figures 29 and 30 show the detected multiplicity for events containing a track with $x > 0.4$ and $x > 0.5$ for the data and the two models. The Feynman-Field model is seen to clearly give a better description of the data, hence the results quoted will use the efficiencies from that model. Whereas the agreement is not perfect, a systematic error corresponding to $\frac{1}{3}$ of the difference in efficiencies between the two models is assigned to account for this effect. The efficiency at 29. GeV is much flatter due to the larger multiplicities involved, and the more collimated nature of the jets.

A test of the reliability of the efficiencies determined from the models was made by changing the event selection criteria, and noting the variation in the corrected number of events obtained. At 5.2 and 6.5 GeV, this is also a significant test of the background subtractions. In particular, the multiplicity, track $\cos\theta$ and p_t, and total momentum cuts were varied. Making these cuts more stringent increases the dependence on the production model used in the Monte Carlo. However, this does remove regions at large angles and low momentum where the detector simulation is less reliable, lessening the dependence on that part of the Monte Carlo. Varying the cuts also affects the slope of the efficiency as a function of x. Raising the total charged momentum cut enhances the relative efficiency at high x, while increasing the multiplicity cut relatively enhances the low x efficiency. In doing this within reason, the number of corrected events changed by at most 3%. The change in the corrected inclusive distributions was generally less than 3%, giving some confidence in the model used to compute the efficiencies.

To further investigate the uncertainty in the efficiencies, several other production models were used. Among them was the LUND [48] model, which employs a different fragmentation scheme for both quarks and gluons. Also tried was a "higher twist" model which replaced gluon emission by an *ad hoc* function added to the usual Gaussian p_t distribution to reproduce the

observed broadening of the sphericity and p_t distributions. The function used was

$$A\,e^{-p_t^2/2\sigma^2} + B\,\frac{1}{(C^2+p_t^2)^2} \tag{4.9}$$

where A, B, and C were adjusted to fit the data. The efficiency was even computed neglecting gluon emission entirely, although this does not reproduce certain aspects of the data. With parameters adjusted to give agreement with the observed data (except in the latter case), the efficiencies varied by at most 4%.

Based on all these studies, the uncertainty in the total efficiencies was estimated to be $\pm 4\%$. The uncertainty in the inclusive efficiencies was estimated to be $\pm 4\%$ rising to $\pm 7\%$ at high x due primarily to the aforementioned model uncertainty.

Chapter 5

Radiative Corrections

The goal of these measurements is by convention to determine the cross section for the process, that which is lowest order in α. However there are higher order processes not necessarily distinguishable from the lowest order process included in the detected sample, which therefore must be corrected for.

Diagrams contributing to hadron production to order α^3 are shown in Figure 31. These include diagrams where the initial electron or positron radiates a photon, as well as interference between the lowest order diagram and the fourth order vertex correction, electron self energy, and photon self energy (vacuum polarization) diagrams.

Computation of these diagrams, assuming factorization of the initial state radiation from the final state hadron production, gives the following relation between the second and third order cross sections [49]:

$$\sigma(s) = \sigma_0\left(1 + \delta_1 + \int_{k_{min}}^{E_b} dk(1 - \frac{k}{E} + \frac{k^2}{2E^2})\frac{\sigma_0(4E(E-k))}{\sigma_0(4E^2)}\right) \tag{5.1}$$

where

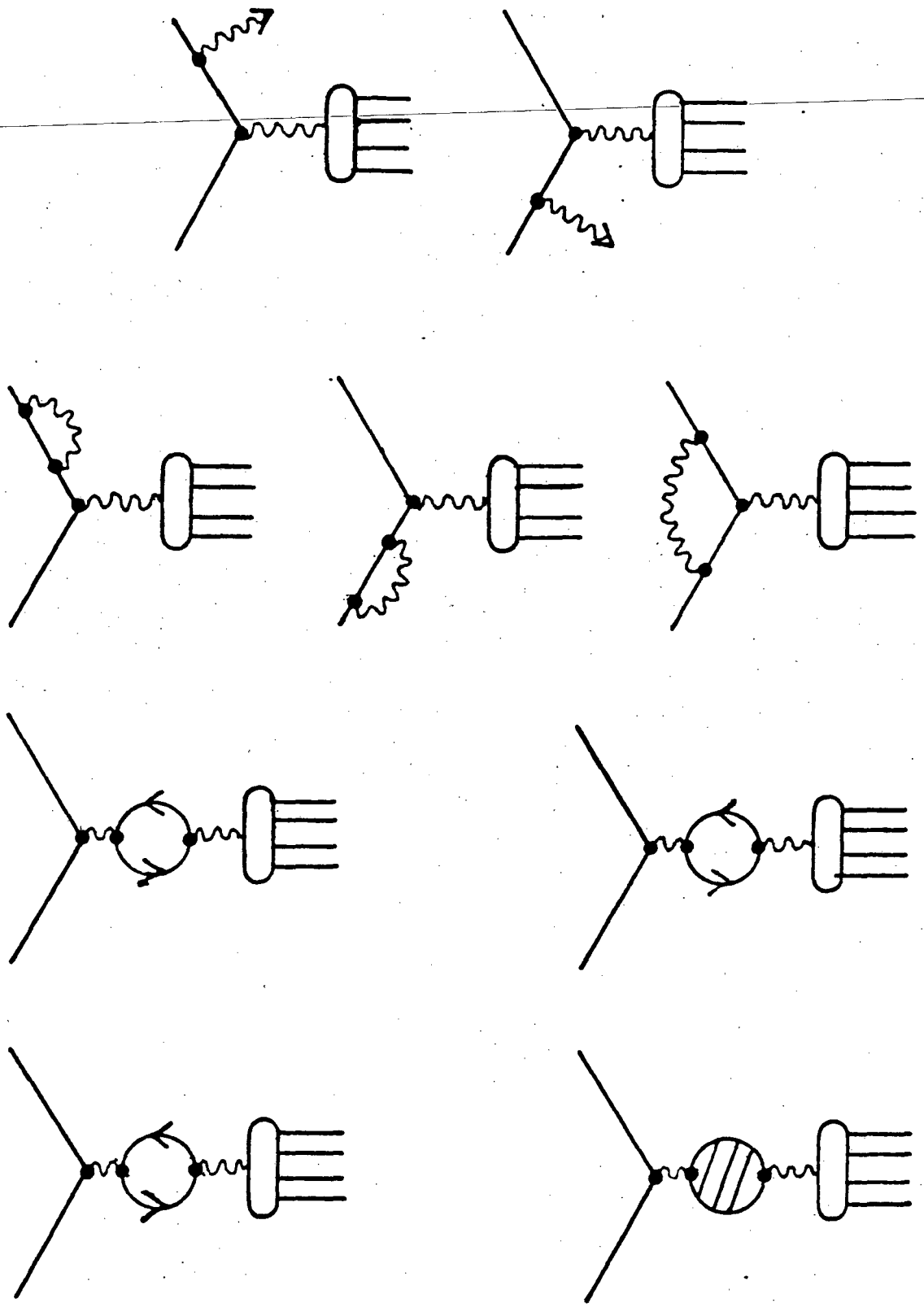

Fig. 31 Diagrams contributing to hadron production of order α^3.

$$\delta_1 = \delta_e + \delta_\mu + \delta_\tau + \delta_h$$

$$\delta_e = \frac{2\alpha}{\pi}(\frac{\pi^2}{6} - \frac{17}{36}) + t(\frac{13}{12} + \ln\frac{k_{min}}{E})$$

$$\delta_{\mu,\tau} = \frac{2\alpha}{\pi}\left(\frac{1}{3}\ln(\frac{s}{m^2_{\mu,\tau}} - \frac{5}{9})\right)$$

$$\delta_h = \frac{-s}{4\pi^2\alpha}\int_{4m_\pi^2}^{\infty}\frac{\sigma(s')ds'}{s'-s}$$

$$t = \frac{2\alpha}{\pi}(2\ln\frac{2E}{m_e} - 1)$$

$$m_{e,\mu,\pi,\tau} = \text{mass of e, } \mu, \pi, \text{ or } \tau$$

The δ_1 term contains contributions from initial state radiation of a photon of energy $k < k_{min}$ and from the virtual corrections shown in c) of the previous figure. The integral term comes from initial state radiation of a photon with energy $k > k_{min}$ followed by annihilation at the reduced center of mass energy $(4E(E-k))^{1/2}$. These terms are separately divergent in the limit $k_{min} \rightarrow 0$, however the sum is finite, thus the total cross section is well defined. In events where a photon is emitted the annihilation occurs in a different rest frame than the lab frame as well as at a lower center of mass energy, thus these events will have a different detection efficiency from non-radiative events. Therefore the integral must include the ratio of the efficiencies at the initial and reduced center of mass energies. So σ_0 can in principle be computed by determining the detection efficiency as a function of s and using the above relation.

An alternative is to note that events where the photon is soft are in practice indistinguishable from lowest order events. Thus k_{min} can be left at some non-zero value (generally taken to be 1% of the beam energy), then the cross section for events with no hard photon is given by

$$\sigma = \sigma_0(1 + \delta_1). \tag{5.2}$$

The effective efficiency then becomes

$$\epsilon_R = \frac{\text{detected events}}{\text{produced events with no hard photon}}(1+\delta_1). \tag{5.3}$$

Also, the ϵ_{qp} matrix becomes

$$\epsilon_{qp} = \frac{\text{Number of Events with q prongs from produced with p prongs}(1+\delta_1)}{\text{Number of Events produced with p prongs and no hard photon}}. \tag{5.4}$$

The particle detection efficiency as a function of x becomes

$$\epsilon(x) = \frac{\text{Number of tracks detected within } x \text{ and } x+dx(1+\delta_1)}{\text{Number of tracks produced within } x \text{ and } x+dx \text{ in events with no hard photon}}. \tag{5.5}$$

To compute the efficiencies, the Monte Carlo is modified to generate events with the appropriate distribution of photon energies. Non-radiative events are generated with probability

$$\frac{(1+\delta_1)}{(1+\delta_1+\int_{.01E_b}^{E_b} dk(1-\frac{k}{E}+\frac{k^2}{2E^2})\frac{\sigma_0(4E(E-k))}{\sigma_0(4E^2)}}. \tag{5.6}$$

Photon energies for radiative events are generated according to the integrand in equation 5.1, using measured values of the total cross section at the lower center of mass energies. If the event contains a hard photon, its angle with respect to the positron direction is given the following distribution function [50]:

$$\frac{\alpha}{2\pi sk}\sigma^0(s')\left(-\frac{4m^2s'}{s}J_1 - 4k^2J_2 + s(1+\frac{s'^2}{s^2})J_3\right)$$

$$\begin{aligned} J_1 &= \frac{1}{1-\cos\theta_\gamma} - \frac{1}{1+\cos\theta_\gamma} \\ J_2 &= \cos\theta_\gamma \\ J_3 &= \ln\left(\frac{1+\cos\theta_\gamma}{1-\cos\theta_\gamma}\right) \end{aligned} \tag{5.7}$$

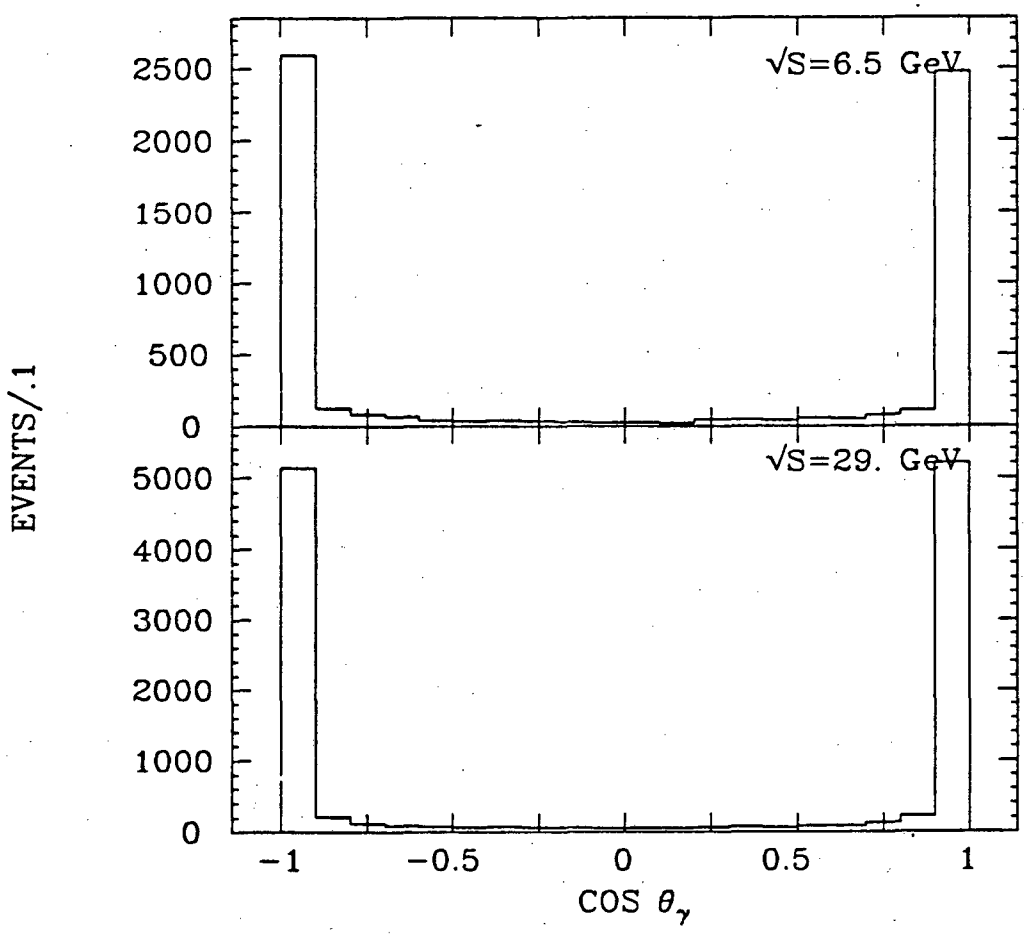

Fig. 32 Angular distribution of radiated photons.

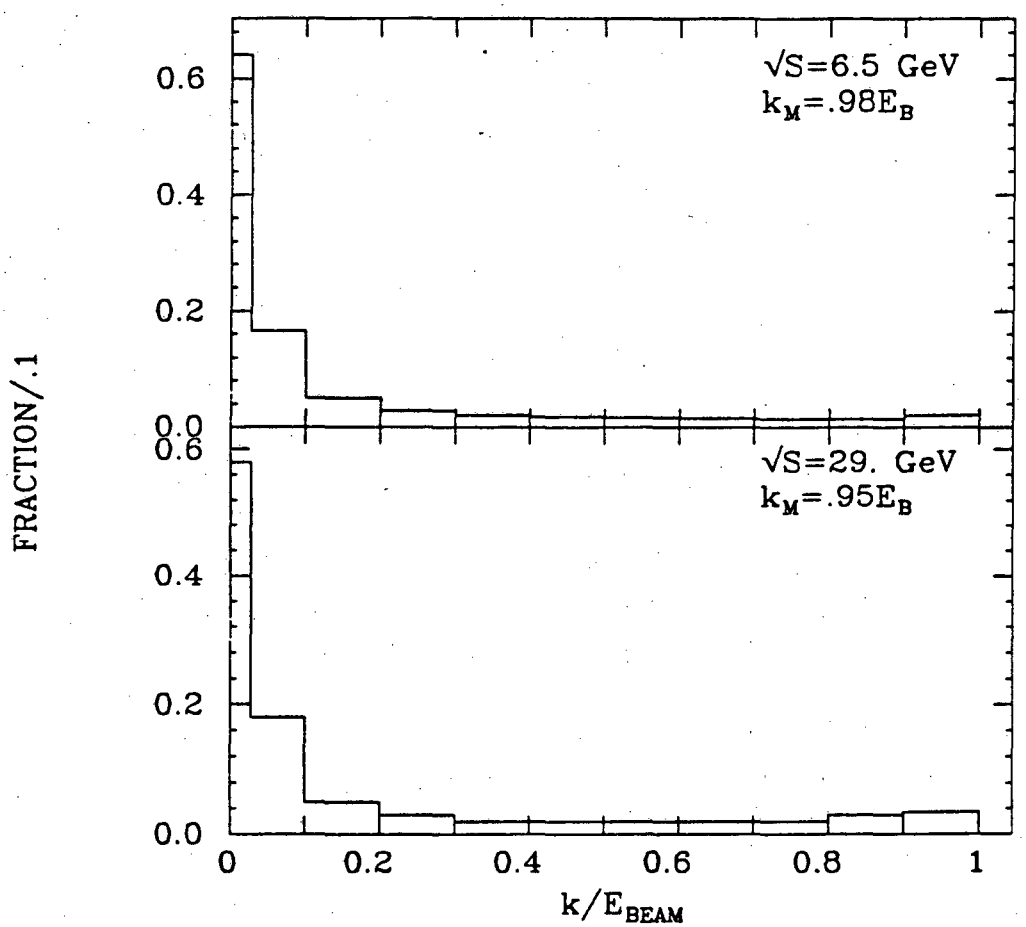

Fig. 33 Energy distribution of radiated photons.

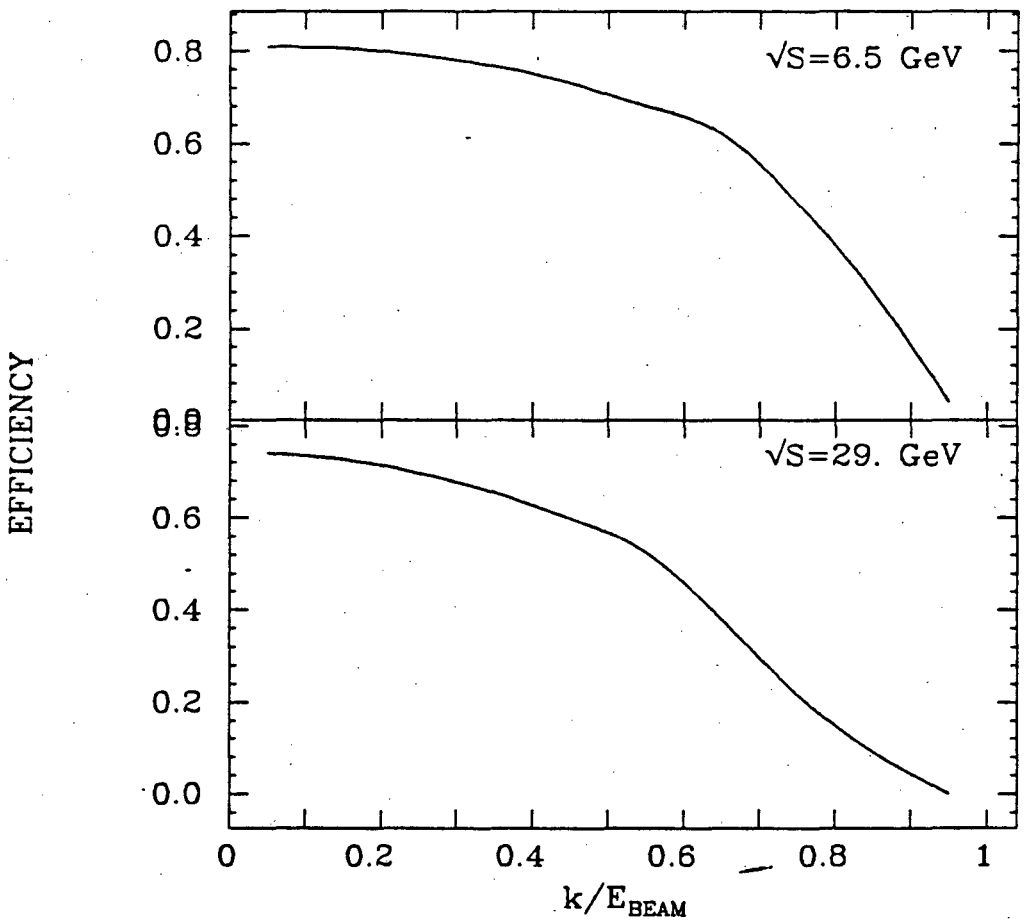

Fig. 34 Detection Efficiency as a function of the radiated photon energy.

where θ_γ is the photon angle with respect to the positron direction in the lab frame. The generated distribution, integrated over photon energies is shown in Figure 32. Photon generation is cut off at some maximum energy k_{max} (typically 0.95 times the beam energy) since highly radiative events are lower in multiplicity and are strongly boosted along the beam direction. This lowers their detection efficiency such that they make a small contribution to the numerator in equation 5.3. This also avoids uncertainties in the cross section for $\sqrt{s} < 1$ GeV, where there is complicated resonant structure. Also, because the annihilation cross section rises faster than the photon energy spectrum falls, setting k_{max} too close to 1 would result in mostly radiative events being generated, which would not be computationally efficient. Figure 33 shows the generated distribution of photon energies, and Figure 34 shows the detection efficiency as a function of this energy.

The net result of these effects is to increase the effective total efficiency by 10% at the SPEAR energies and by 15% at 29.0 GeV. For the inclusive distributions, this correction is about 10% (15% at 29 GeV) at low x falling to less than 5% at high x. The correction is smaller for high x since highly radiative events cannot produce high x tracks.

Uncertainties in the radiative corrections come from lack of knowledge of the relative cross section and production model at energies below the nominal center of mass energy, from the calculation itself as well as possible higher order corrections not considered here. For the 29 GeV data, R is believed to have no significant structure down to 11 GeV, corresponding to a photon energy of 0.85 E_{beam}. So this is not much of a problem for this data. However, for the SPEAR energies this cross section has complicated structure in the region $3.7 \leq \sqrt{s} \leq 4.5$ GeV, which furthermore has not been measured with great precision. Different forms of the cross section in this region, even including a constant R, were tried to estimate the uncertainty in the radiative correction due to uncertainties in the cross section in this region.

This correction also requires extrapolation of the production model to lower energies, where less may be known about the properties of the events. In particular, for the SPEAR data properties of the events at resonances may be somewhat different from the surrounding continuum. And for the PEP data measurements are sparse (none have been made with the Mark II detector) in the region below 29 GeV. This uncertainty is estimated by studying the variation of the correction with different production models.

Finally, higher order diagrams have not been included, a crude estimate of their possible contribution is made by squaring the magnitude of the correction. This therefore gives a larger contribution to the uncertainty at 29 GeV.

The contribution to the uncertainty in the total cross section is taken to be $\pm 2.5\%$ at 5.2 and 6.5 GeV, dominated by uncertainties in the cross section and production model at lower energies. At 29 GeV, this uncertainty is estimated to be $\pm 3\%$, dominated by possible higher order corrections.

Finally, it should be noted that no correction is made for final state radiation (off the quark lines). Naively, one would expect this correction to be much smaller than the initial state radiative correction because of the large mass of quarks relative to electrons. However since this process competes with gluon emission, a proper calculation must include both, as well as interference between initial and final state radiative diagrams. Several such calculations have been attempted [51], however pending further theoretical and experimental work, the results quoted here will not include final state radiative corrections.

Chapter 6

Normalization

Whereas the beam parameters in an e^+e^- storage ring cannot be reliably measured, the luminosity must be determined by observing the rate of a process with known cross section. Fortunately, the processes $e^+e^- \rightarrow e^+e^-$, $\mu^+\mu^-$, and $\gamma\gamma$ may be reliably calculated using QED. Furthermore these processes have distinctive topologies making measurement relatively straightforward. Use of each of these reactions to determine the luminosity is discussed below.

The first method considered is measurement of Bhabha scattering at small angles, using the luminosity monitor. The main advantage of this method is the high rate (5-10 Hz). However, these counters were relatively small. So, since the cross section is steeply falling in this angular range ($\sim 1/\theta^4$), there is considerable sensitivity to edge effects in the shower counters, counter placement, and movements of the beam. This method was most useful as a fast online monitor.

Bhabha events observed in the central detector may also be used. This method has the advantage that considerable information is recorded for each event, and furthermore they have such a distinctive topology that a background free sample may be selected with very loose cuts. Higher order corrections to the cross section may be computed fairly reliably, and checked to some extent with the data. The rate is not nearly as high as the small angle case, but in the detector is still 1.5–2 times the rate for hadronic events.

Another possibility is to measure mu pair events in the central detector. This method shares the advantage of good information in the detector with the Bhabhas. However, the detected rate is only about 10% of that for Bhabha events, much less than the hadronic event rate. Furthermore, time of flight cuts must be made to reject cosmic rays, introducing systematic errors due to cracks between TOF counters and non-Gaussian tails of the time distribution.

Whereas gamma-gamma events do not satisfy the charged particle trigger (unless a photon converts) they may only be used for the PEP data. They also feature a distinctive topology and reasonable rate ($\sim$0.4 times the hadronic rate). And since the higher order radiative corrections are somewhat different (there are no vacuum polarization or weak corrections) this process provides a useful check of the others.

Based on the above considerations, the measurement of Bhabha events in the central detector was chosen as the primary luminosity measurement, with the other methods contributing to an estimate of the systematic error.

Bhabha events were required to contain two tracks satisfying the following:

1) $|\cos\theta| \leq 0.65$

2) Momentum $P \geq E_{beam}/2$.

3) Collinear to within 10°.

4) At least 40 mrad from a crack in the LA system.

5) $\sum ELA / \sum |P| \geq 0.25$, where ELA is the energy deposited in the liquid argon system.

Cuts 1) and 4) insured the events were within the detection volume of the liquid argon system. Cuts 2) and 3) allowed for radiative events. They were chosen to be much greater

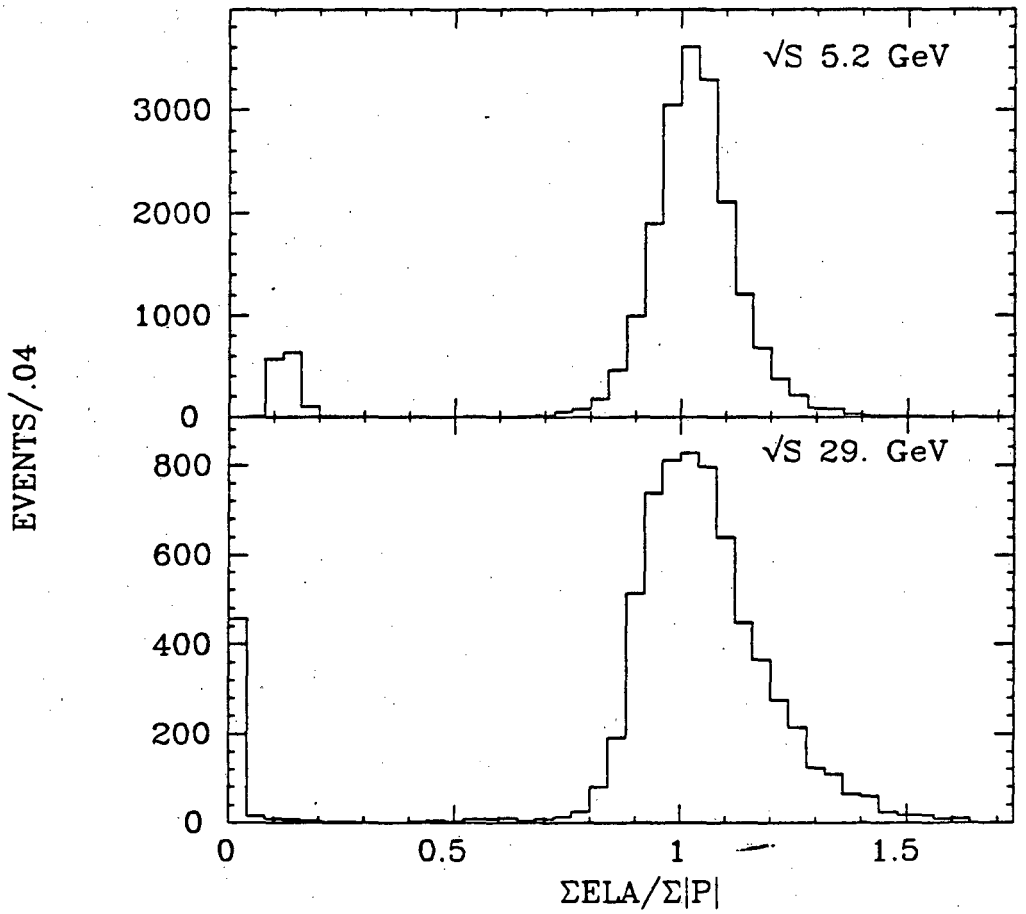

Fig. 35 ΣELA/Σ|P| for events satisfying cuts 1-4.

than the corresponding experimental resolution, while keeping the magnitude of the higher order corrections relatively small. Cut 5) separated Bhabha events from mu pair and cosmic ray events (Figure 35). Events with more than two prongs were included to allow for conversion of radiated photons in the material preceding the drift chambers. At $\sqrt{s} = 5.2$ and 6.5 GeV, 2.5% of the events contained additional tracks; this fraction was 7.5% at 29 GeV. In approximately 10% of these events at 29 GeV, the tracks were so closely spaced as to cause confusion for the pattern recognition program. This therefore contributed 0.7% to the overall normalization uncertainty due to the event selection procedure at that energy. Loss due to tracking inefficiency was searched for by scanning events with one found track with ELA > EBEAM/2. An inefficiency of about 0.5% was found for the SPEAR data. However the lost events were recovered by retracking with the PEP pattern recognition program, which was found to be fully efficient for these events. Whereas the detector trigger at 6.5 GeV required both tracks to have an associated TOF hit, there was an estimated additional 1.9% loss due to cracks between the counters. This inefficiency was estimated from the 5.2 GeV data, where only one track was required to have a TOF hit. Based on a visual scan of 1700 events at the SPEAR energies, misidentified events, namely mu pairs with a collinear photon, cosmic rays, poorly reconstructed events, or multiprongs more likely to be tau or hadron events, were below the level of 0.5%. For the 29 GeV data, possible event misidentification was dominated by the above mentioned confusion in multiprong events.

The expected observed cross section was computed through order α^3 using a Monte Carlo event generator provided by Berends and Kleiss [52]. This program included the muon, tau, and hadron contributions to the vacuum polarization. Particles were generated in accordance with expected kinematical distributions, then projected into the detector generating hits in the appropriate elements and taking into account radiation and photon conversion in the material preceding the drift chambers. The generated Monte Carlo raw data was then passed through the usual event reconstruction programs. Third order QED corrections reduced the observed cross

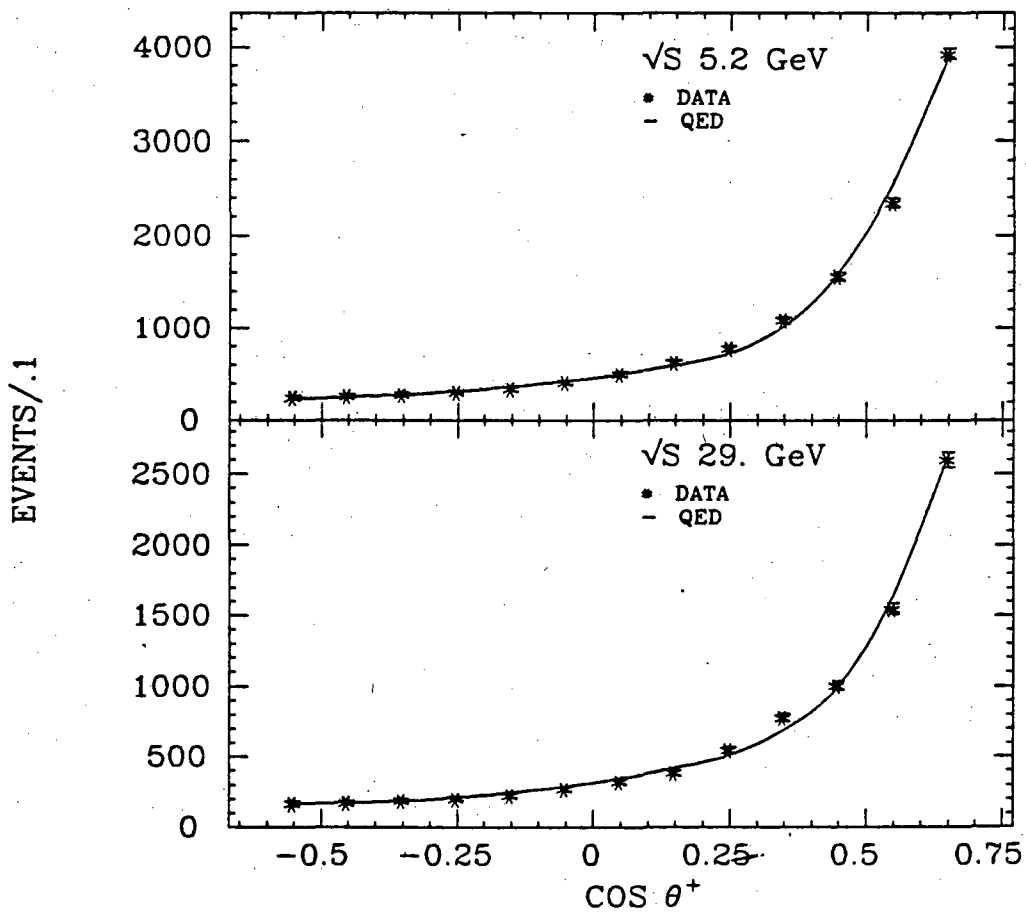

Fig. 36 Angular distribution of the positive track for Bhabha events.

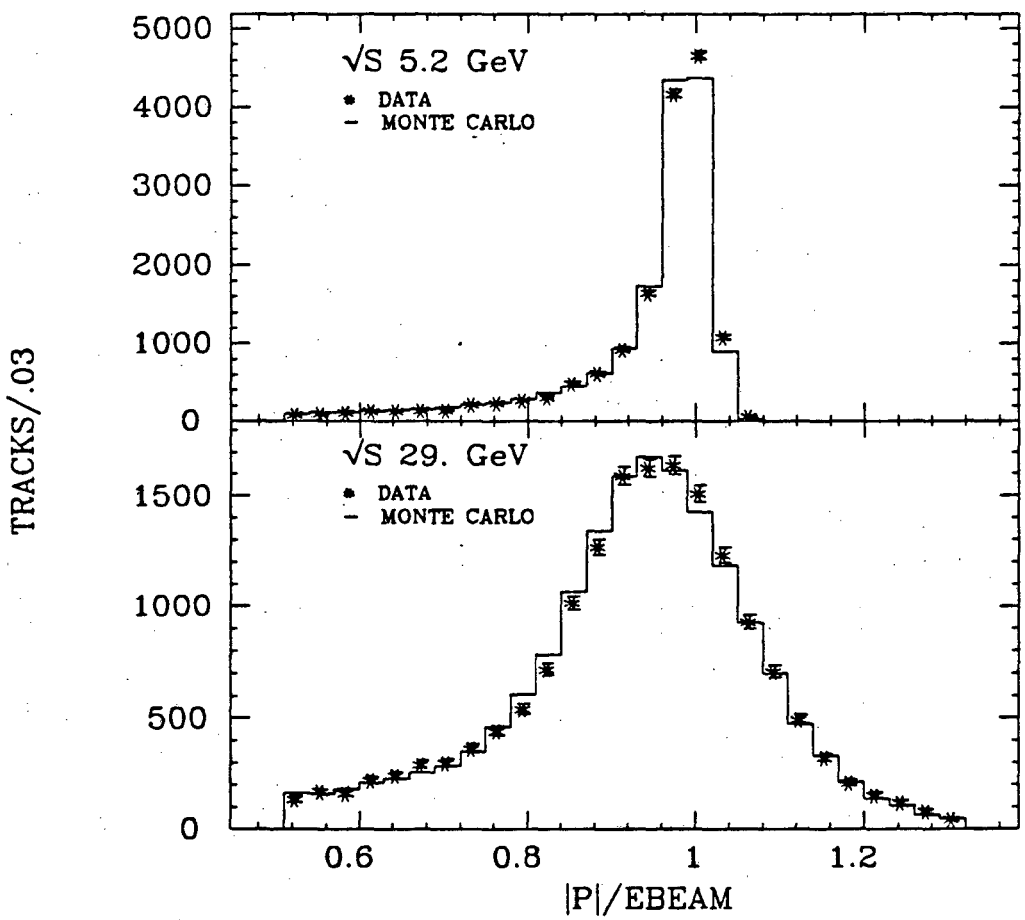

Fig. 37 Observed track momentum distribution for Bhabha events compared with the Monte Carlo prediction.

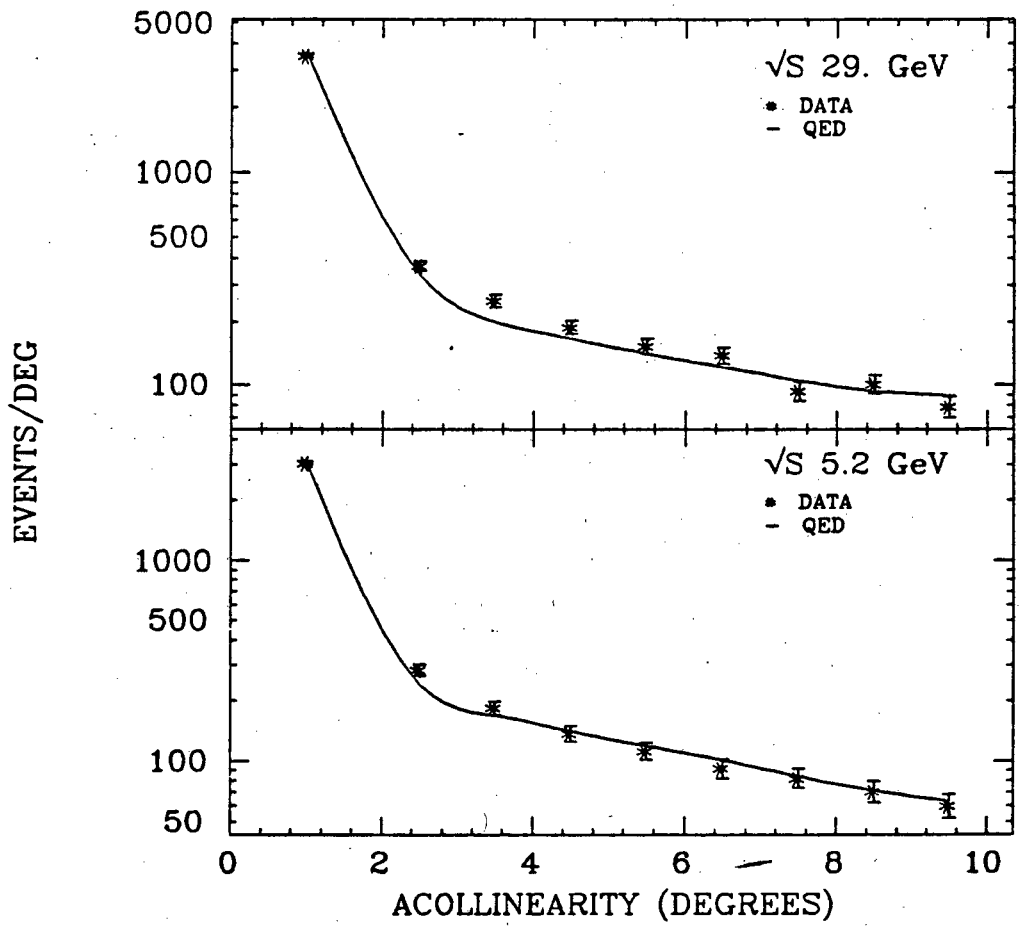

Fig. 38 Observed acolliearity distribution for Bhabha events compared with the Monte Carlo prediction.

section by 7%, external radiation reduced it by another 10%. Comparisons of the data to the predictions of this Monte Carlo are shown in Figures 36, 37, and 38. The best test of the higher order corrections is the acollinearity distribution. This is because the experimental resolution is good ($\sim 0.5°$), and not greatly affected by scattering in the beam pipe. From the variation in the resulting luminosity with the collinearity cut, as well as other theoretical considerations, the estimated uncertainty due to the calculation is estimated to be $\pm 3\%$.

External radiation before the drift chambers also contributed to the uncertainty in the luminosity. This was due to uncertainties in the amount of the material and in the energy loss relation used to estimate the correction, and was estimated to be $\pm 1\%$.

The total estimated uncertainty in this measurement was estimated to be $\pm 3\%$. Uncertainty in the hadronic vacuum polarization, which requires as input the total hadronic cross section, was not included. Since the Q^2 for Bhabha events in the detector is fairly large, it has a similar effect on the radiative corrections for hadronic events, thus any error cancels when the ratio is taken to obtain R.

Comparisons of the luminosity obtained from the monitor to that obtained from Bhabha events are and summarized in Table 4. The 15% difference in the 5.2 data is believed to have resulted from damage to the monitor near the beginning of this running. The systematic error on the monitor measurement was estimated to be $\pm 6\%$ for the SPEAR data. For the PEP data, since there were drift chambers allowing reconstruction of tracks, shower counter edge effects could be much better estimated, reducing the error to $\pm 3\%$.

Muon pair events were selected using the above cuts, except cut 5) was reversed. In addition, to reject cosmic rays the measured flight time was required to be within 3 ns of the expected time based on the path length measured by the drift chamber. The correction for cracks between TOF counters was taken to be that measured from Bhabha events. The results of this analysis are

Process	Events	$\mathcal{L}/\mathcal{L}_{MON}$
	$\sqrt{s}$ 5.2 GeV	
e^+e^-	78230	1.15
$\mu^+\mu^-$	5570	1.14 ± 0.013
	$\sqrt{s}$ 6.5 GeV	
e^+e^-	19375	1.00 ± 0.005
$\mu^+\mu^-$	1420	0.97 ± 0.025
	$\sqrt{s}$ 29.0 GeV	
e^+e^-	8400	1.00 ± 0.01
$\mu^+\mu^-$	635	1.01 ± 0.04
$\gamma\gamma$	1890	0.96 ± 0.02

Table 4.

Comparison of the luminosity obtained from the small angle monitor to that obtained from wide angle Bhabhas, mu pairs, and gamma-gamma events. The errors shown are statistical only.

given in Table 4, and agree well with the luminosity computed from wide angle Bhabha events.

For the PEP data, $\gamma\gamma$ final states were also measured and compared to QED predictions [53]. Table 4 gives the result of this analysis. The 4% systematic error was due mainly to uncertainties from photons which converted, and in the efficiency of the total energy trigger (since it was disabled during bursts of line-synchronous electronic noise.)

The overall uncertainty in the integrated luminosity measurement was estimated to be $\pm 3\%$. The good agreement among all these measurements gives some confidence in this assigned error.

Chapter 7

Results and Conclusions

§7.1 Total Cross Section Results

The ratio R is given by

$$\mathrm{R} = \frac{N - NB}{\epsilon \cdot \mathcal{L} \cdot \sigma_{\mu\mu}} \tag{7.1}$$

where N is the number of observed events, NB is the number of background events, ϵ is the detection efficiency including radiative corrections and $\mathcal{L}$ is the integrated luminosity. Results for R at the three energies are given in Table 5. The first error is statistical, the second systematic. Adding in quadrature the systematic errors from the efficiency calculation, luminosity, radiative corrections and background subtractions gives a total error of about 6% at each of the three energies, these are summarized in Table 6. Relative errors between the 6.5 and 5.2 GeV measurements are estimated to be 2% due to the large background subtraction and more stringent trigger requirements at 6.5 GeV. Relative errors between the SPEAR and PEP measurements are estimated to be $\pm 5\%$. The analyses are sufficiently different that the only common uncertainty is in the calculation of the Bhabha cross section used for normalization. These errors represent some improvement over previous measurements, which generally quoted total systematic errors

$\sqrt{s}$ (GeV)	Luminosity(pb^{-1})	Events	R
5.2	4.16	44180	$3.90 \pm .02 \pm .25$
6.5	1.63	11895	$3.95 \pm .05 \pm .25$
29.0	13.6	4750	$3.90 \pm .05 \pm .25$

Table 5. Results for the ratio $R = \frac{\sigma_{tot}}{\sigma_{\mu\mu}}$.

Reason	5.2 GeV	6.5 GeV	29.0 GeV
Tau subtraction	1.3%	1.2%	0.5%
Beam gas subtraction	0.6%	1.9%	–
Two photon subtraction	0.8%	0.8%	0.8%
Radius cut	1.0%	1.0%	–
Model Dependence	4.%	4.%	4.%
Luminosity	3.%	3.%	3.%
Radiative Corrections	2.5%	2.5%	3.%
Total	6.%	6.%	6.%

Table 6. Contributions to the systematic error in R.

of 10%. The major improvements are in the luminosity measurement and determination of the detection efficiency.

It is noted that there is no significant energy dependence in R over this energy range. The ratio of R at 6.5 to that at 5.2 GeV is

$$\frac{R_{6.5}}{R_{5.2}} = 1.01 \pm 0.02. \tag{7.2}$$

The Mark I data seemed to show a rise in R over this range, however the systematic errors were large, and those measurements extended to higher energy (7.4 GeV). The 90% confidence limit on an increase in R at 29 GeV over the SPEAR energies is 0.4. Thus production of a charge $\frac{2}{3}$ quark, for which an increase in R of $1\frac{1}{3}$ is expected, is excluded by this measurement. Study of the event topology also showed no evidence for production of such a quark, and a search at PETRA for narrow resonances corresponding to bound states of such a quark gave negative results [54] for $\sqrt{s} \leq 36$ GeV. This measurement is not inconsistent with b quark production, which would contribute 0.33 to R in the absence of QCD corrections. The expected difference over this energy range is reduced to 0.15–0.2 by the Q^2 depencence of α_s.

The R values measured at 5.2 and 6.5 GeV lie about two standard deviations above the naive quark model prediction; at 29 GeV this difference is about one standard deviation. Thus the data are consistent either with the parton model, or with the slight deviations expected from QCD and weak interaction effects. The errors are too large, however, to make a meaningful determination of α_s or the weak coupling parameters. The relative errors between the high and low energy data are too large to set limits on $\sin^2\theta_w$, as has been done by several PETRA experiments [55].

The 29 GeV measurement is consistent with other measurements in this energy region. These are summarized in Table 7 [56].

$\sqrt{s}$ (GeV)	Experiment	R
34.	TASSO	4.13 ± 0.2
35.	TASSO	4.22 ± 0.2
33.-36.	JADE	$3.95 \pm 0.08 \pm 0.4$
30.-32.	PLUTO	$3.8 \pm 0.2 \pm 0.4$
33.-36.	CELLO	$3.89 \pm 0.13 \pm 0.5$
33.-36.	Mark J	$3.76 \pm 0.08 \pm 0.4$
29.	MAC	$4.1 \pm 0.05 \pm 0.3$

Table 7. R measurements from other experiments

Whereas R is such a potentially good quantitative test of QCD and of weak interaction theories, it is worthwhile to consider whether the systematic errors in the measurement can be reduced to the level where a meaningful test of these theories can be made. This of course assumes that enough data can be accumulated so that the statistical error is sufficiently small.

The largest contribution to the uncertainty is from the detection efficiency and background calculations. Since one-photon annihilation events have the property that the produced energy is the center of mass energy, in principle the optimum strategy would be to measure total energy over as large a solid angle as practical. Whereas solenoidal spectrometers such as the Mark II have limited momentum resolution at small angles, a calorimeter based detector such as MAC [57] may give better results. However, backgrounds from two photon and beam gas interactions increase dramatically at small angles, so that some overlap in the energy distributions of the two processes is inevitable given the finite resolution of any detector. Since the background events have a large net longitudinal momentum compared to 1-photon annihilation events, this may be used to separate these classes of events. Since the resolution of calorimeters is inversely proportional to $\sqrt{E}$, they would not offer much advantage at lower energies as far as this measurement is concerned. Thus at low energies, there will inevitably be significant beam-gas background, which however could be estimated from extensive separated beam running. Tau events are also a significant background in this energy region; a precise subtraction would require more information about the decay branching ratios, particularly for the multi-pion modes.

The luminosity measurement is already nearly limited by calculation of higher order corrections to the Bhabha cross section. In an experiment with better momentum resolution and a thinner beam pipe, such that corrections due to final state radiation and external photon conversion are small, the uncertainty would be almost entirely in the calculation. Note however that calorimeter based detectors which do not measure well the momentum and acollinearity cannot

determine radiative corrections as well, limiting the precision on the luminosity measurement.

For radiative corrections to hadron production, measurements of hadronic event properties and relative cross sections at intermediate energies preferably with the same detector, would remove most of the experimental uncertainty in these corrections at PEP energies. The situation is much worse for the SPEAR energies, due to the the complicated structure in the 4 GeV region. This is especially difficult since determination of the structure requires assumptions about the cross section in the absence of radiation, which of couse cannot be directly measured. However there are still higher order and final state radiative corrections which are difficult to estimate.

So while some experimental improvements are possible, uncertainties in QED corrections at the level of a few percent could still partially obscure QCD and weak effects. And as discussed in Chapter 1, uncertainties in the weak mixing angle θ_w make QCD tests difficult for $\sqrt{s} > 45$ GeV.

§7.2 Results for $s\frac{d\sigma}{dx}$

The results obtained for $s\frac{d\sigma}{dx}$ are displayed in Figure 39 and summarized in Table 8. Systematic errors are estimated to be $\pm 6\%$ for low x rising to $\pm 10\%$ at high x due to uncertainties in the model at low energies, and in the tracking efficiency and momentum resolution effects at 29 GeV. The low energy data lie somewhat below the Mark I measurements, at the edge of the quoted systematic errors. This difference is believed to have two origins. First, the detection efficiency as a function of x was computed using the "jet" model, which gave a lower efficiency and thus a higher cross section. However in Chapter 5 it was shown that the Feynman Field model gave a better description of the data as far as this measurement is concerned. Also, the decay modes of the tau lepton are better established allowing a proper estimate of this background.

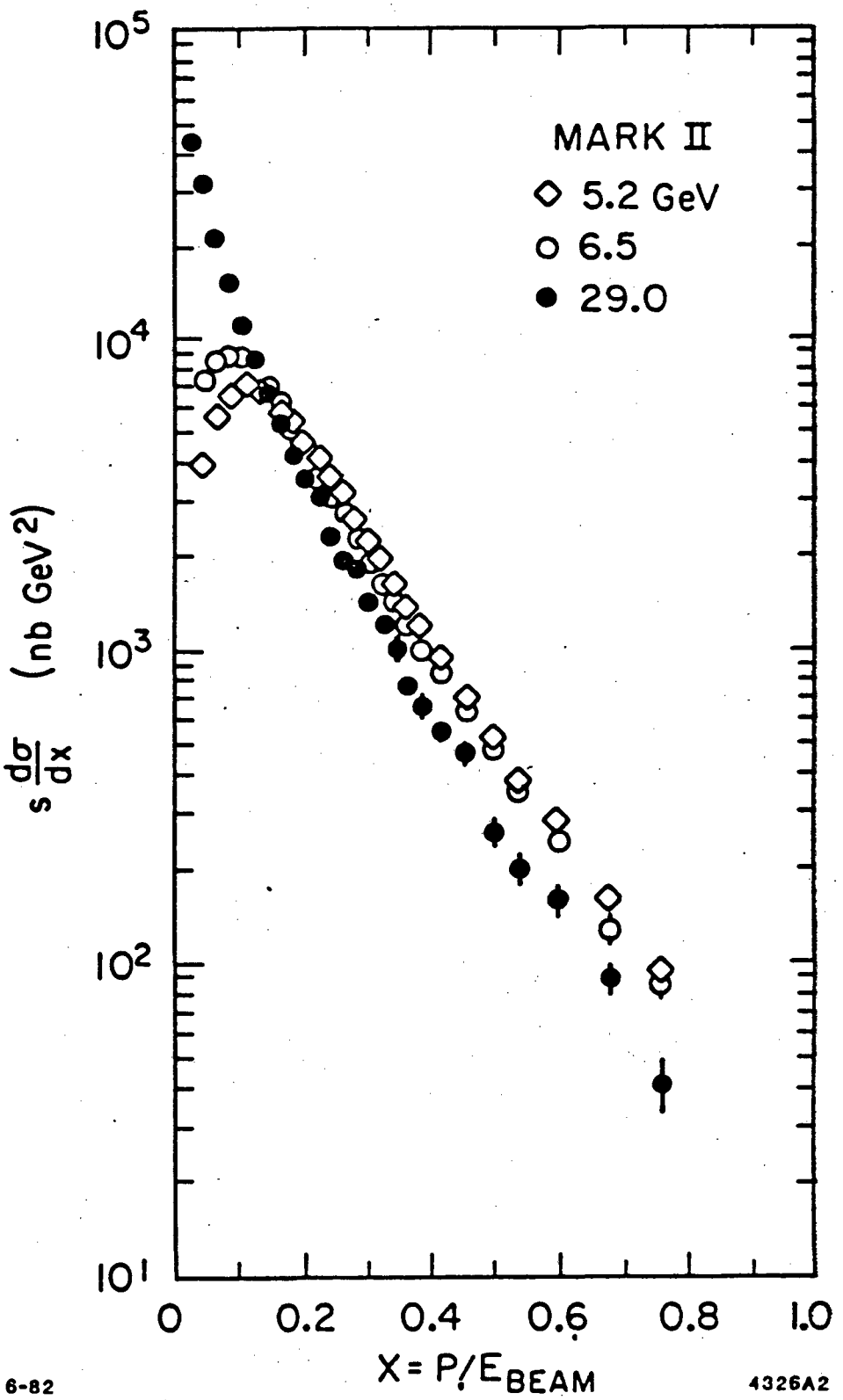

Fig. 39 $sd\sigma/dx$ at 5.2, 6.5, and 29.0 GeV as measured by this experiment.

x	$\sqrt{s}$ 5.2 GeV	$\sqrt{s}$ 6.5 GeV	$\sqrt{s}$ 29.0 GeV
.02-.04	1.94 ± 0.20	3.49 ± 0.16	42.2 ± 0.4
.04-.06	3.93 ± 0.05	7.63 ± 0.12	31.0 ± 0.3
.06-.08	5.75 ± 0.05	8.88 ± 0.13	20.7 ± 0.3
.08-.10	6.54 ± 0.06	9.15 ± 0.13	14.9 ± 0.3
.10-.12	7.02 ± 0.06	8.85 ± 0.13	11.0 ± 0.2
.12-.14	6.87 ± 0.06	8.35 ± 0.13	8.34 ± 0.19
.14-.16	6.63 ± 0.06	7.38 ± 0.12	6.50 ± 0.19
.16-.18	5.93 ± 0.06	6.43 ± 0.12	5.20 ± 0.15
.18-.20	5.29 ± 0.05	5.38 ± 0.11	4.10 ± 0.12
.20-.22	4.62 ± 0.05	4.83 ± 0.10	3.48 ± 0.12
.22-.24	4.20 ± 0.05	3.73 ± 0.10	3.02 ± 0.12
.24-.26	3.62 ± 0.05	3.36 ± 0.09	2.29 ± 0.12
.26-.28	3.20 ± 0.04	2.92 ± 0.09	1.89 ± 0.10
.28-.30	2.66 ± 0.04	2.39 ± 0.08	1.88 ± 0.10
.30-.32	2.23 ± 0.04	2.02 ± 0.07	1.44 ± 0.09
.32-.34	2.03 ± 0.04	1.74 ± 0.07	1.19 ± 0.08
.34-.36	1.66 ± 0.03	1.52 ± 0.06	0.98 ± 0.06
.36-.38	1.40 ± 0.03	1.26 ± 0.06	0.76 ± 0.08
.38-.40	1.22 ± 0.03	1.05 ± 0.06	0.67 ± 0.07
.40-.44	0.96 ± 0.02	0.89 ± 0.04	0.54 ± 0.04
.44-.48	0.71 ± 0.02	0.66 ± 0.03	0.47 ± 0.03
.48-.52	0.54 ± 0.02	0.50 ± 0.03	0.26 ± 0.03
.52-.56	0.38 ± 0.01	0.36 ± 0.03	0.20 ± 0.02
.56-.64	0.29 ± 0.01	0.25 ± 0.02	0.16 ± 0.02
.64-.72	0.16 ± 0.01	0.13 ± 0.01	$.089 \pm 0.01$
.72-.80	$.093 \pm 0.01$	$.085 \pm 0.01$	$.040 \pm 0.01$

Table 8. $s\frac{d\sigma}{dx}$ (μb-GeV^2; statistical errors)

A cross check on the results may be made by comparing the integral of the distributions to the mean multiplicity obtained from the unfold (No unfold is done at 29 GeV as considerable Monte Carlo statistics would be required). In particular, the following relation should hold:

$$\frac{3}{4\pi\alpha^2 R}\int s\frac{d\sigma}{dx}dx = < N_{ch} > . \tag{7.3}$$

Results for this comparison are shown in Table 9, the agreement is good.

The 29 GeV data lie significantly above the low energy data for $x < 0.2$, and significantly below them for $x > 0.2$, the difference being well outside the estimated relative systematic errors. This is seen more clearly in Figure 40 which shows $s\frac{d\sigma}{dx}$ versus s for several regions in x. The difference between the high and low energy data is almost a factor of two for the largest x regions. Figure 41 plots $\frac{1}{\sigma}\frac{d\sigma}{dx}$. This ratio is plotted to remove systematic errors in normalization and to compensate for changes in total hadron production due to the b quark threshold. This experiment is thus seen to be in good agreement with similar measurements made using the TASSO detector [58] when normalization differences are accounted for.

The magnitude of the scaling violation is larger than the QCD predictions discussed in Chapter 1. However those predictions are for the primary produced hadrons, whereas this experiment measures the decay products of short lived vector, charm, and bottom particles. To estimate the effect of gluon emission, Monte Carlo distributions generated for $\sqrt{s} = 29.$ GeV with the program discussed in Chapter 5 for all events and for events with no gluons are compared. For reasonable values of Λ, the difference between the two curves is only $\sim 25\%$ at $x = 0.7$, also not sufficient to account for the entire scale breaking. The effect is even in fact exagerated in this model due to the discontinuity between events with and events without gluons. Other possible contributions are now considered.

For events where c and b quarks are produced, because only the decay products of the leading

$\sqrt{s}$ (GeV)	$\frac{3s}{4\pi\alpha^2 R}\int\frac{d\sigma}{dx}$	$< N_{ch} >$
5.2 GeV	$5.0 \pm .1$	$5.2 \pm .1$
6.5 GeV	$5.7 \pm .1$	$5.8 \pm .1$

Table 9. Integrated x distributions compared to mean multiplicities.

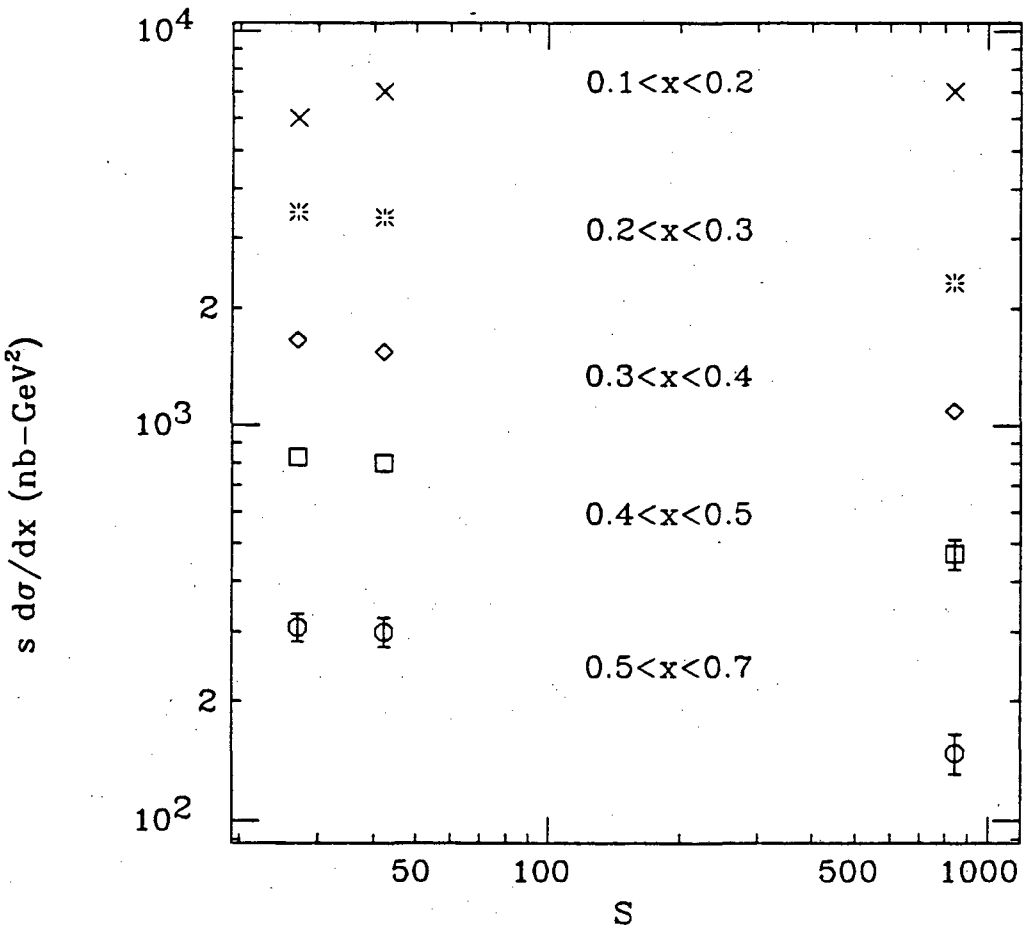

Fig. 40 sdσ/dx versus s as measured by this experiment.

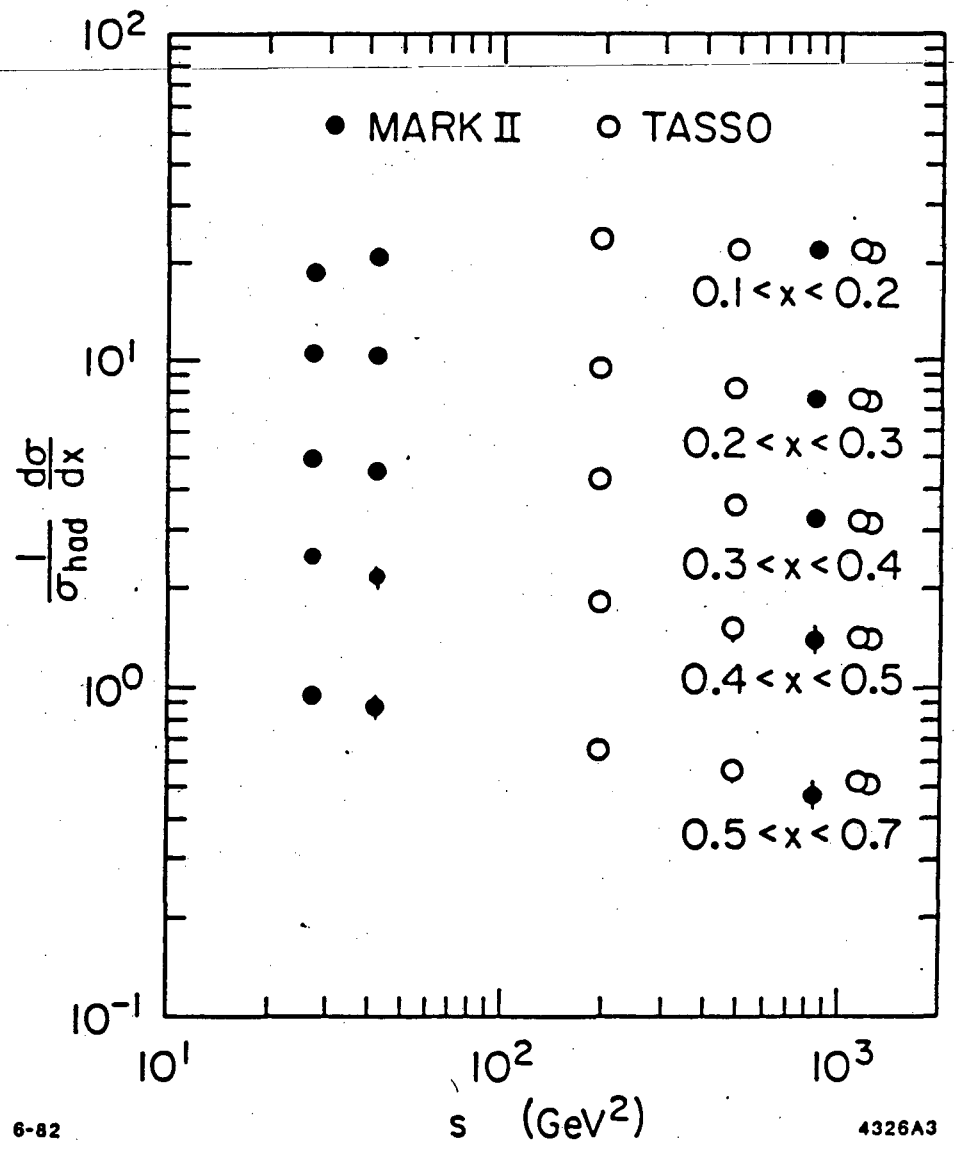

Fig. 41 $1/\sigma\ d\sigma/dx$ versus s as measured by the Mark II and TASSO experiments.

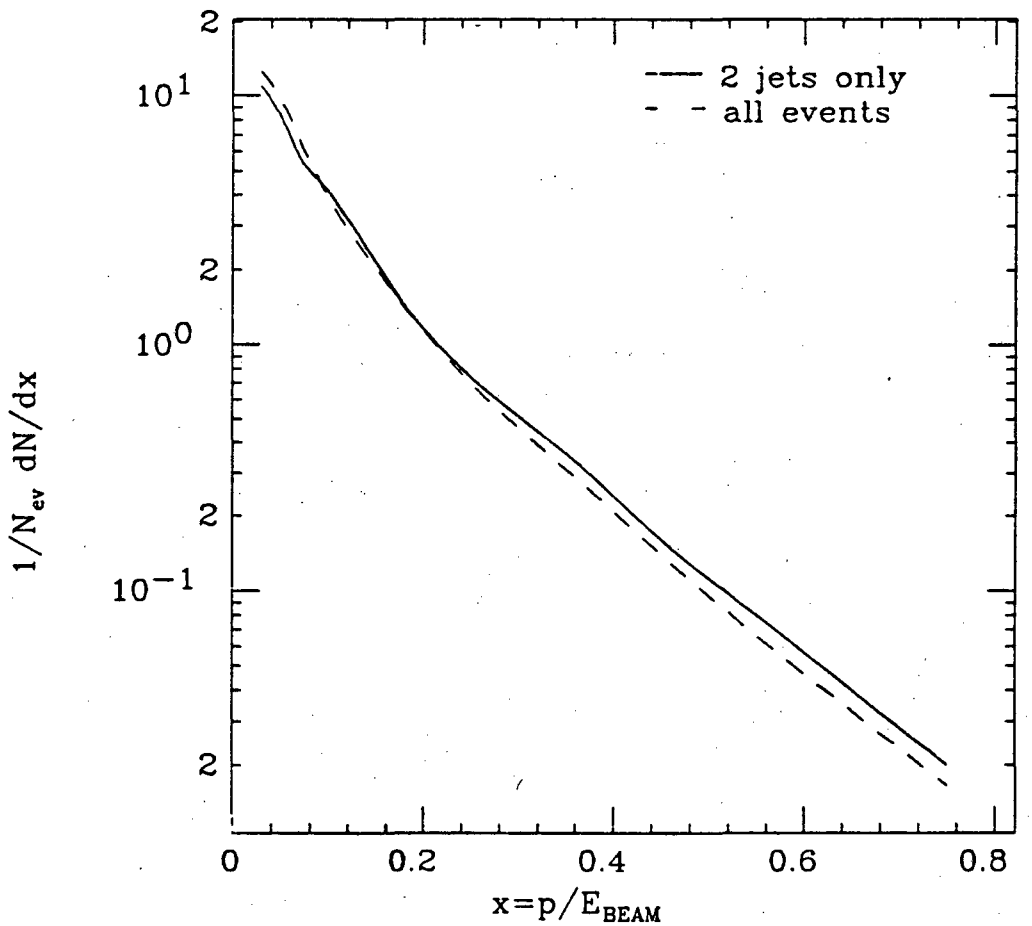

Fig. 42 1/N dN/dx at 29. GeV as predicted by the Ali et al. Monte Carlo for all events and for events with no hard gluon, assuming Λ=0.3 GeV.

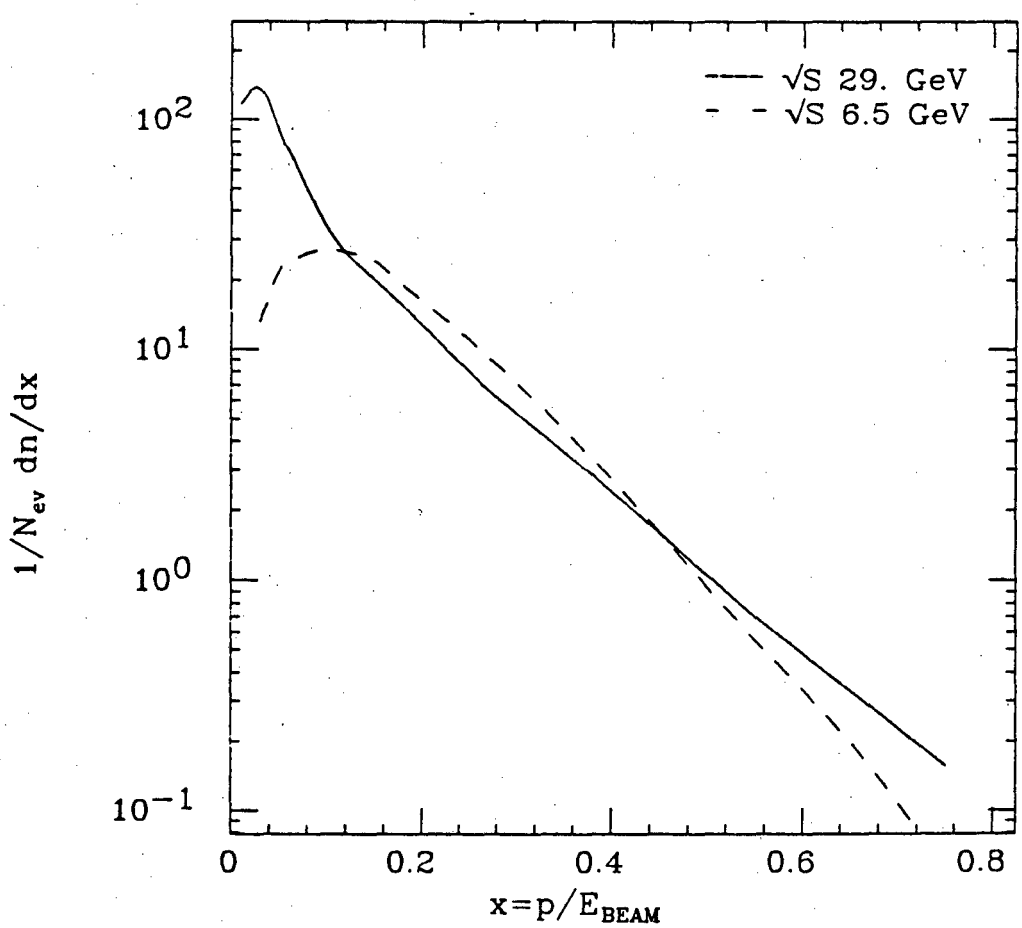

Fig. 43 1/N dN/dx at 6.5 and 29. GeV for events containing a primary charm quark as predicted by the Feynman-Field model, assuming a flat charm splitting function.

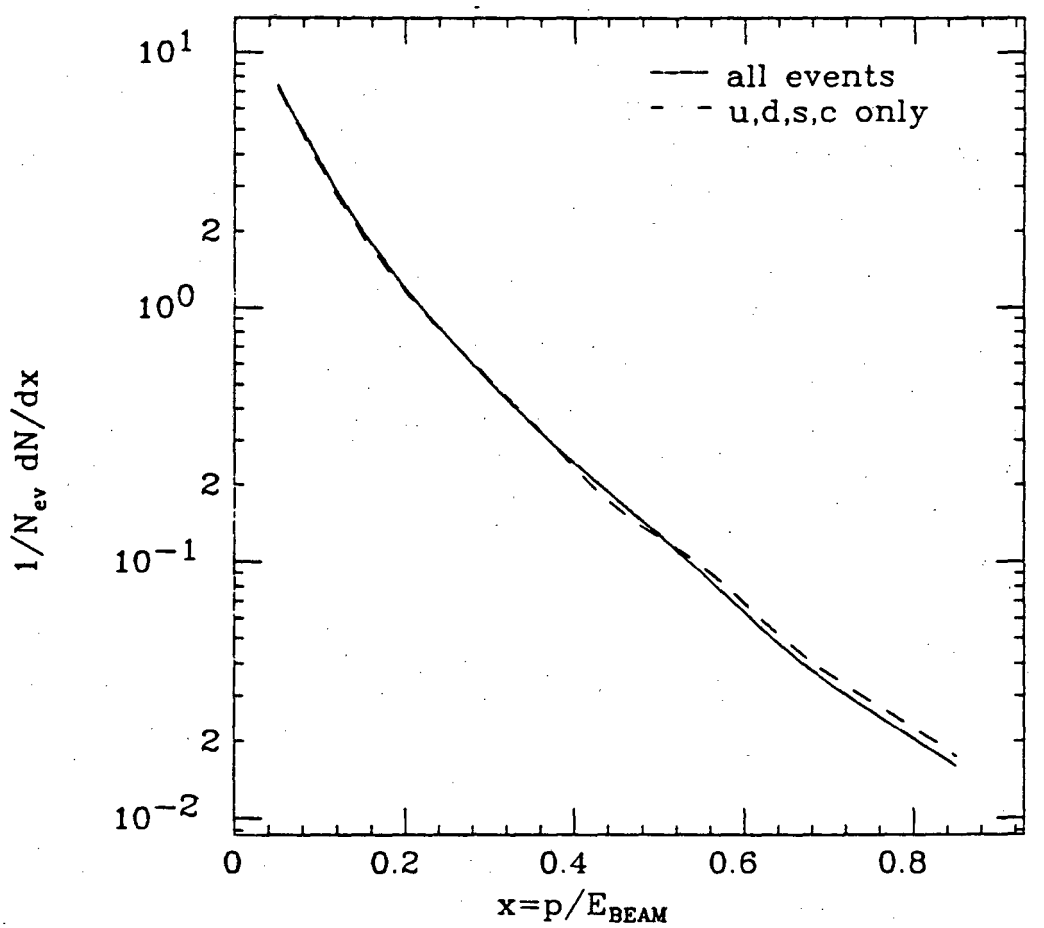

Fig. 44 1/N dN/dx at 29. GeV as predicted by the Ali et al. Monte Carlo for all events compared to events where the primary quark is not a b quark.

c or b particles are detected, the momentum distribution will be softer than that of the primary hadrons. However, as s is increased, the decay products are boosted along the initial quark direction, actually giving a rise in the cross section at large x for these events, in the opposite direction from the observed non-scaling effect. Figure 5 shows $\frac{1}{N}\frac{dN}{dx}$ versus s for events with a primary charm quark, which shows this rise. Thus charm production is unlikely to be the cause of the large observed scale breaking at high x. However since the SPEAR data lie below b quark threshold, b production could contribute to the scale breaking observed over the energy range of this experiment. Figure 6 shows Monte Carlo distributions of $\frac{1}{N}\frac{dN}{dx}$ versus x at $\sqrt{s} = 29.$ GeV for all events, and for events where the primary quark is not a b quark. A flat splitting function for the b quark was assumed. There is about a 5% difference between these two curves at $x = 0.8$, this could be more or less depending on the actual b quark splitting function.

Non-perturbative effects could also contribute to the observed scaling violation, especially since at the SPEAR energies particle masses are not necessarily negligible. The rise in charged multiplicity over this range is much steeper than the logarithmic rise expected from the increase in available longitudinal phase space [6]. As one way of examining this possibility, the s dependence of the Feynman-Field model is examined. With the parameters fixed at the values used to fit the low energy data, this model appears to approximately scale for $x > 0.4$, as shown in Figure 7. However there are significant effects below $x = 0.3$, where at the low energies, particle rest masses are not negligible. Note most of the rise in charged multiplicity with s is for $x < 0.1$. An increase in vector particle production, which is likely as the available phase space increases, would cause scale breaking, since only the resonance decay products are observed. The previous figure also shows $\frac{1}{N}\frac{dN}{dx}$ at $\sqrt{s} = 29.$ GeV assuming a vector fraction of 0.5. As the vector fraction is increased to 0.5, differences of $\sim$25% are seen for $x = 0.7$. Thus it is likely that the large scaling violation observed in this experiment receives contributions from non-perturbative effects as well as gluon emission. Given how well QCD describes the jet properties of the data,

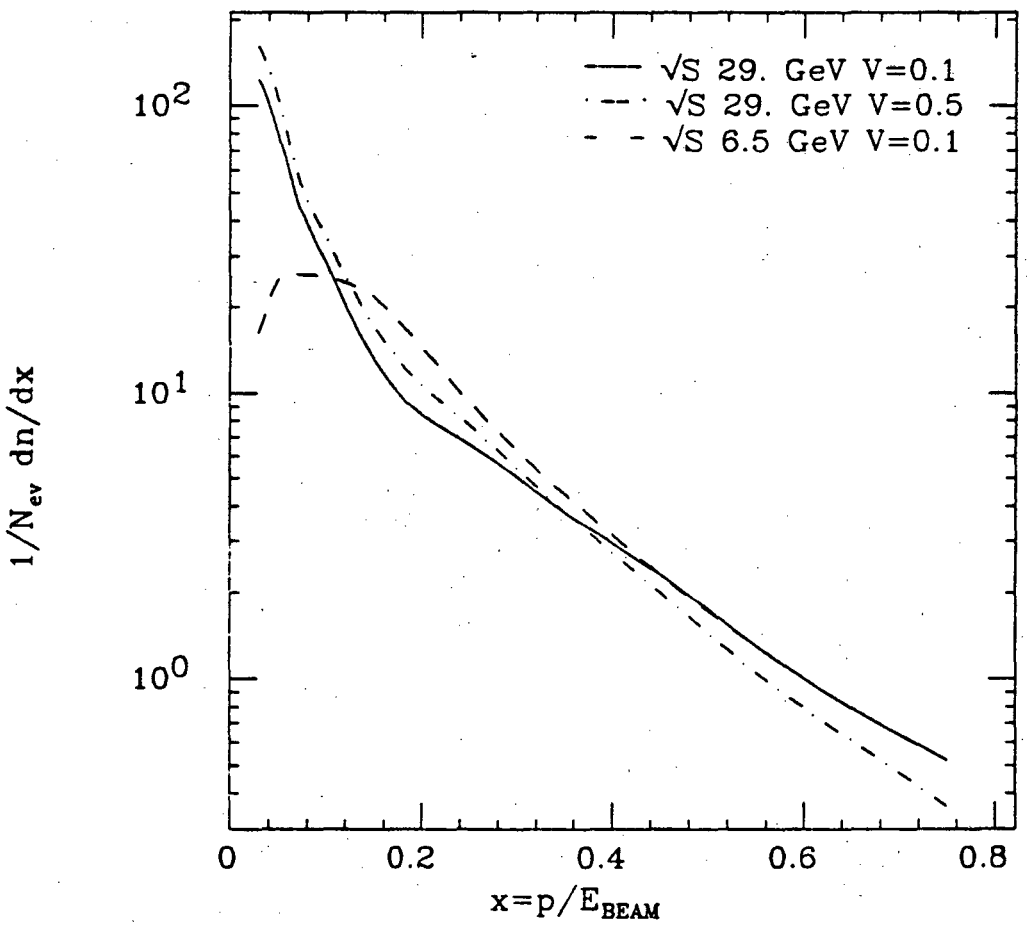

Fig. 45 1/N dN/dx at 6.5 and 29. GeV for events with a primary u,d, or s quark as predicted by the Feynman-Field model with A=0.77 and the vector fractions shown.

it is natural to question the effect of these non-perturbative effects on that analysis. However, it has been shown [7] in the determination of α_s from jet properties that α_s is not very sensitive to fine details of the fragmentation process (or the exact parameters used in the Monte Carlo).

In conclusion, we have determined the ratio R over a wide energy range with better precision than previous measurements. The results obtained are consistent with production of the standard u, d, s, c, and b (above threshold) quarks. Further work will be required, however, to make more detailed quantitative tests of QCD and weak interaction theories. Also, considerable scale breaking, in the direction predicted by QCD, has been observed in the inclusive distributions over this energy range. Again, further measurements will be required to determine the full origin of this behavior, and to quantitatively test QCD.

REFERENCES

1. J. Siegrist *et al.*, SLAC-PUB-2831, Submitted to Physical Review D;
   J. Siegrist, SLAC-225, Ph.D. Thesis (unpublished).

2. G. Zweig, CERN-TH-401,402 (1964), unpublished;
   M. Gell-Mann, Phys. Lett. 8, 214 (1964).

3. S. Glashow *et al.*, Phys. Rev. D2, 1285 (1970).

4. J.E. Augustin *et al.*, Phys. Rev. Lett. 33, 1406 (1974);
   J.J. Aubert *et al.*, Phys. Rev. Lett. 33, 1404 (1974);
   G.S. Abrams *et al.*, Phys. Rev. Lett. 33, 1453 (1974).

5. S.W. Herb *et al.*, Phys. Rev. Lett. 39, 252 (1977);
   W.R. Innes *et al.*, Phys. Rev. Lett. 39, 1240 (1977).

6. G. Hanson *et al.*, Phys. Rev. Lett. 35, 1609 (1975);
   G. Hanson *et al.*, SLAC-PUB-2855, Submitted to Physical Review D.

7. S.D. Drell and T.-M. Yan, Phys. Rev. 187, 2159 (1969);
   S.D. Drell and T.-M. Yan, Phys. Rev. D1, 1617 (1970);
   R.P. Feynman, Photon-Hadron Interactions, W.A. Benjamin (1972).

8. J.D. Bjorken, Phys. Rev. 179, 1547 (1969).

9. J. Siegrist *et al.*, SLAC-PUB-2831, Submitted to Physical Review D;
   J. Siegrist, SLAC-225, Ph.D. Thesis (unpublished).

10. C. Bouchiat *et al.*, Phys. Lett. 38B, 519 (1972);
    D.J. Gross and R. Jackiw, Phys. Rev. D6, 477 (1972);

G. 't Hooft, Nucl. Phys. B35, 167 (1971).

11. S. Weinberg, Phys. Rev. D13, 974 (1976);
L. Susskind, Phys. Rev. Lett. 19, 2619 (1979);
S. Dimopoulos, Nucl. Phys. B168, 69 (1979).

12. S.L. Adler, Lectures on Elementary Particles and Quantum Field Theory, MIT Press (1971).

13. D.J. Gross *et al.*, Phys. Rev. Lett. 30, 1343 (1973);
H.D. Politzer, Phys. Rev. Lett. 30, 1346 (1973).

14. R. Brandelik *et al.*, Phys. Lett. 86B, 243 (1979);
Ch. Berger *et al.*, Phys. Lett. 86B, 418 (1979);
D.P. Barber *et al.*, Phys. Rev. Lett. 43, 830 (1979);
W. Bartel *et al.*, DESY Report 79/80 (1980).

15. T. Appelquist and H.D. Politzer, Phys. Rev. D12, 1404 (1975).

16. W. Celmaster and R.J. Gonsalves, Phys. Rev. Lett. 44, 560 (1979);
V.G. Chetyrkin, A.L. Kataev, and F.V. Tkachev, Phys. Lett. 85B, 277 (1979);
M. Dine and J. Sapirstein, Phys. Rev. Lett. 43, 668 (1979).

17. W. Celmaster and D. Sivers, Phys. Rev. D23, 227 (1981);
P.M. Stevenson, Phys. Lett. 100B, 61 (1981).

18. T.D. Gottschalk, Phys. Lett. 109B, 331 (1982);
R.K. Ellis, D.A. Ross, A.E. Tarrano, CALTECH Report 68-785 (1980);
K. Fabricius *et al.*, Z. Phys. C11, 315 (1982);
Z. Kunzt, Phys. Lett. 99B, 429 (1981);

A. Ali, DESY Report 81/59 (1981).

19. J. Jersák, E. Laermann and P.M. Zerwas, Phys. Lett. 98B, 363 (1981);
J. Ellis and M.K. Galliard, CERN 76-18, (1976).

20. C.Y. Prescott *et al.*, Phys. Lett. 77B, 347 (1978);
C.Y. Prescott *et al.*, Phys. Lett. 84B, 524 (1979);
Winter, Proc. of the 1979 Symposium on Lepton and Photon Interactions at High Energies, Fermilab 371 (1979).

21. G. Altarelli *et al.*, Nucl. Phys. B160, 301 (1979);
R. Baier *et al.*, Z. Phys. C2, 339 (1979);
W.R. Frazer and J.F. Gunion, Phys. Rev. D20, 147 (1978);
J.F. Owens, Phys. Lett. 76B, 85 (1978);
T. Uematsu, Phys. Lett. 79B, 97 (1978).

22. R. Baier *et al.*, Z. Phys. C2, 265 (1979).

23. A. Bäcker, DESY-F33-77/03, Ph.D. Thesis (unpublished);
R. Brandelik *et al.*, Phys. Lett. 67B, 358 (1978).

24. R. Brandelik *et al.*, Phys. Lett. 83B, 261 (1980);
R. Brandelik *et al.*, Phys. Lett. 89B, 418 (1980).

25. R.H. Schindler, SLAC-219, Ph.D. Thesis (unpublished).

26. J.A. Kadyk, PEP-0362, (1980).

27. W. Davies-White *et al.*, Nucl. Instrum. Methods 160, 227 (1979).

28. J.E. Grund *et al.*, IEEE Trans. Nuclear Science NS-27, 599, 1980.

29. G.S. Abrams *et al.*, IEEE Trans. Nuclear Science, NS-25, 309, (1978);
G.S. Abrams *et al.*, IEEE Trans. Nuclear Science, NS-27, 59, (1980).

30. H. Brafman *et al.*, IEEE Trans. Nuclear Science, NS-25, 692, (1978);
T. Himel, SLAC-223, Ph.D. Thesis (unpublished).

31. R.H. Schindler, SLAC-219, Ph.D. Thesis (unpublished) and references therein.

32. C.A. Blocker, LBL-10801, Ph.D. Thesis (unpublished).

33. The acoplanarity angle is defined to be 180° - the angle between the tracks in the plane perpendicular to the beam axis.

34. A track was considered an electron if its associated energy deposition in the Liquid Argon system exceeded half its momentum. Tracks with $x > 0.7$ not within the LA detection volume were considered electrons.

35. C.A. Blocker *et al.*, SLAC-PUB-2929, To be Submitted to Physical Review D.

36. G. Hanson *et al.*, Phys. Rev. Lett. 35, 1609 (1975).

37. This model is described in detail in S. Cooper, LBL-11322, Ph.D. Thesis.

38. S. Cooper, LBL-11322, Ph.D. Thesis (unpublished).

39. R.D. Field and R.P. Feynman, Nucl. Phys. B136, 1 (1978).

40. M. Suzuki, Phys. Lett. 71B, 139 (1977);
J.D. Bjorken, Phys. Rev. D17, 171 (1978).

41. J.M. Yelton *et al.*, SLAC-PUB-2926, Submitted to Physical Review Letters.

42. A. Ali *et al.*, Phys. Lett. 93B, 155 (1980).

43. The thrust is defined to be $T = \sum_i P_{L_i} / \sum_i |P_i|$ where P_{L_i} is the momentum component along an axis (the "thrust" axis) so that T is maximized.
E. Farhi, Phys. Rev. Lett. 39, 1587 (1977).

44. Whereas at least two particles are generated for each gluon, no matter how soft, the genreated momentum and multiplicity will in fact be slightly affected by this cutoff.

45. Altarelli and Parisi, Phys. Lett. 60B, 100 (1977).
The computed efficiencies are not very sensitive to the choice of the splitting function.

46. This analysis has not attempted to determine α_s.

47. R.H. Schindler, SLAC-PUB-219, Ph.D. Thesis (unpublished).

48. B. Andersson *et al.*, Nucl. Phys. B197, 45 (1982);
B. Andersson *et al.*, Z. Phys. C6, 235 (1980).

49. G. Bonneau and F. Martin, Nucl. Phys. B27, 381 (1971);
F.A. Berends and R. Kleiss, Nucl. Phys. B178, 141 (1981).

50. F.A. Berends and R. Kleiss, *ibid.*

51. E. Laermann *et al.*, SLAC-PUB-2901, Submitted to Nuclear Physics B.

52. F.A. Berends and R. Kleiss, Nucl. Phys. B177, 237 (1981).

53. C.A. Blocker *et al.*, SLAC-PUB-2929, to be Submitted to Physical Review D.

54. R. Brandelik *et al.*, Phys. Lett. 88B, 199 (1979);
W. Bartel *et al.*, Phys. Lett. 89B, 136 (1979);
H.J. Behrend *et al.*, DESY Report 81/29, Submitted to Physics Letters;
D.P. Barber *et al.*, Phys. Rev. Lett. 44, 1722 (1980).

55. W. Bartel *et al.*, Phys. Lett. 101B, 361 (1981);

D.P. Barber *et al.*, Phys. Rev. Lett. 46, 1663 (1981).

56. R. Brandelik *et al.*, DESY Report 82/10, Submitted to Physics Letters;

W.T. Ford *et al.*, SLAC-PUB-2921;

J-F. Grivaz, in Proceedings of the XVI Recontre de Moriond (1981).

57. PEP proposal PEP-6.

58. R. Brandelik *et al.*, DESY Report 82/13, Submitted to Physics Letters.

59. R.P. Feynman, Phys. Rev. Lett. 23, 1415 (1969).

60. J. Freeman, Wisconsin Ph.D. Thesis (1981).

This report was done with support from the Department of Energy. Any conclusions or opinions expressed in this report represent solely those of the author(s) and not necessarily those of The Regents of the University of California, the Lawrence Berkeley Laboratory or the Department of Energy.

Reference to a company or product name does not imply approval or recommendation of the product by the University of California or the U.S. Department of Energy to the exclusion of others that may be suitable.

TECHNICAL INFORMATION DEPARTMENT
LAWRENCE BERKELEY LABORATORY
UNIVERSITY OF CALIFORNIA
BERKELEY, CALIFORNIA 94720